Granular Dynamics in Vibrated Beds

Samenstelling promotiecommissie:

Prof. dr. C.A. van Blitterswijk, voorzitter	Universiteit Twente
Prof. dr. ir. J.A.M. Kuipers, promotor	Universiteit Twente
Dr. ir. M.A. van der Hoef, assistent-promotor	Universiteit Twente
Prof. dr. E.G. Flekkøy	University of Oslo, Noorwegen
Jun.-Prof. Dr.-Ing. S. Heinrich	Universität Magdeburg, Duitsland
Prof. dr. ir. R.F. Mudde	Technische Universiteit Delft
Prof. dr. W.J. Briels	Universiteit Twente
Prof. dr. D. Lohse	Universiteit Twente
Dr. ir. N.P Kruyt	Universiteit Twente
Dr. D. van der Meer	Universiteit Twente

Publisher:
Printpartners Ipskamp B.V., P.O. box 333, 7500 AH, Enschede, the Netherlands

Granular Dynamics in Vibrated Beds / by Christiaan Zeilstra. - Enschede: University of Twente, 2007. - Proefschrift.

Copyright ©2007 by Christiaan Zeilstra

No part of this book may be reproduced by print, photocopy, microfilm or any other means without written permission from the author.

ISBN 978-90-365-2486-5

Granular Dynamics in Vibrated Beds

PROEFSCHRIFT

ter verkrijging
van de graad van doctor aan de Universiteit Twente,
op gezag van de Rector Magnificus,
prof.dr. W.H.M. Zijm,
volgens besluit van het College voor Promoties
in het openbaar te verdedigen
op vrijdag 11 mei 2007 om 15.00 uur

door

Christiaan Zeilstra

geboren op 19 oktober 1977
te Sneek

Dit proefschrift is goedgekeurd door de promotor

Prof. dr. ir. J.A.M. Kuipers

en de assistent-promotor

Dr. ir. M.A van der Hoef

The work described in this thesis was part of the research program of the Foundation for Fundamental Research on Matter (FOM), and was made possible by financial support from the Dutch Organization for the Advancement of Research (NWO).

Aan mijn ouders

Contents

Summary

Granular matter subject to vibration is found to display a wide range of interesting phenomena, and for this reason it has been a popular research topic in academia for decades. Depending on the particle properties and vibration parameters, the flow behavior of the material can be very different, behaving as a solid, liquid or even a gas, leading to a wealth of phenomena such as heaping, convection, pattern formation, etc. The processing of particle mixtures may even lead to segregation, which is often undesirable. To make matters more complex, additional forces such as those from the interstitial gas come into play when the particles are small, leading to new and sometimes very surprising phenomena. In the study of such complex systems, computer simulations can play an important role since they can provide data that is not accessible in experiments, and since interactions can be switched on and off at will it is relatively easy to study the effects of parameters separately. Moreover, preliminary simulations can provide a window of desired operating conditions that can be explored more fully in focused experiments. In this thesis, the flow and segregation behavior of granular matter subject to vertical vibrations is studied by numerical modeling and experimentation. As a second, separate subject, the dynamics of a large intruder particle when forced through a bed of much smaller particles is studied. The topics in order of appearance: (i) wall-induced granular convection, (ii) air-induced segregation of fine bronze and glass particles, (iii) solids circulation in gas-vibro fluidized beds, (iv) dynamics of a large sphere upon impact on a static granular bed, and (v) dynamics of a large sphere in a fluidized granular bed.

There are a number of simulation methods available for gas-solid two-phase flows, where the models differ in the amount of detail taken into account, and hence also the scale on which they can operate. The discrete particle model (DPM) was found to be the most suitable for the description of the systems that were studied, since it combines the necessary level of detail for the solids phase with the capability of modeling a sufficiently large system size.

In DPM, the solids phase is considered to be made up out of individual spherical particles, where the trajectories are calculated by solving Newton's equation of motion. A soft-sphere type collision model is used to describe the interactions in between particles when in contact, and the gas flow is described by the volume-averaged Navier-Stokes equations. The interaction between the gas and particles is handled via empirical drag relations and two-way coupling ensures that amounts

of momentum exchanged between the phases is preserved. This type of modeling is often used for the description of gas-fluidized beds and was also found to be the most suitable one for the study of (air flow in) vibrated beds. The existing fluidized bed code needed to be adapted to allow for a vibrating bottom plate. The final model was found to be capable of describing realistic air velocity and pressure gradients induced by the accelerating and decelerating walls.

The first research topic which was addressed with the new model was wall-induced granular convection in vertically vibrated granular beds. In addition, a pseudo-2D experimental set-up containing glass particles ($d_p \sim 2.5$ mm) was constructed. The convection rolls were generated via a well-defined surface roughness, obtained by attaching glass particles to the side walls. The convection rolls are visible at the principle cell faces of the set-up, so that a non-intrusive optical measurement technique - particle image velocimetry (PIV) - can be employed to obtain particle velocity information. The convection strength was estimated from the velocity vectors and it was found that the model was capable of predicting most of the trends in the experiments. In particular, both in experiments and simulations it was observed that the convection strength at constant acceleration (Γ) decreases as the vibration frequency (f_z) increases, which has also been reported in literature. Also, it was found that the width of the down flow region near the walls was approximately constant. A quantitative comparison proves difficult however, since the experimental system often showed limited reproducibility. It was further found that the convection strength was generally over-predicted in the simulations. One reason could be that the actual wall friction at the principle cell faces in the experiments was larger than assumed in the simulations. Another reason was that the simulation results were found to be dependent on the value of the spring stiffness used in the soft-sphere collision model: an increased stiffness decreased the convection strength.

As a second research topic, the effect of air on the density segregation of fine ($d_p \sim 0.1$ mm), equal-sized bronze and glass particles under vertical vibrations was studied. The segregation phenomena were first observed by King and co-workers in experiments. Depending on the vibration parameters, two main segregation forms could be observed, namely, (i) a bronze layer situated on top of a glass layer or (ii) a bronze layer ‘sandwiched’ between two glass layers. They constructed a phase-diagram of acceleration vs. frequency, in which each region corresponds to a typical segregation behavior. In this work, DPM was used to investigate this system by numerical simulations and it was found that the model was capable of predicting the two main segregation forms in roughly the same regions of the phase diagram as was found experimentally. The next step was to investigate the origin of these remarkable segregation phenomena, which was not clear from the experimental data. On the basis of the detailed numerical data, it was found that two distinct mechanisms were responsible for the segregation. (i) For low vibration frequencies, the difference in acceleration from the gas drag causes the bronze to gradually move to the top, due to the pumping of air in combination with the cyclic compaction and decompaction of the bed. This effect appears to be very robust and relatively independent of the gas and particle properties that we studied. (ii)

For higher vibration frequencies, the difference in inertial mass in collisions causes the bronze clusters on top to penetrate the glass-rich layer below in the second part of the vibration cycle, when the falling bed is hitting the bottom plate. For lower frequencies and higher amplitudes, the first mechanism dominates due to the longer period of free flight, and bronze will always move to the top. For higher frequencies and lower amplitudes, the combination of mechanism (i) and (ii) leads to the sandwich formation. The formation of the sandwich structure, however, appears to be a rather subtle process, and the state is much less robust. It has not been found in previous simulation studies, and also turns out to be rather sensitive on the particle properties: under the same shaking conditions, the bronze layer was found to end up in the middle (i.e., sandwich), on top *or* on the bottom, depending on the values for the friction coefficients.

Up till now, systems have been studied where the particles were agitated by vertical vibrations only. However, vibrations may also be applied to a gas-fluidized bed. A benefit of this type of operation is that the fluidization quality of cohesive powders may be improved, since the vibrations are capable of suppressing the formation of stable channels. In this thesis, the main focus was on the effects of vibration on the bubble behavior and solids circulation. To investigate this, experiments and complementary simulations were performed with glass particles ($d_p \sim 1.0$ mm). From visual inspection it was found that - depending on the vibration parameters - the bubble behavior could be very different from conventional gas-fluidization, namely that the vibrations suppress bubble formation, leading to fewer, but also larger bubbles. This was especially true for vibrations with a large vibration amplitude, where experimentally a behavior reminiscent of that of a spout-fluid bed could be observed. In the experiments, PIV was employed to determine the time-averaged solids circulation patterns which were compared to those obtained from the simulations. In both simulations and experiments, it was found that the solids circulation rate at constant f_z increased with acceleration Γ, in agreement with experimental findings in literature; by contrast, no clear trend could be observed at constant Γ when the value of f_z was varied, which was somewhat surprising, since in the visual observations the bubble behavior was clearly affected. Gas-vibro fluidization generally displayed larger circulation rates as compared to conventional gas-fluidization. Quantitative comparison of the simulations and experiments yielded that the circulation rate in the simulations was larger than in the corresponding experiments. From a limited parameter study in the simulations, it was found that this may be caused by the wall friction which is probably larger in the experiments than assumed in the simulations.

A different application of the code is the impact of a solid body ('intruder') on a static, loosely packed granular bed. In experiments performed by Lohse and coworkers, on impact a crown-like splash is created, followed by a jet shooting out at the position of the impact. They developed a theoretical analysis for the description of the phenomenon, which was investigated using DPM. A one-to-one modeling of the experimental system proved impossible however: in order to keep the number of particles below 2 million, the particles in the simulations had to have a diameter of 500 μm instead of the 40 μm of the experiments. In addition, the phenomenon was investigated in a pseudo-2D geometry so that the intruder - which was not coupled to the gas phase - resembled a disc. Despite these restrictions, it was found that the model was capable of qualitatively describing the impact phenomenon, although the visual effects were much less dramatic than in the experiments. It was found, however, that the very loose packing of the experiment ($\varepsilon_s = 0.40$) could not be obtained with the perfectly round spheres in the simulation model. The numerical model allowed for a test of the assumptions underlying the theoretical analysis of the impact phenomenon by Bergmann *et al.*. It was found that two assumptions in the theoretical scaling law were not satisfied, but this could very well be caused by the fact that the simulated system differs quite strongly from the experimental one.

Recently, the role of interstitial air on physical phenomena has received much attention. It was found not only to play a crucial role in the jet formation or the bronze/glass segregation studied earlier, but also in the occurrence of the *reverse* Brazil Nut effect, where the large intruder particle - subject to vibrations - goes down instead of up. In the modeling of such systems however, the size differences between the intruder and the much smaller 'background' particles makes that the treatment of the gas-solid coupling is non-trivial since the large particle exceeds the computational grid size. In the thesis, a first attempt has been made to incorporate the immersed boundary method (IBM) - which can be used to describe the gas-solid interaction of such a large particle - into DPM. Although the model is still far from perfect (in particular it suffers from grid-size and time step dependence), it has been used - as a first application - to measure the viscosity of the granular medium by using a method similar to the 'falling sphere' method used in experiments for determining the viscosity. In our case, the intruder is pulled through the granular bed with constant velocity. The total drag, which contains a contribution from the gas phase and from collisions with the background particles, was measured and it was found that the gas drag was much larger than expected, which was most likely connected to the relatively coarse computational grid that was used. The drag force was measured as function of the intruder velocity and - assuming that the Stokes-Einstein drag law is valid for the gas-solid suspension - values for the granular viscosity in the range 0.6-0.9 Pa.s were found for this particular system. Despite the relatively coarse computational grids employed in the simulations, the computed viscosities are close to the range reported in literature.

Samenvatting

Geschudde granulaire materie kan een verscheidenheid aan interessante fenomenen vertonen en is daarom een populair onderzoeksgebied binnen de wetenschap. Afhankelijk van de deeltjeseigenschappen en de schudcondities kan het gedrag van de deeltjes sterk verschillen; ze kunnen zich gedragen als een vaste stof, een vloeistof of zelfs een gas, resulterend in een rijk geschakeerde collectie fenomenen zoals 'hoop vorming', convectie, patroonvorming, etc. Het verwerken van deeltjesmengsels kan zelfs een (ongewenste) ontmenging induceren. De verschijnselen worden nog gecompliceerder voor kleine deeltjes, omdat dan nog andere krachten, zoals die van interstitieel gas, belangrijk worden; dit leidt tot nieuw en vaak verrassend gedrag van granulair materiaal. Bij de bestudering van deze complexe systemen kunnen numerieke simulaties een belangrijke rol spelen, omdat langs deze weg inzichten verkregen kunnen worden die moeilijk of niet langs experimentele weg toegankelijk zijn. Tevens is het relatief eenvoudig om het effect van individuele parameters te onderzoeken omdat deze eenvoudig in- en uitgeschakeld kunnen worden. Bovendien kan een voorstudie met simulaties potentieel interessante operatiegebieden identificeren, die verder onderzocht kunnen worden in meer gefocusseerde experimenten. In dit proefschrift zal het stromings- en ontmenggedrag van geschud granulair materiaal worden onderzocht met behulp van experimenten en numerieke berekeningen. Een tweede thema is het gedrag van grote deeltjes die bewegen door een bed van kleinere deeltjes. De specifieke onderwerpen die bestudeerd worden zijn: (i) wand-gedreven granulaire convectie, (ii) lucht-gedreven ontmenging van kleine bronzen en glazen deeltjes, (iii) deeltjescirculatie in een gevibreerd wervelbed, (iv) dynamica van een groot deeltje bij inslag op een bed met granulair materiaal, en (v) dynamica van een groot deeltje dat door een gefluïdiseerde suspensie van deeltjes wordt getrokken.

Voor de beschrijving van gas-vast twee-fasen stroming is een aantal numerieke modellen beschikbaar. Deze modellen verschillen in de mate van gedetailleerdheid, en hieraan gekoppeld ook de mogelijke schaalgrootte van de beschreven systemen. Het is gebleken dat het discrete deeltjes model (DPM) het meest geschikt is voor de in dit proefschrift onderzochte systemen, omdat het model de juiste mate van detaillering verenigt met de noodzakelijke schaalgrootte.

In DPM wordt voor individuele deeltjes de trajectorie berekend op basis van de tweede wet van Newton. Botsingen tussen deeltjes worden afgehandeld door een zachte-bollen botsingsmodel, terwijl de gasstroming wordt beschreven met de volume-gemiddelde Navier-Stokes vergelijkingen. De wisselwerking tussen gas en deeltjes wordt beschreven met empirische drag vergelijkingen, waarbij de modelimplementatie van de koppeling zodanig is dat de uitgewisselde hoeveel impuls behouden blijft. Dit type model wordt veelvuldig gebruik voor de beschrijving van wervelbedden en bleek ook het meest geschikt voor de beschrijving van (de gasstroming in) geschudde bedden. Hiertoe werd een beschikbaar model aangepast voor vibraties en het resulterende model bleek in staat de door de vibraties geïnduceerde gassnelheid en drukgradiënt goed te beschrijven.

Het eerste onderwerp dat met het nieuwe model werd bestudeerd is wandgedreven granulaire convectie in verticaal geschudde bedden. Tevens werd een pseudo-2D experimentele opstelling geconstrueerd met hierin glazen deeltjes ($d_p \sim 2.5$ mm). De convectierollen werden gegenereerd middels een goed gedefinieerde wandruwheid, die werd verkregen door op de wand glazen deeltjes te bevestigen. De convectierollen zijn dan zichtbaar in de hoofdvlakken van de opstelling, en middels een niet-invasieve meettechniek - Particle Image Velocimetry (PIV) - kunnen deeltjessnelheden verkregen worden. De convectiesterkte werd afgeschat aan de hand van de snelheidsvectoren, en het bleek dat het model in staat was de meeste trends in de experimenten te beschrijven. In zowel model als experiment werd gevonden dat bij een constante versnelling (Γ) de convectiesterkte afnam met een toename van de schudfrequentie (f_z), een waarneming die ook in de literatuur gerapporteerd is. Tevens werd gevonden dat het gebied (nabij de wanden) waarin deeltjes naar beneden stromen bij benadering een constante breedte heeft. Een kwantitatief vergelijk was moeilijk omdat de experimenten slechts beperkt reproduceerbaar bleken. Er werd verder gevonden dat de convectie sterkte werd overschat in de simulaties. Een reden kan zijn dat de wandfrictie op de hoofdvlakken hoger was dan werd verondersteld in de simulaties. Een andere reden was dat de simulatieresultaten nog enige afhankelijkheid van de veerconstante van het zacht-bollen model vertoonden: het verhogen van de veerconstante verlaagde de convectiesterkte.

Als tweede onderwerp werd de ontmenging van kleine ($d_p \sim 0.1$ mm) bronzen en glazen deeltjes in lucht onder verticale vibratiecondities onderzocht. Deze ontmenging werd voor het eerst in experimenten waargenomen door King *et al.*. Afhankelijk van de schudparameters konden in de experimenten twee regimes onderscheiden worden, namelijk (i) een laag brons gepositioneerd bovenop een laag glas, of (ii) een laag brons 'sandwiched' tussen twee lagen glas. King en medewerkers construeerden een 'fasen-diagram' van de versnelling vs. frequentie, waarin elk gebied correspondeert met een typisch ontmenggedrag. In dit proefschrift werd dit systeem onderzocht met behulp van DPM simulaties en het model bleek in staat de twee hoofdvormen in ruwweg dezelfde gebieden als waargenomen in de experimenten te voorspellen. De volgende stap was het onderzoek naar de oorsprong van deze opmerkelijke ontmenging, welke niet duidelijke was gevonden uit de experimentele studie. Op basis van gedetailleerde analyse van de simulatieresultaten werd gevonden dat de ontmenging veroorzaakt werd door twee verschillende mechanismen: (i) Bij lage schudfrequenties veroorzaakt het verschil in versnelling door de gasfase van glas en brons dat het brons gestaag naar boven gaat, vanwege het pompen van de lucht in combinatie met de cyclische compactie en de-compactie van het granulaire bed. Dit effect is zeer robuust en relatief onafhankelijk van de bestudeerde gas- en deeltjeseigenschappen. (ii) Bij hoge schudfrequenties werd gevonden dat het verschil in *trage* massa van glas en brons tijdens botsingen ervoor zorgt dat de bovenop gelegen brons clusters de ondergelegen glaslaag binnendringen gedurende het tweede deel van de vibratie cyclus, waarin het vallende bed inslaat op de bodem. Het verschil in *zware* massa (d.w.z. het ondervinden van een verschillende zwaartekracht) speelt nauwelijks een rol. Bij lage schudfrequenties en hogere schudamplitudes domineert het eerste mechanisme vanwege de langere vrije-vlucht fase, en daarom zal het brons altijd naar boven gaan. Voor hogere frequenties en lagere amplitudes zal de combinatie van mechanisme (i) en (ii) leiden tot een sandwich formatie. De vorming van de sandwich blijkt echter een subtiel proces te zijn en deze configuratie is veel minder robuust. Ze is niet eerder waargenomen in simulatie studies en bleek ook gevoelig voor de deeltjeseigenschappen; bij dezelfde schudcondities werd gevonden dat de bronslaag in het midden, bovenop of zelfs onderin kon eindigen, afhankelijk van de mate van frictie in deeltjes-deeltjes botsingen.

Tot zover werden systemen bestudeerd waarbij de deeltjes slechts geagiteerd werden middels verticale vibraties. Vibraties kunnen echter ook aangewend worden bij wervelbedden. Het nut hiervan is dat het fluïdisatiegedrag van cohesieve poeders kan worden verbeterd, omdat de vibraties de vorming van stabiele kanalen in het granulaire materiaal kunnen onderdrukken. In dit proefschrift ligt de nadruk op het effect van de vibraties op het bellengedrag en circulatie van deeltjes. Hiertoe zijn experimenten en complementaire simulaties uitgevoerd met glazen deeltjes ($d_p = 1.0$ mm). De visuele waarnemingen lieten zien dat het bellengedrag tijdens gas-vibro fluïdisatie sterk kon verschillen van conventionele gas-fluïdisatie, namelijk dat de vibraties belvorming konden onderdrukken. Dit leidt tot minder, maar ook grotere bellen. Dit was met name het geval voor vibraties met een grote amplitude, waarbij in de experimenten een gedrag werd geobserveerd dat verwant is aan spout-fluïdisatie. Voor het bepalen van de tijdsgemiddelde deeltjesstroming in de experimenten werd PIV toegepast. Zowel in de simulaties als de experimenten werd gevonden dat de deeltjesstroming bij constante f_z toeneemt met de acceleratie Γ, in overeenstemming met experimentele bevindingen uit de literatuur. Echter, geen duidelijke trend kon worden onderscheiden bij constante Γ als de waarde van f_z werd gevarieerd. Dit was verassend, aangezien het bellengedrag duidelijk was beïnvloed. Over het algemeen werd bij gas-vibro fluïdisatie een hogere circulatiesnelheid van deeltjes gemeten, in vergelijking met conventionele gas-fluïdisatie. Uit een kwantitief vergelijk tussen simulaties en experimenten kwam naar voren dat de circulatie sterkte in de simulaties groter was dan die in de complementaire experimenten. Een beperkte parameterstudie in de simulaties liet zien dat deze waarneming veroorzaakt kan zijn door de wand frictie die vermoedelijk hoger was in de experimenten, dan aangenomen in de simulaties.

Een tweede toepassing van het model is de inslag van een voorwerp ('intruder') op een statisch, los gepakt granulair bed. In experimenten die uitgevoerd zijn door Lohse *et al.*, blijkt dat bij inslag een kroon-vormige 'splash' wordt gevormd, waarna een jet ontstaat op de impact locatie. Lohse en medewerkers ontwikkelden een eenvoudig model voor de beschrijving van het fenomeen, welke met DPM werd onderzocht. Echter, een ‘een-op-een’ modelering van het experimentele systeem bleek niet mogelijk; het was noodzakelijk de 40 μm deeltjes te vervangen door 500 μm deeltjes, opdat het aantal deeltjes onder de 2 miljoen zou blijven. Bovendien werd het fenomeen onderzocht in een pseudo-2D geometrie zodat de intruder - die niet was gekoppeld aan de gas fase - op een schijf leek. Ondanks deze beperkingen bleek dat het model in staat was een kwalitatieve beschrijving van de experimenten te geven, hoewel de visuele effecten veel minder uitgesproken waren dan in de experimenten. Er werd echter gevonden dat de losse pakking in de experimenten ($e_s = 0.40$) niet verkregen kon worden met de perfect ronde bollen van het simulatiemodel. Met het numerieke model konden de aannames van de theoretische analyse van het inslagverschijnsel door Bergmann *et al.* onderzocht worden. Het bleek dat aan twee aannames van de theoretische schalingswet niet werd voldaan, maar dit kan ook veroorzaakt zijn door de grote verschillen tussen het experimentele en model systeem.

Recentelijk heeft het effect van het interstitiële gas op fysische fenomenen veel aandacht verkregen. Het bleek dat dit effect niet alleen een cruciale rol speelt bij de eerder behandelde jet vorming of bij de brons/glas scheiding, maar ook bij het optreden van het *omgekeerde* ‘Brazil Nut’ effect, waarbij een groot deeltje naar beneden beweegt, in plaats van omhoog, wat normaalgesproken wordt waargenomen. Bij het modeleren van dit soort systemen maakt het verschil in grootte tussen intruder en de kleinere beddeeltjes dat de behandeling van gas-vast interactie niet triviaal is, omdat de intruder groter is dan de controle volumes gebruikt voor het oplossen van de Navier-Stokes vergelijkingen. In dit proefschrift wordt een eerste poging ondernomen om de ‘immersed boundary’ methode (IBM) - welke gebruikt kan worden voor de beschrijving van de gas-vast interactie van een dergelijk groot deeltje - in DPM te integreren. Hoewel het model nog verre van perfekt is (het bevat nog grid en tijdstap afhankelijkheden), is het - als een eerste toepassing - gebruikt om de viscositeit van een granulair medium te meten. In ons geval wordt de intruder met constante snelheid door het granulaire medium getrokken. De totale drag, welke een bijdrage van de gasfase en van botsingen met de beddeeltjes bevat, werd gemeten en de bevinding was dat de gas drag veel groter was dan verwacht. Waarschijnlijk werd dit veroorzaakt door het relatief groffe grid. De drag kracht werd gemeten als functie van de intruder snelheid en - bij aanname van een Stokes-Einstein drag relatie voor het gas-vast systeem - werden voor de granulaire viscositeit waarden tussen 0.6-0.9 Pa.s gevonden voor dit specifieke systeem, hetgeen dicht de experimenteel gevonden waarden ligt.

1

General Introduction

1.1 Granular matter

Granular matter is one of the most manipulated materials in the world. The handling and processing are far from trivial, however, since granular matter can behave as a gas, a liquid or a solid, depending on the processing conditions. It has been estimated that 40 % of the capacity of our industrial plants is wasted because of problems related to the transport of these materials [13] and it is therefore clear that a better understanding of its behavior is of the utmost importance, not only out of scientific curiosity, but also for economic reasons. Often, the problems that arise when dealing with granular material can be attributed to either (i) undesired segregation of particle mixtures and (ii) transportation / manipulation problems, as illustrated in the following two examples.

When granular materials with different particle properties, for example density or size, are processed, segregation may occur, which is undesirable when homogeneous mixtures - important in for example the pharmaceutical industry - are required. Such segregation phenomena can also take place at home: when a pack of mixed nuts is shaken, the large nuts (such as the Brazil Nuts) end on top of the smaller ones (‘Brazil Nut effect’).

An example of equipment which is notoriously difficult to operate is the hopper, which is essentially a container with an outlet, used to feed bulks of solids into a process. In the design of such equipment it is - amongst others - important to take the particle properties into account. Wrong hopper design, or using granular material with sufficiently different properties than the design was intended for, may lead to for example bad flow behavior at the outlet. Often, a telling sign of such problems is the dented metal (also called ‘hammer rash’) found near the hopper outlet, usually caused by personnel who wanted to ‘facilitate’ the granular flow.

In addition to industry, the intricacies of granular media have also attracted scientists for centuries. Already in the 1800s, Faraday experimentally studied clustering of vibrated granular material into a ‘Peculiar class of Acoustical Figures’ [1] and Janssen [20] found that in granular media the pressure head did not increase indefinitely with granular bed height, such as in regular fluids. This effect allows for the sand in an hourglass to flow at a constant rate. More recently, formation and stability of heaps [3], transport of granules and segregation phenomena under vibrations (i.e., the Brazil Nut Effect [2]) have received much attention [15,19]. Also the hydrodynamic study of gas-fluidized beds - which are much used in the cracking of oil (Fluid Catalytic Cracking) - is an important branch of granular matter research.

1.2 Numerical modeling of gas-solid systems

Until recently, most of the research on vibration induced segregation was concerned with ‘dry’ systems, where the effect of the interstitial air was ignored. For large and/or heavy particles this assumption is usually valid, but when the particles become small ($d_p < 1$ mm) the gas forces must be taken into account. An example is the famous Brazil Nut effect. One of the reasons for segregation is a steric effect, where the small particles can move underneath the large sphere during a vibration cycle. Recently, however, it was found that also air drag may be important [15–17]: when choosing the right combination of shaking conditions, air pressure, size ratio and particle materials, the large sphere may even sink.

Computer simulations can play an important role in the research of granular material, since they can provide data that is not accessible in experiments (such as local contact and drag forces), and also it is relatively easy to study the effects of parameters separately. Moreover, preliminary simulations can provide a window of desired operating conditions that can be explored more fully in focused experiments. As mentioned earlier, in the past years, the numerical simulations of granular matter under vibration have mainly been concerned with 'dry' systems, i.e., granules in vacuum. One of the reasons is that a proper modeling of the surrounding air is a task that is far from trivial. The few numerical studies of granular matter with air that have appeared in literature in the past use a simplified description of the Navies-Stokes equations with a Darcy-type gas-solid interaction, thereby neglecting inertial effects [4–6]. Only recently, King and co-workers [7] have included the full Navier-Stokes equations in the vibrated granular bed.

In the field of gas-fluidized beds, an accurate description of the gas flow and the coupling between gas and solid is crucial and such models have already proven their usefulness in the field of chemical engineering, where gas-fluidized beds are widely used for chemical conversions. With respect to the models for gas-particle flows in fluidized systems, four different modeling levels can be distinguished. Basically, the higher level models can be used to describe industrial sized systems, sacrificing the details. The lower level models contain more details, but are limited in the (computationally) feasible system size. See Fig. 1.1.

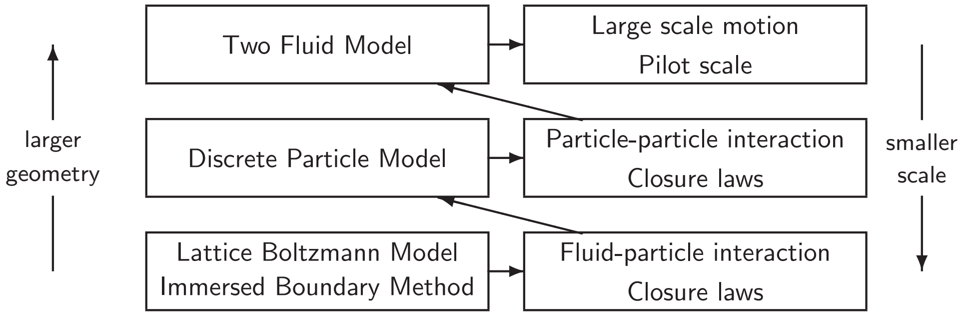

Figure 1.1: *Multi-level modeling approach. The amount of detail (and computational effort) increases from top to bottom. The feasible number of particles increases from bottom to top.*

At the lowest level, the Lattice Boltzmann model and alternatively the Immersed Boundary Method [11] can be used. These models are based on first principles, and input of empirical data is minimal. The gas phase is fully resolved, i.e., the length scale of the gas phase description is much smaller than that of the individual particles. Appropriate boundary conditions on the particle surface take care of the gas-solid coupling. Drawback of these methods is the small number of particles ($\sim$ 1,000) than can be handled, due to restrictions in memory and CPU-time.

At the intermediate level, the discrete particle model [12] is found, where the maximum number of particles that can be handled on a modern PC is typically around 1 million. The length scale of the gas phase description is larger than the particle diameter and therefore drag closures are required to describe the interaction between gas and solid. Such gas-particle drag closures can be empirical in nature (such as the famous Ergun equation) or may be obtained from the more fundamental Lattice Boltzmann model [8–10].

At an even higher level, the multi-fluid model [14, 18] can be found. This model considers the gas phase and the gas/particle emulsion phase as two interpenetrating liquids that may be described by the Navier-Stokes equations. The model requires closures for 'liquid' properties of the gas/particle emulsion, such as pressure and viscosity, which may be obtained from the Kinetic Theory of Granular Flow. A drawback is that the model still requires that a sufficiently fine grid is used to capture heterogeneous structures (i.e., bubbles or clusters), which limits the size of the modeled systems.

At the highest rung - but not shown in Fig. 1.1 - the discrete bubble model can be found, with which industrial size equipment can be described. As the name implies, the model is derived from a model developed for gas-liquid systems, where the bubbles are considered individual entities, while the liquid is considered a continuum which can be described using the Navier-Stokes equations. For the usage in gas-particle systems, the emulsion phase is considered a Newtonian liquid and the bubbles are discrete spheres.

In this thesis, we have extended the discrete particle model (DPM) to include vertical vibrations, so that they also may be applied to systems where particles are shaken. As a result, the effects of interstitial gas on segregation and flow behavior can now be studied in detail. One of the main reasons for choosing the DPM model is that for the systems that we study in this thesis, a high level of detail is required: on the one hand we need a detailed description of the particle-particle interactions since the effects of these parameters are unknown and a discrete particle model handles these in a natural way via the collision model. The continuum models lack such level of detail. On the other hand, we need to model a sufficient number of particles (typically larger than 20,000), which excludes a description of the lowest level, where we are limited to approximately a 1,000 particles. In this trade-off, the model of choice is the discrete particle model.

1.3 Outline of the thesis

In this thesis, the primary focus is on the flow behavior of particles subject to vertical vibrations. As a second subject we also study the behavior of large particles in assemblies of (much) smaller ones.

In chapter 2, the numerical model for the description of gas-particle flow is presented. The emphasis is on the treatment of the moving bottom plate and the verification of its implementation.

In chapter 3, wall-induced granular convection rolls are investigated. The capability of the numerical model to describe the convection strength as a function of the vibration parameters was investigated. To this end, whole-field particle velocity fields have been measured in experiments, using PIV. The findings were compared to the model results.

In chapter 4, we investigate the density segregation of a mixture of fine, equal-sized bronze and glass particles by numerical simulations. The model results were compared with experiments from literature and following this, an explanation for different experimentally observed segregation phenomena - which were a function of the vibration parameters - is proposed.

In chapter 5, the numerical model is used to investigate the behavior of granular material under conditions of both vibration and gas-fluidization. For this mode of operation, also known as gas-vibro fluidization, the focus is on the effects of vibration on the solids circulation rate. An experimental study was carried out in order to validate the model predictions.

In chapter 6, the capability of the model for describing impact phenomena of a large intruder on static granular assemblies of small particles is investigated. The visual observations were compared qualitatively with experiments from literature. Following this, simulation data for the channel collapse were compared with theory.

In chapter 7, a first attempt is made to incorporate the immersed boundary method (IBM) - which can be used to describe the gas-solid interaction of a large sphere - into DPM. The main focus is on the numerical implementation of the sphere. As a preliminary test of the hybrid model, the total force acting upon an intruder being pulled through a fluidized granular bed was investigated and from this an estimate for the granular viscosity was made.

Bibliography

[1] M. Faraday, ‘On a Peculiar Class of Acoustical Figures; and on Certain Forms Assumed by Groups of Particles upon Vibrating Elastic Surfaces’, Phil. Trans. Roy. Soc. London **121**, p. 299 (1831).

[2] A. Rosato, K.J. Strandburg, F. Prinz, R.H. Swendsen, ‘Why the Brazil Nuts Are on Top: Size Segregation of Particulate Matter by Shaking’, Phys. Rev. Lett. **58**, p. 1038 (1987).

[3] H.K. Pak, E. Van Doorn, R.P. Behringer, ‘Effects of Ambient Gases on Granular Materials under Vertical Vibration’, Phys. Rev. Lett. **74**, p. 4643 (1995).

[4] S. McNamara, E.G. Flekkøy, K. Jørg, K.J. Måløy, ‘Grains and Gas Flow: Molecular Dynamics with Hydrodynamic Interactions’, Phys. Rev. E **61**, p. 4054 (2000).

[5] E.G. Flekkøy, S. McNamara, K.J. Måløy, ‘Structure Formation and Instability in a Tube of Sand’, Phys. Rev. Lett. **87**, 134302 (2001).

[6] P. Biswas, P. Sánchez, M.R. Swift, P.J. King, 'Numerical Simulations of Air-driven Granular Separation', Phys. Rev. E **68**, 050301 (2003).

[7] R.J. Milburn, M.R. Swift, P.J. King, 'The effects of fluid-driven convection on the separation of binary mixtures', in 'Powders and Grains', Edited by Garcia-Rojo, Hermann and McNamara, p. 1029 (Taylor & Francis Group, London, 2005).

[8] R.J. Hill, D.L. Koch, A.J.C. Ladd, 'The First Effects of Fluid Inertia on Flows in Ordered and Random Arrays of Spheres', J. Fluid Mech. **448**, p. 243 (2001).

[9] M.A. van der Hoef, R. Beetstra, J.A.M. Kuipers, 'Lattice-Boltzmann simulations of low-Reynolds-number flow past mono- and bidisperse arrays of spheres: results for the permeability and drag force', J. Fluid Mech. **528**, p. 233 (2005).

[10] R. Beetstra, M.A. van der Hoef, J.A.M. Kuipers, 'Drag force of intermediate Reynolds number flow past mono- and bidisperse arrays of spheres', AIChE Journal, **53**, p. 489 (2007).

[11] M. Uhlmann, 'An immersed boundary method with direct forcing for the simulation of particulate flows', J. Comp. Phys. **209**, p. 448 (2005).

[12] B.P.B. Hoomans, J.A.M. Kuipers, W.J. Briels, W.P.M. van Swaaij, 'Discrete particle simulation of bubble and slug formation in a two-dimensional gas-fluidised bed: a hard-sphere approach', Chem. Eng. Sci. **51**, p. 99 (1996).

[13] H.M. Jaeger, S.R. Nagel, R.P. Behringer, 'Granular solids, liquids, and gases', Rev. Mod. Phys. **68**, p. 1259 (1996).

[14] J.A.M. Kuipers, K.J. van Duin, F.P.H. van Beckum, W.P.M. van Swaaij, 'A numerical model of gas-fluidized beds', Chem. Eng. Sci. **47**, p. 1913 (1992)

[15] M.E. Möbius, B.E. Lauderdale, S.R. Nagel, H.M. Jaeger, 'Size separation of granular particles', Nature **414**, p. 270 (2001).

[16] M.E. Möbius, X. Cheng, G.S. Karczmar, S.R. Nagel, H.M. Jaeger, 'Intruders in the Dust: Air-Driven Granular Size Separation', Phys. Rev. Lett. **93**, 198001 (2004).

[17] M.E. Möbius, X. Cheng, P. Eshuis, G.S. Karczmar, S.R. Nagel, H.M. Jaeger, 'Effect of air on granular size separation in a vibrated granular bed', Phys. Rev. E **72**, 011304 (2005).

[18] M.J.V. Goldschmidt, J.A.M. Kuipers, W.P.M. van Swaaij, 'Hydrodynamic modelling of dense gas-fluidised beds using the kinetic theory of granular flow: effect of coefficient of restitution on bed dynamics', Chem. Eng. Sci. **56**, p. 571 (2001).

[19] N. Burtally, P.J. King, M.R. Swift, 'Spontaneous Air-Driven Separation in Vertically Vibrated Fine Granular Mixtures', Science **295**, p. 1877 (2002).

[20] H.A. Janssen, 'Versuche über Getreidedruck in Silozellen', Z. Vereines Deutsch. Ing. **39**, p. 1045 (1895).

2

A Numerical Model for Vibrated Beds

ABSTRACT

In this chapter, the discrete particle model is presented. In this model, the gas-phase is described using the volume-averaged Navier-Stokes equation, while the particles are individual entities that interact with each-other via a soft-sphere collision model. The interaction between the particles and gas is two-way and handled via (empirical) drag relations. The model was further developed to include vertical vibrations, and the implementation of vibrating walls into the model is discussed in detail, as well as the numerical verification of the method. Apart from this, a short theoretical background is provided for the immersed boundary method (IBM), which is a model in which the gas-solid interaction is fully resolved. The method is employed in an explorative fashion in Chapter 7.

2.1 Introduction

The accurate modeling and simulation of gas-solid two-phase flows has challenged the scientific community for decades. The importance of these systems for industrial applications has already been pointed out in Chapter 1. In this chapter we now focus on the computational and modeling strategies that are available to study the systems of interest. In this, we will make a distinction between the description of the particle phase and the one that is used for the gas phase.

The systems we consider are made up of well-defined particles, such as spheres. The most realistic description of the solid phase would therefore be a discrete particle model, where the trajectory of each individual particle is computed. This is to be preferred over a continuous model, since the collisional interaction - which determines the amount of energy being dissipated - can be more accurately modeled in a discrete particle description. It is well known that the dissipation strongly affects the behavior of particles in gas flows, such as in the gas-fluidized bed [14] and therefore a detailed description of the particle interactions (i.e., collision model) is required if these effects are to be studied. Two types of collision model are widely used, namely the hard sphere model and the soft sphere model. The hard sphere model is event driven and only binary, instantaneous collisions take place. The resulting particle velocities are obtained from an impulse balance, which can be solved analytically. The soft sphere model is time driven and multiple particle contacts are possible, where the particle velocities are calculated from contact forces via numerical integration. The hard sphere model is often used in dilute granular flows, but is less efficient in dense regions where many collisions take place. By contrast, the soft sphere model can be used in dilute as well as dense granular systems. Although both models are available in our group, the soft sphere model is most suitable for the dense systems that we plan to study, and we will not further discuss the hard-sphere model here.

There are several options for the description of the gas phase in the presence of a solid phase, but all of these can be traced back to two types, namely fully resolved and unresolved gas flow. For fully resolved flow (i.e., Lattice Boltzmann Simulations [8] or the Immersed Boundary methods [10, 13]), the gas phase is solved on a length scale that is much smaller than the size of the particles. With the appropriate boundary condition on the surface of the particles, the force of the gas acting on the particles is calculated directly. Fully resolved flow computations, however, are expensive from CPU and computer memory point of view and therefore the size of such systems is usually limited to approximately a thousand particles. For unresolved flow, the gas phase is solved on length scales larger than the particles and therefore the computational effort is much smaller. However, it is now necessary to introduce drag relations in order to take the gas-particle interaction into effect. For the simulations described in this thesis, we use an unresolved type of description - at least with respect to the interaction of the gas with the *bed* particles - which we will hence call the discrete particle model. Note that the dynamics of large bodies present in the system (such as the vibrating bottom or intruder (Chapter 7)) will be modeled fully resolved.

In this chapter we will describe the discrete particle model that was developed for use under both vibration and gas-fluidization conditions. The model considers individual spherical particles that interact with each other via a soft sphere type of collision model. The surrounding gas phase is described using volume-averaged Navier-Stokes equations, where the interaction between the individual particles and the gas phase is included via (empirical) drag relations.

Since there have been elaborate accounts on the discrete particle model for gas-fluidized beds in literature (see [10] and references therein), we focus in this chapter on the implementation of the vibrating walls, which is described in section 2.3. Before doing so, however, we first give a brief description of the discrete particle model for gas-solid flows in section 2.2.

2.2 Discrete particle model

2.2.1 Equations of motion for the particulate phase

The position vector $\mathbf{r}_i$ of each individual particle i (mass m_i, diameter d_i) follows from Newton's law:

$$m_i \frac{\mathrm{d}^2\mathbf{r}_i}{\mathrm{d}t^2} = \mathbf{F}_{i,c} + \mathbf{F}_{i,g} + \mathbf{F}_{i,d} + \mathbf{F}_{i,\nabla p} \ . \tag{2.1}$$

In this equation, $\mathbf{F}_{i,g} = m_i\mathbf{g}$ is the gravitation force, and $\mathbf{F}_{i,\nabla p} = -\mathrm{V_i}\nabla p$ is the force due to pressure gradients in the gas phase, with $\mathrm{V_i}$ the volume of particle i. Furthermore, $\mathbf{F}_{i,c}$ is the total contact force, which is the sum of the individual contact forces exerted by all particles in contact with particle i, and $\mathbf{F}_{i,d}$ is the gas drag force. The latter two forces will be discussed in more detail in the next two sections.

2.2.2 Contact forces: $\mathbf{F}_{i,c}$

For the calculation of $\mathbf{F}_{i,c}$, a 3D linear spring/dashpot type of soft sphere collision model [10] following the lines of Cundall and Strack [4] is used. The coordinate system is shown in Fig. 2.1. From this model, it follows that the force in the normal direction between two particles a and b which are in contact is equal to:

$$\mathbf{F}_{ab,n} = -k_n\delta_n\mathbf{e}_{ab,n} - \eta_n\mathbf{v}_{ab,n} \ . \tag{2.2}$$

In Eq. 2.2, k_n is the spring stiffness [N/m], δ_n the overlap between the particles [m], $\mathbf{e}_{ab,n}$ the unit vector, η_n the damping coefficient [Ns/m], $\mathbf{v}_{ab,n}$ the velocity difference [m/s], all for the normal direction, indicated by the subscript n. The unit vector in normal direction is defined as:

$$\mathbf{e}_{ab,n} = \frac{\mathbf{r}_b - \mathbf{r}_a}{|\mathbf{r}_b - \mathbf{r}_a|} \tag{2.3}$$

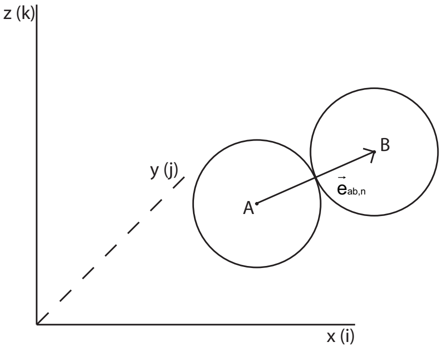

Figure 2.1: *Coordinate system and unit normal vector (Eq. 2.3). The indices i, j and k are used in the discretization of the Navier-Stokes equations and indicate the x-, y- and z-direction, respectively.*

The force in the tangential direction has a similar form

$$\mathbf{F}_{ab,t} = -k_t \delta_t \mathbf{e}_{ab,t} - \eta_t \mathbf{v}_{ab,t} \ , \tag{2.4}$$

where the variables have the same meaning as in Eq. 2.2, but now for the tangential direction, indicated with the subscript t. Note that Eq. 2.4 only applies when $|\mathbf{F}_{ab,t}| \leq \mu_{pp} |\mathbf{F}_{ab,n}|$. If the tangential force is larger, then frictional sliding occurs, which results in a force:

$$\mathbf{F}_{ab,t} = -\mu_{pp} |\mathbf{F}_{ab,n}| \, \mathbf{e}_{ab,t} \ , \tag{2.5}$$

where μ_{pp} [-] is the Coulomb friction coefficient of particle-particle contact.

In order to solve Eqns. 2.2 and 2.5, we need to know five parameters: the normal and tangential spring stiffness k_n and k_t, the normal and tangential damping coefficients η_n and η_t and the friction coefficient μ_{pp}

The coefficients of normal and tangential restitution, which determine the amount of kinetic/rotational energy that is dissipated in a collision, enter the model via the normal and tangential damping coefficients (η_n and η_t). The equation of motion for the collision process (Eq. 2.2) is essentially that of a damped harmonic oscillator. The equation can be solved using the appropriate initial conditions and the definition of the normal restitution coefficient (e_n)

$$e_n = -\frac{\mathbf{v}_{ab,n,end}}{\mathbf{v}_{ab,n,start}} \tag{2.6}$$

which results in the following relation between η_n and e_n

$$\eta_n = \begin{cases} \dfrac{-2 \ln e_n \sqrt{m_{\text{eff}} k_n}}{\sqrt{\pi^2 + \ln^2 e_n}} & \text{for} \quad \eta_n > 0 \\[2ex] 2\sqrt{k_n m_{\text{eff}}} & \text{for} \quad \eta_n = 0. \end{cases} \tag{2.7}$$

A similar analysis for the tangential spring leads to

$$\eta_t = \begin{cases} \dfrac{-2\ln e_t\sqrt{m'_{\text{eff}}k_t}}{\sqrt{\pi^2+\ln^2 e_t}} & \text{for} \quad \eta_t > 0 \\[2ex] 2\sqrt{k_t m'_{\text{eff}}} & \text{for} \quad \eta_t = 0. \end{cases} \tag{2.8}$$

The expressions for the reduced masses used in Eqns. 2.7 and 2.8 are

$$m_{\text{eff}} = \frac{m_a m_b}{m_a + m_b}, \qquad m'_{\text{eff}} = \frac{2}{7}\frac{m_a m_b}{m_a + m_b}. \tag{2.9}$$

In the case of particle-wall contact, particle b (the wall) is simply treated as a particle with infinite radius, so that

$$m_{\text{eff}} = m_a, \qquad m'_{\text{eff}} = \frac{2}{7}m_a. \tag{2.10}$$

The collision parameters that need to be specified are now the two spring stiffnesses (k_n and k_t) and the three collision parameters e_n, e_t and μ.

2.2.3 Fluid-particle drag force: $\mathbf{F}_{i,d}$

The gas drag force $\mathbf{F}_{i,d}$ on a single particle in the presence of neighboring particles cannot be evaluated analytically, and we have to resort to empirical expressions, which follow from pressure drop data and data for the terminal velocity of assemblies of spheres. We have used the Ergun [1] and Wen&Yu [2] correlations for the gas-solid drag, which is common in simulation models for dense gas-solid two-phase flow. In the Ergun and Wen&Yu model, the drag force is equal to

$$\mathbf{F}_{i,d} = 6\pi\mu_g R_p\left(\mathbf{u} - \mathbf{v}_i\right)\cdot \mathrm{F}(\mathrm{Re},\varepsilon)\ , \tag{2.11}$$

with

$$\mathrm{F}(\mathrm{Re},\varepsilon) = \begin{cases} \varepsilon^{-2.65}\left(1 + 0.15\,\mathrm{Re}^{0.687}\right) & \text{for} \quad \varepsilon > 0.8 \\[2ex] \dfrac{150}{18}\dfrac{1-\varepsilon}{\varepsilon} + \dfrac{1.75}{18}\dfrac{\mathrm{Re}}{\varepsilon} & \text{for} \quad \varepsilon < 0.8 \end{cases} \tag{2.12}$$

where R_p is the particle radius, μ_g is the dynamic gas viscosity [Pa.s] and $\mathbf{u}$ is the local flow velocity of the gas phase, while $\mathrm{Re} = 2R_p\rho_g\varepsilon\left|\mathbf{u} - \mathbf{v}_i\right|/\mu_g$ is the particle Reynolds number, with ρ_g the density of the gas phase. More recently, improved drag relations, obtained from fully resolved simulations such as the Lattice Boltzmann Model have been proposed [15].

$$\begin{aligned} \mathrm{F}(\mathrm{Re},\varepsilon) \ &= \ \frac{10\,(1-\varepsilon)}{\varepsilon} + \varepsilon^3\left(1 + 1.5\,(1-\varepsilon)^{1/2}\right) \\ &+ \frac{0.413\,\mathrm{Re}}{24\varepsilon}\left[\frac{\varepsilon^{-1} + 3\varepsilon(1-\varepsilon) + 8.4\,\mathrm{Re}^{-0.343}}{1 + 10^{3(1-\varepsilon)}\mathrm{Re}^{-(1+4(1-\varepsilon))/2}}\right]\ . \end{aligned} \tag{2.13}$$

In order to evaluate the drag force from Eq. 2.11, the local gas phase porosity ε

$$\varepsilon = \frac{V_{cell} - \sum_{i \in cell} V_i}{V_{cell}} \tag{2.14}$$

is evaluated for each cell, where V_i is the volume (located in the cell) of particle i and V_{cell} is the volume of the computational cell. The void fraction is updated each calculation cycle, of which a flow chart can be found in Appendix C.

2.2.4 Integration and time step

The equation of motion for each particle i can be integrated using any kind of method for ordinary differential equations. The simple first-order scheme is widely used and gives:

$$\mathbf{v}_{i,t+\Delta t} = \mathbf{v}_{i,t} + \mathbf{a}_{i,t} \cdot \Delta t \tag{2.15}$$

$$\mathbf{r}_{i,t+\Delta t} = \mathbf{r}_{i,t} + \mathbf{v}_{i,t+\Delta t} \cdot \Delta t \tag{2.16}$$

$$\omega_{i,t+\Delta t} = \omega_{i,t} + \mathbf{\Theta}_{i,t} \cdot \Delta t \tag{2.17}$$

with $\mathbf{a}_i$ the acceleration [m/s^2], $\mathbf{v}_i$ the velocity [m/s], $\mathbf{r}_i$ the location [m], ω_i the rotational velocity [rad/s] and $\mathbf{\Theta}_i$ the rotational acceleration [rad/s^2], all of particle i.

The maximum value that one can choose for the time step Δt depends on the duration of the contact. From an energy conservation point of view, the contact times for the normal as well as the tangential contact need to be the same, i.e.:

$$\sqrt{\frac{\pi^2 + (\ln e_n)^2}{k_n/m_{\text{eff}}}} = \sqrt{\frac{\pi^2 + (\ln e_t)^2}{k_t/m'_{\text{eff}}}} \tag{2.18}$$

Under the assumption that $e_n = e_t$, it follows that the relation between normal and tangential spring stiffness is

$$\frac{k_t}{k_n} = \frac{m_{\text{eff}}}{m'_{\text{eff}}} = \frac{2}{7}. \tag{2.19}$$

In case that the restitution coefficients are not the same, the appropriate tangential spring stiffness can be calculated from Eq. 2.18. The time step used for the collision dynamics follows from the contact time (not further specified here):

$$\Delta t = \frac{1}{K_N} t_{contact,n} \tag{2.20}$$

where K_N is the number of steps during one contact. Van der Hoef *et al.* [10] report that this value should not be smaller than 5. In the simulations we use a value of $K_N = 10$. In addition to a minimum number of contact steps, also care should be taken with respect to the maximum overlap that can occur. In general, this maximum overlap should be less than 1 % of the particle diameter.

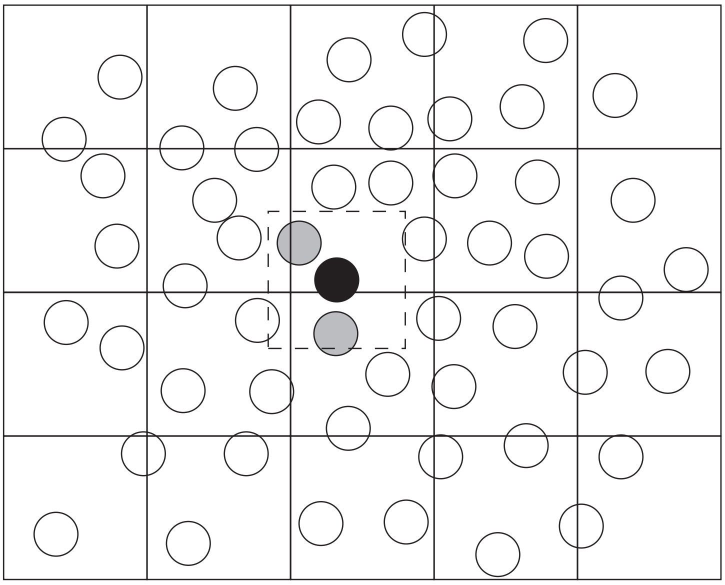

Figure 2.2: *Cell lists and neighbor lists. From the cell lists, a neighbor list is composed for each particle. In the example, the particles that are marked gray are within the area of interest.*

2.2.5 Collision detection

In order to perform simulations for systems containing many particles, it is essential to optimize the computational strategy for the collision detection. To this end, Hoomans *et al.* [5] applied the common cell list and neighbor list method [11] to limit the search area for potential collision partners (see Fig. 2.2).

The simulation box is divided into cells. For each cell, a list is made, containing numbers of the particles that are present in the respective cell. The neighbor list for a particle is constructed by comparing its position with those of the particles contained in the cell lists of the surrounding cells. This strategy strongly limits the computational effort that would be required to search all particles for potential collision partners ($\sim \mathrm{N}^2$ operations). All particles within a specific square (or cube in 3D) are added to the neighbor list, where the size of this area (or volume) depends on the maximum particle radius and the velocities of the particles:

$$R_{nblist} = 2v_{max}\Delta t_{nbl} + 2R_{p,max} \tag{2.21}$$

with v_{max} the maximum instantaneous particle velocity, Δt_{nbl} the time step for neighbor list updates and $R_{p,max}$ the maximum particle radius. The maximum particle velocity is re-evaluated after each time step (DT) that is used for flow-field updates. In this manner, even with changing particle velocities, collisions are still detected correctly.

2.2.6 Particle-wall interactions

The collisions of particles with system walls are in principle similar to those between particles. Differences are that the wall is considered to have an infinite mass and radius. Additionally, if the box is vibrated, the walls also have velocity. Generally, the walls are vibrated using a sinusoidal signal, so that the position and velocity function are described by:

$$r_{z,bottom} = A_z \left(1 + \sin\left(\omega_z t\right)\right) \tag{2.22}$$

$$v_{z,bottom} = A_z \omega_z \cos\left(\omega_z t\right) \tag{2.23}$$

with $r_{z,bottom}$ and $v_{z,bottom}$ the bottom position and velocity, respectively. A_z and f_z are the vibration amplitude [m] and frequency [1/s] in z-direction and $\omega_z = 2\pi f_z$. The dimensionless acceleration (Γ) is defined as:

$$\Gamma = \frac{A_z \omega_z^2}{g_z} \tag{2.24}$$

with g_z the acceleration of gravity, taken to be 9.81 m/s^2. The position and velocity of the walls (Eq. 2.22, 2.23) are updated at the same instant as the particle positions. From the overlap between walls and particles, the contact forces are calculated.

In Chapter 3, we simulate a box where the side walls are covered with particles, in order to study convective motion under vertical vibration. These particles are 'numerically glued' to the side walls, that is, their position and velocity are always fixed relative to the vibrating bottom plate. With respect to collisions, the particles are assumed to have infinite mass, similar to regular walls. Note that with respect to the collision detection, no distinction between 'glued' particles and 'mobile' particles has to be made.

2.2.7 Choosing the collision parameters

In principle, the spring stiffnesses (k_n and k_t) in the soft sphere collision model are related to the physical properties of the particle material, namely the Young modulus and the Poisson ratio. For computational reasons however, the spring stiffness is commonly set to a much lower value, so that the time step used for the integration of the equations of motion of the particles can be kept relatively large; the drawback is that the overlap between the spheres is larger than the deformation that occurs during a collision in the real situation. Therefore, care must always be taken that using a higher spring stiffness will have no significant influence on the phenomena observed.

In order to estimate the restitution coefficient in the normal and tangential direction (e_n and e_t) and the friction coefficient μ, experimental data - obtained from collision experiments - is required. Unless stated otherwise, the coefficient of restitution is set to 0.97 for the normal direction and 0.33 for the tangential direction, and the friction coefficient μ_{pp} is set to 0.1, for all particle-particle interactions. These values have been determined from collision experiments for glass particles with a radius of 750 μm, and were also found to be the most realistic values in a previous simulation study of gas-fluidized beds [6]. It is not *a priori* obvious, however, that the same parameters apply to particles with other radii or consisting of other materials (i.e., bronze-bronze and glass-bronze interactions, see Chapter 4). Therefore, the sensitivity of the results needs to be investigated for such cases.

2.2.8 Governing equations for the gas phase

For the numerical solution of the Navier-Stokes equations we use a finite difference technique as described in Van der Hoef *et al.* [10]. For the gas phase, we divide the domain into computational cells and evaluate the volume-averaged Navier-Stokes equations for each cell to obtain the pressure p and the velocity field $\mathbf{u}$:

$$\frac{\partial\left(\varepsilon\rho_g\right)}{\partial t} + \nabla\cdot\varepsilon\rho_g\mathbf{u} = 0\ , \tag{2.25}$$

$$\frac{\partial\left(\varepsilon\rho_g\mathbf{u}\right)}{\partial t} + \nabla\cdot\varepsilon\rho_g\mathbf{u}\mathbf{u} = -\varepsilon\nabla p - \mathbf{S} - \nabla\cdot\varepsilon\tau + \varepsilon\rho_g\mathbf{g}\ , \tag{2.26}$$

where ε is the volume fraction [-] and ρ_g is the density [kg/m^3] of the gas phase, which is directly linked tot the pressure p via the equation of state of an ideal gas:

$$\rho_g = \frac{pM_g}{RT} \tag{2.27}$$

with M_g the molecular mass of the gas, R the universal gas constant (8.314 J/(mol.K)) and T the temperature [K]. For the viscous stress tensor τ [N/m^2], we use the general form for a Newtonian fluid [3]:

$$\tau = -\left(\lambda_g - \frac{2}{3}\mu_g\right)(\nabla\cdot\mathbf{u})\,\mathbf{I} - \mu_g\left(\nabla\mathbf{u} + \left(\nabla\mathbf{u}^T\right)\right) \tag{2.28}$$

with λ_g the gas phase bulk viscosity, μ_g the gas phase shear viscosity, and $\mathbf{I}$ the unit tensor. In the simulations, the bulk viscosity of the gas phase is set equal to zero, which is allowed for gases [3].

The term $\mathbf{S}$ in Eq. 2.26 represents the effective momentum exchange with the solids phase, which can formally be written as

$$\mathbf{S} = \frac{1}{V_{cell}}\int\sum_{i=1}^{N_{part}}\mathbf{F}_{i,d}\,\delta\left(\mathbf{r}-\mathbf{r}_i\right)\,dV\ , \tag{2.29}$$

where the integral is over the volume of a computational cell, the summation is over all particles in the cell, and the drag force $\mathbf{F}_{i,d}$ is identical to what is used in the equation of motion for the solid phase. In the numerical implementation, this force-per-volume term $\mathbf{S}$ is distributed to the eight nearest grid points (nearest four when considering a 2D system) using a volume-weighing technique.

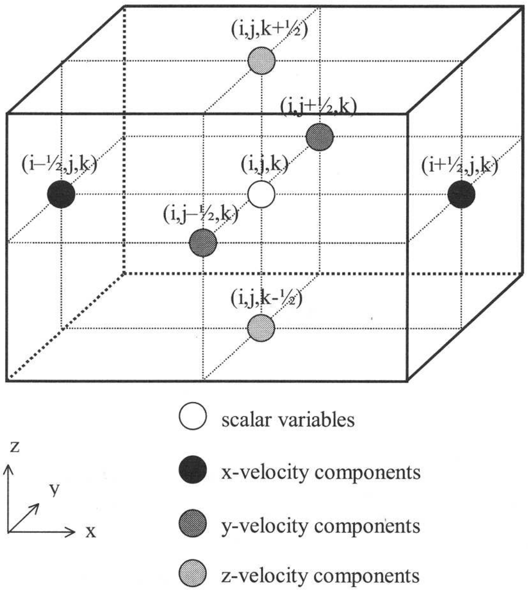

Figure 2.3: *Centering of the Eulerian variables. The scalar variables such as porosity and pressure are defined at cell center. The velocity components are found half a cell staggered, on the respective cell faces. (Figure taken from [9]).*

The numerical solution procedure follows the lines of Van der Hoef *et al.* [10]. A finite difference technique, employing a staggered grid to ensure numerical stability, is used to solve the gas-phase conservation equations. The scalar variables (p and ε) are defined at the cell center, whereas the velocity components are defined at the cell faces (see Fig. 2.3). A pressure correction technique is employed to solve the discretized sets of partial differential equations. More information can be found in Van der Hoef *et al.* [10]. Boundary conditions are taken into account by utilizing the flag matrix concept, which allows for the use of different boundary conditions for different cells.

2.3 Implementation of vibration

2.3.1 Principle

The basic numerical model described in the previous paragraphs can be readily used for the modeling of gas-fluidization or the study of impact phenomena (Chapter 6 and 7). In order to study the behavior of granular media under vibration, however, the effect of moving boundaries must be incorporated in the gas phase equations to properly account for the force (change in momentum) that is enacted upon the continuum by the accelerating and decelerating walls. There are different modeling options for incorporating these effects, but they can be traced back to two general forms that differ with respect to the way in which the computational cells - which are used to evaluate the Navier-Stokes equations - are implemented. In the first approach the Navier-Stokes equations must be transformed so that the grid of computational cells remains fixed to the moving box and that they are accelerating and decelerating with respect to the laboratory frame. In the second approach, the computational grid remains fixed to the laboratory framework and the vibrated box moves through the computational domain. Along the lines of this second approach, Tatemoto *et al.* [7] use a technique where all computational cells are fixed to the laboratory frame. The vibration is included by changing the size of the lowest row of computational cells according to the position of the bottom plate.

In this work, we follow the second approach, that is, we keep the computational grid fixed to the laboratory frame. In contrast to Tatemoto *et al.*, we do not change the size of the computational cells. This means that the lowest computational cells will in general be ‘cut’ by the bottom plate, so that they are only partially located in the vibrated box. When the amplitude of the vibration is larger than the size of the cells, computational cells will even find themselves completely outside the vibrated box when the bottom plate is at its highest position, and hence should be taken out of the update procedure. We have adjusted the model to incorporate these cell changes, which we describe in detail in the following section. We start the discussion with the incorporation of the moving walls into the computational grid. Next, the consequences for the convective mass and momentum fluxes and for the frictional stress are discussed. Then, the boundary conditions, the gas-solid coupling and handling of cell changes are treated, followed by a discussion of the interaction between particles and moving boundaries. Finally, the general calculation conditions will be addressed. The gas-solid coupling, numerical verification of the model and the computational flow chart can be found in Appendices A, B and C, respectively.

2.3.2 Cartesian and staggered cells

For the numerical solution of the Navier-Stokes equations we use a finite difference technique as described in Van der Hoef *et al.* [10]. To this end, the computational domain is divided into computational cells. The mass balance (Eq. 2.25) is evaluated on a regular rectangular (Cartesian) grid, while the momentum balance (Eq. 2.26) is calculated on a grid that is half a cell staggered with respect to the Cartesian grid, which enhances numerical stability. Since there are 3 directions, there are also 3 types of staggered cells.

We now focus on the calculation of the void fraction (ε) in case the cell is cut by a moving wall. Since the position of the moving wall is known at any time, it is straightforward to evaluate ε:

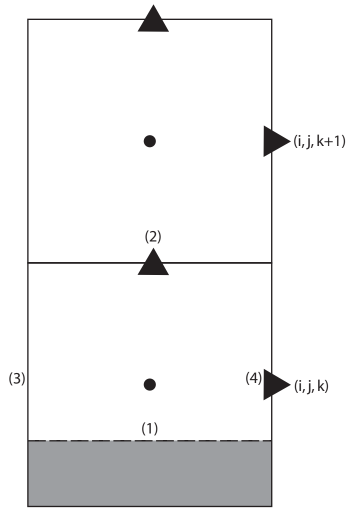

Figure 2.4: *The effect of walls on mass fluxes. Schematic representation of the Cartesian cells (solid lines). We consider a bottom wall (bold dashed line) moving through the cells. As the bottom wall proceeds through the cell, the area available for mass transport through the horizontal cell faces (indicated '1' and '2') is not reduced. The use of* ε_{em} *(Eq. 2.33) is required. For the vertical cell faces (indicated '3' and '4'), however, the area is reduced and* ε *does not need to be corrected.*

$$\varepsilon = 1 - \frac{V_{wall} + V_{particles}}{V_{cell}} \tag{2.30}$$

where V_{cell}, V_{wall} and $V_{particles}$ are the volume of the cell, the volume occupied by the bottom or top wall and by the particles present in the cell, respectively. Both V_{wall} and $V_{particles}$ are readily calculated from the position of the moving wall and the particles.

The movement of the wall increases/decreases the volume available for the gas in the Cartesian cells, generating the wall-induced gas flow in a natural way (see Fig. 2.4). Special care must be taken when analyzing the (staggered) momentum cells, on which is elaborated in the next section. Note that for the calculation of the drag force on a particle, the local void fraction around the particle is required, which can be very different from ε as given by Eq. 2.30; a much better approximation is given by the void fraction of the *emulsion* (ε_{em}), that is, the void fraction of *only* the gas and particle mixture, located above the moving wall:

$$\varepsilon_{em} = 1 - \frac{V_{particles}}{V_{cell} - V_{wall}} \tag{2.31}$$

These void fractions are also used in some of the expressions for the mass flux in z-direction (see Fig. 2.4).

From an implementation point of view, it is convenient to introduce ε_{wall}, which is the void fraction of the computational cell when *only* the wall would be present:

$$\varepsilon_{wall} = \frac{V_{cell} - V_{wall}}{V_{cell}} \tag{2.32}$$

The void fraction of the emulsion (ε_{em}) in a Cartesian cell (partially) occupied by a wall can then be written as:

$$\varepsilon_{em} = \frac{\varepsilon}{\varepsilon_{wall}} \tag{2.33}$$

While for regular cells, the void fraction in a staggered cell is calculated simply by averaging the two nearest void fractions in the Cartesian grid, this method cannot be applied when one of these is affected by the presence of a wall. A similar correction as for the Cartesian cell can be applied, while taking the location of the moving wall into account.

2.3.3 Convective fluxes and stress

In this section we consider the expressions for the different mass and momentum fluxes in the three-dimensional system. Per computational cell, a total of 12 fluxes are calculated: 3 mass fluxes (3 directions) and 9 momentum fluxes (for each component 3 directions). The system is conservative so that the outgoing flux for one cell is the same as the incoming flux for the neighbor cell. Consider the expression for the mass flux ($\varepsilon\rho_g\mathbf{u}$) and see Fig. 2.4 in the previous paragraph. When a wall enters the Cartesian cell, ε will become smaller, and as a result the mass flux ($\varepsilon\rho_g\mathbf{u}$) is reduced.

This is correct for the transport through the side walls (x- and y-direction: $\varepsilon\rho_g u_x$, $\varepsilon\rho_g u_y$) of the cell, where indeed the available area for mass transport is reduced by the same factor that ε was reduced with. However, as can be seen in Fig. 2.4, the horizontal cell faces (transport in z-direction: $\varepsilon\rho_g u_z$) remain entirely available for mass transport so that for this direction the mass flux should not be reduced. The most straightforward way to remove the undue effect of the wall for the horizontal cell faces, is by using ε_{em} for the mass flux in the vertical direction. Additionally, as in regular cells without a wall being present, the presence of particles also reduces the area of transport, but this is accounted for in this expression for ε_{em} (Eq. 2.33). A similar analysis can be applied to the 9 momentum fluxes ($\nabla \cdot \varepsilon\rho_g\mathbf{uu}$), see Fig. 2.5. When we consider the transport of the 3 velocity components in the vertical direction (i.e., through the horizontal cell faces), again, if a wall is present in the staggered cell under consideration, the effect of the wall in the expression for this vertical flux needs to be removed, that is, the porosity needs to be adapted in the expression. In analogy to the mass fluxes, the momentum fluxes through the vertical cell faces (x- and y-direction) do not need to be corrected, since the presence of the wall again limits the area available for momentum transport. The stresses are handled in a similar manner.

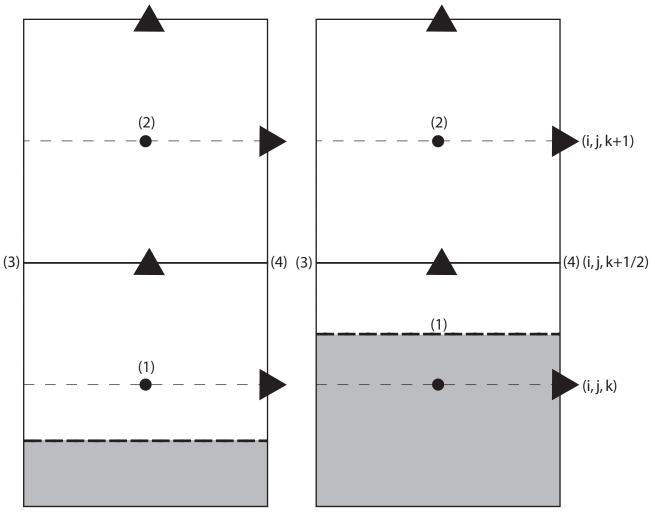

Figure 2.5: *The effect of walls on the momentum fluxes. Schematic representation of the Cartesian cells (solid lines) with the staggered cells for the z-direction indicated by the unbroken dashed lines (staggered cell center at (i,j,k+$\frac{1}{2}$)). We consider a bottom wall (bold dashed line) moving through the computational cells. As can be seen, different situations occur. (i) On the left-hand side, the bottom wall is located in the Cartesian cell, but not in the staggered cell for z-momentum: the horizontal cell faces (indicated '1' and '2') of the staggered cell are fully available for momentum transport. Also the vertical cell faces ('3' and '4') are fully available. (ii) On the right-hand side, the bottom wall is located in the both the Cartesian and the staggered cell. The upper horizontal cell face ('2') of the staggered is still fully available for momentum transport. However - in the absence of gas inflow - no gas is flowing through the lower horizontal cell face ('1'). Additionally, the vertical cell faces ('3' and '4') are partially blocked and the area available for momentum transport in those directions is reduced.*

2.3.4 Cell changes and boundary conditions

When the boundary is moving through the computational domain, it can occur that computational cells have to be removed or added. This means that the location of the boundary cells is not fixed and the flag matrix, which describes the type of computational cell, is updated accordingly. We will start our discussion with the removal of cells. At the time that a computational cell has been completely emptied, the respective cell becomes a boundary cell. However, care must be taken that the mass and momentum balances are correctly satisfied, i.e., that no mass or momentum is lost. With respect to the mass balances, the mass is conserved when the computational cell is removed by depositing the remaining amount in the nearest cell in direction of vibration. With respect to the momentum balances, the remaining x- and y-momentum is conserved in a similar manner: the momentum is deposited in the nearest staggered cell of the respective type of momentum in the direction of vibration. The remaining z-momentum is conserved automat-

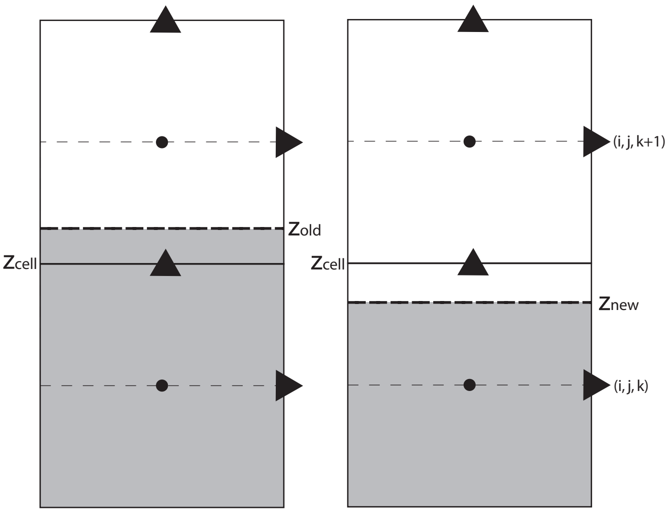

Figure 2.6: *Computational grid before and after a Cartesian cell is added. Since usually the Cartesian cell is added in between time steps (DT), the mass flux into the newly added cells is fractionated. The incoming mass flux that can be attributed to the new cell is:* $J'_{dt} = J'_{DT} \cdot \frac{z_{new}-z_{cell}}{z_{new}-z_{old}}$ *with* z_{new} *and* z_{old} *the new and old bottom plate position, respectively and* z_{cell} *the boundary of the cell. The same correction is also used for the outgoing mass flux of the cell above, since we have a conservative system.*

ically since the part of the staggered cell that remains after removal is not solved anymore. Since these measures describe phenomena at a time level below the update of the flow field, one could call this a sub time-scale correction.

See Fig. 2.6, where the lower half of the Cartesian cell is the subject of the discussion below. When cells are added, similarly a sub-time scale correction is made to the convective mass and momentum fluxes. This is necessary since the influx of mass and momentum into the newly added cell is not for the duration of the entire time step and is therefore fractioned as depicted in Fig. 2.6.

A remaining point is how to choose the initial values for the newly added Cartesian cells. More specifically, we need to choose an initial pressure and initial values for the gas velocity. The initial pressure is calculated from the pressure of the nearest Cartesian cell in the direction of vibration, also taking into account the pressure gradient. This is exemplified for the case when adding a Cartesian cell at the bottom of the domain (obtaining information from the cell above, see Fig. 2.6):

$$p_{i,j,k} = p_{i,j,k+1} - \frac{dp}{dz}_{i,j,k+1/2} \cdot \mathrm{DZ} \tag{2.34}$$

with $p_{i,j,k}$ and $p_{i,j,k+1}$ the pressure in the newly added cell and the cell above, respectively. $\left(\frac{dp}{dz}_{i,j,k+1/2}\right)$ indicates the pressure gradient of the cell above. The initial values for the gas velocity are taken the same as those of the cell above.

Also, the velocity boundary conditions of the vibrated box require attention. For the side walls of the vibrated box, only tangential velocity components are important (i.e., the side walls do not induce a gas flow normal to the wall surface, such as the bottom and top walls do). Therefore, only the boundary conditions for the no-slip case (flag 3) need to be adjusted. The vertical velocity in the boundary must be chosen such, that the velocity at the surface of the boundary corresponds to the vertical velocity of the box. In the following equation, an example is shown for the left side wall, where the indices (i,j,k+1/2) indicate the boundary cell:

$$u_{z,i,j,k+1/2} = 2 \cdot v_{z,bottom} - u_{z,i+1,j,k+1/2} \tag{2.35}$$

with u_z the velocities in the different flow cells - indicated by the indices - and $v_{z,bottom}$ the vertical velocity of the box.

In Fig. 2.7 we show the boundary condition in the cells containing moving walls. In principle, the velocity at the boundary can also be obtained from the normal velocity of the wall (i.e., vibration velocity). However, instabilities can occur when the moving wall approaches the upper boundary, which is exemplified below. By rewriting the following equation, the velocity at the lower boundary ($u_{z,i,j,k+1/2}$) can be obtained:

$$v_{z,bottom} = \frac{(\Delta z - \delta z) \cdot u_{z,i,j,k+1/2} + \delta z \cdot u_{z,i,j,k+3/2}}{\Delta z} \tag{2.36}$$

The instability occurs when the plate is very close to the top side of the computational cell. Even if the velocity of the cell ($u_{z,i,j,k+3/2}$) deviates only slightly from the box velocity, the linearly extrapolated velocity at the lower boundary ($u_{z,i,j,k+1/2}$) can become very large. Instead, we perform a linear extrapolation on the velocity at the boundary from the gas velocity field:

$$u_{z,i,j,k+1/2} = 2 \cdot u_{z,i,j,k+3/2} - u_{z,i,j,k+5/2} \tag{2.37}$$

Note that the procedure described above is specifically for a closed box (flag 2). However, when applying gas-fluidization *in addition* to the vibrations, we use influx (flag 4) and prescribed pressure cells (flag 5) for the lower and upper boundary condition, respectively. The influx cells are still moving through the computational domain, as before. The prescribed pressure cells at the top of the computational domain remain in place. Sometimes, it is desirable to evaluate the effects of shaking where the fluid is not forced through the domain. For such cases prescribed pressure cells (flag 5) are used for both the upper and lower boundary. In a real experiment, this situation would correspond to an upper and lower boundary being made of a (metal) gauze, with a negligible pressure drop, so that gas is free to move in and out of the system.

We conclude this section with a few comments on the calculation conditions. In most simulations we use free slip boundary conditions for all the system walls, which implies that no gas can enter or leave the system and thus the total amount of gas is conserved.

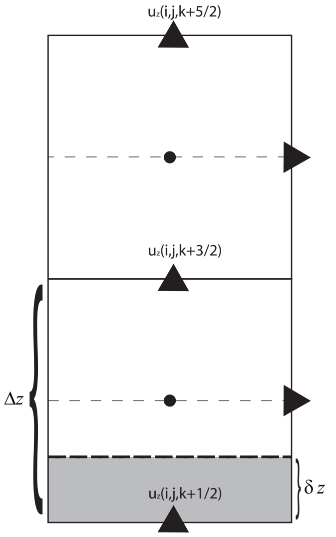

Figure 2.7: *Velocity boundary conditions for the normal velocity component in a cell containing moving boundaries. The velocity at the boundary of the Cartesian cell is linearly extrapolated from the velocity field in the cells above.*

In the numerical scheme, conservation of mass is ensured by means of an iterative scheme, where in each step of the iteration, for each cell i, j, k the ratio of mass defect $\mathrm{def}_{i,j,k}$ [kg/m^3] and the gas density $(\varepsilon\rho_g)_{i,j,k}$ is evaluated. Convergence is achieved - and thus the flow field is accepted - when:

$$\frac{\mathrm{def}_{i,j,k}}{(\varepsilon\rho_g)_{i,j,k}} < \epsilon \tag{2.38}$$

with ϵ the accuracy of the pressure iteration, for which usually a value of 10^{-9} is used. For cells that are nearly emptied (porosity smaller than 10^{-3}) due to the moving boundary, we use a value of 10^{-6}. In this way, the absolute accuracy is kept in the same order of magnitude.

After an iteration has been carried out, a new velocity field can be calculated. When the number of iterations becomes too large (i.e., 25), relaxation is applied to the newly calculated velocities until the solution has been obtained.

2.4 The immersed boundary method

In the Immersed Boundary method the gas phase is fully resolved, i.e., the gas phase is solved on a length scale that is much smaller than the size of the particles. The method is therefore well suited for the description of the intruder as used in Chapter 7, since the intruder is much larger than the grid size used in these simulations. In this section we will discuss the theory behind the Immersed Boundary method, as proposed by Uhlmann [13] and Van der Hoef *et al.* [10].

In order to calculate the interaction between the continuum phase and the immersed object, Lagrangian force points need to be defined and uniformly distributed on the objects' surface. The velocity $\mathbf{W}_m$ at these force points is known and can be computed from the combined effect of particle translation and rotation, which, in the case of a sphere is defined as:

$$\mathbf{W}_m = \mathbf{v}_i + (\omega_i \times (\mathbf{r}_m - \mathbf{r}_i)) \tag{2.39}$$

with $\mathbf{v}_i$ the particle translation velocity, ω_i the rotational velocity, $\mathbf{r_m}$ the position of the Lagrangian force point m and $\mathbf{r_i}$ the position of the sphere center.

The force density at the location of the Lagrangian force point is then calculated from a no-slip boundary condition: at the force point, the local gas velocity $\mathbf{u}^*$ should match the local particle velocity:

$$\mathbf{F}_m = \frac{(\varepsilon\rho_g)_{new}\mathbf{W}_m - (\varepsilon\rho_g)_{old}\mathbf{u}^*}{\Delta t} \tag{2.40}$$

$\mathbf{u}^*$ is obtained by using a suitable distribution function D. We use a volume-weighing technique where the local properties are obtained from the eight surrounding data points. However, using this kind of distribution function, force oscillations can occur since a force point may suddenly use different data points due to movement. For the cases that we studied though, this effect was small, as will be demonstrated in Chapter 7. More smooth distribution functions - such as regularized delta functions introduced by Peskin [12] - can be used to alleviate these problems. Note that due to the staggered nature of the momentum equation, the mapping should be carried out separately for each component.

The Eulerian force density $\mathbf{F}^*_m$ is obtained by scaling the Lagrangian force density $\mathbf{F}_m$, which, for a sphere is done using the equation:

$$\mathbf{F}^*_m = \frac{\Delta v_m}{h^3}\mathbf{F}_m = \frac{\pi}{3N_p}\left(12\left(\frac{R}{h}\right)^2 + 1\right)\mathbf{F}_m \tag{2.41}$$

with $h = \sqrt[3]{\Delta x \Delta y \Delta z}$ the characteristic Eulerian grid size, R the particle radius and Δv_m the volume of the range of influence of a force point. N_p is the total number of Lagrangian force points positioned on the sphere surface.

Finally, the force density at the location of the Eulerian grid can be obtained by mapping the Lagrangian force density back, using the same distribution function D. Again, this mapping needs to be carried out for each component of the force density separately and needs to be summed over all Lagrangian force points that are located within the range of influence of the Eulerian grid point.

We now have obtained momentum source terms, which need to be introduced in the momentum equation (Eq. 2.26). These terms are introduced in the explicit part of the momentum equation.

For more details on the verification and use of this method, the reader is referred to Chapter 7.

Appendix A: Vibration and two-way coupling

The two-way coupling between the particles and the gas phase is handled via the source term $\mathbf{S}$ (Eq. 2.29), which can also be written as:

$$\mathbf{S} = \frac{1}{V} \int \sum_{a=0}^{N_{part}} \frac{\mathrm{V_i}\beta}{(1-\varepsilon)} (\mathbf{u} - \mathbf{v}_i)\, \delta\, (\mathbf{r} - \mathbf{r}_i)\, \mathrm{d}V \tag{2.42}$$

with $\mathrm{V_i}$ the volume of a particle [m^3], β the interphase momentum transfer coefficient [kg/(m^{3}s)] and $\mathbf{u}$, $\mathbf{v}_i$ and ε the local gas velocity, particle velocity and porosity.

The information is mapped to the centers of the computational cells via a volume weighing method. Regular calculation for z-momentum goes via:

$$\beta_{i,j,k+\frac{1}{2}} = 0.5\, (\beta_{i,j,k} + \beta_{i,j,k+1})\,. \tag{2.43}$$

However, in the case of vibrations, part of a computational cell may be occupied by the system wall. In that case, the mapping must be adjusted, since the amount of gas with which the particles are exchanging momentum is different in case a flow cell is partially occupied by the wall. We first consider such case on the left-hand side in Fig. 2.8, where $\beta_{stag,i,j,k+\frac{1}{2}}$ is located at the cell interphase. The amount of

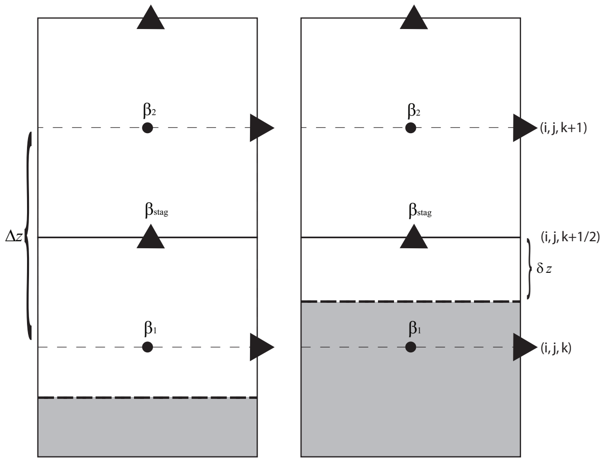

Figure 2.8: *The effect of walls on the two-way coupling. Schematic representation of the Cartesian cells (unbroken black lines) with the staggered cells for the z-direction indicated by the broken gray lines. We consider a bottom wall (broken black line) moving through the computational cells. As can be seen, different situations occur. (i) On the left-hand side, the bottom wall is be located in the Cartesian cell, but not the staggered cell for z-momentum. The momentum in the staggered cell is calculated using Eq. 2.44. (ii) On the right-hand side, the bottom wall is located in the both the Cartesian and the staggered cell and Eq. 2.45 is used*

momentum in this staggered cell can be calculated via:

$$\beta_{i,j,k+\frac{1}{2}} = 0.5 \left(\frac{\beta_1}{\varepsilon_{wall}} + \beta_2 \right) \tag{2.44}$$

where β_1 and β_2 are the amount of momentum that was mapped in the regular manner to the Cartesian cell centers. ε_{wall} is used to re-scale the momentum to the volume of a Cartesian cell and is calculated via Eq. 2.32.

A second situation that can occur (see right-hand side Fig. 2.8) is that the wall is present in the staggered cell for z-momentum. In that case, instead of mapping to the cell center of cell 1, we map to the position of the plate (obtaining quantity $\beta_1^{'}$). After this the amount is adjusted via:

$$\beta_1 = \frac{1}{\varepsilon_{stagg,wall}} \cdot \frac{\delta z}{0.5\Delta z} \cdot \beta_1^{'} \tag{2.45}$$

with $\varepsilon_{stagg,wall}$ the porosity in the staggered cell if only the wall would be mapped (analogous to Eq. 2.32).

To calculate $\beta_{i,j,k+\frac{1}{2}}$, we find that:

$$\beta_{i,j,k+\frac{1}{2}} = \beta_1 + 0.5\beta_2 \tag{2.46}$$

We have tested the implementation by measuring the pressure drop of a fixed particle bed where gas is passed through and where the bottom plate was located at different heights in the Cartesian cell. In all cases we found the pressure drop that would be obtained using the Ergun equation. See Appendix B.

Appendix B: Numerical verification

Results for the verification of the moving boundaries implementation can be found in this Appendix. Cases for which the analytical/physical results are known, were tested. For our simulations, we commonly use a 2D gas system, which is justified if the particle bed has a limited depth. The implementation, however, was tested for both the 2D as well as the 3D system. We considered four test systems: (i) empty vibrated bed (closed box), (ii) empty vibrated bed (open on both sides), (iii) empty gas-fluidized vibrated bed and (iv) a packed bed.

For the (empty) vibrated beds and the gas-fluidized vibrated bed, we verified the generated gas velocity profiles and the pressure gradients. For the packed bed, we verified the pressure drop.

Before this, we first tested the conservation of mass in the closed boxes. Two cases were considered that differ in the number of cell changes that occur during vibration. In case 1 many cell changes occur, while during case 2 none take place. We found that mass conservation was very good indeed (case 1: 10^{-9} % over 7 s and case 2: 10^{-8} % over 45 s). Other tests were conducted with respect to the soft sphere collision model. The collision dynamics were verified against the results of the hard sphere model and were found to correspond well (results not shown here). Interestingly, differences between the two models can occur due to the possibility that the collision type (with respect to rotations) can change from ‘sliding’ to ‘sticking’ (and back) in the soft sphere model as the collision progresses. This is due to the changing ratio between normal and tangential force (see Eqns. 2.4 and 2.5), while for the hard sphere model the collision type is fixed at the instant of collision. As a result, differences in rotational/translational velocities may be found.

2.4.1 Empty column: vibration and gas-fluidization

For the investigated vibration cases, we evaluate the Navier-Stokes equations in 2D in a column consisting of 25 cells in both the x- as well as the z-direction. The physical dimensions are $8.25.10^{-3} \times 6.5.10^{-4} \times 8.25.10^{-3}$ m^3. Free slip boundary conditions (flag 2) are used for the system walls. We investigated air at 3 different pressures (0.01, 1.0 and 100 atmosphere) with a viscosity of $1.8.10^{-5}$ Pa.s. Additionally, at atmospheric pressure a larger viscosity ($1.8.10^{-3}$ Pa.s) was investigated. The time step (DT) for the flow field update was $2.5.10^{-5}$ s, except for the case of 0.01 atmosphere and the case with the increased viscosity at atmospheric pressure, in which case a time step $\mathrm{DT} = 5.0.10^{-6}$ s was used for stability. In all cases, we applied a vibration amplitude of $9.0.10^{-4}$ m and frequency of 55 Hz. The size of the computational cells is $3.3.10^{-4} \times 6.5.10^{-4} \times 4.0.10^{-4}$ m^3. Since we used a gravitational constant g_z of -9.81 m/s, we calculate $dp/dz = \rho_g g_z$ to be -11.75 Pa/m. In other words, for every ‘g_z’ of acceleration acting on the gas, a pressure gradient of -11.75 Pa/m is generated in the gas. Only the results for the atmospheric cases are shown, the results for the other cases are similar.

As can be seen in Fig. 2.9 and Fig. 2.10, the results for both the gas velocity (Eq. 2.23) as well as the pressure gradient, agree well with the analytical results. The

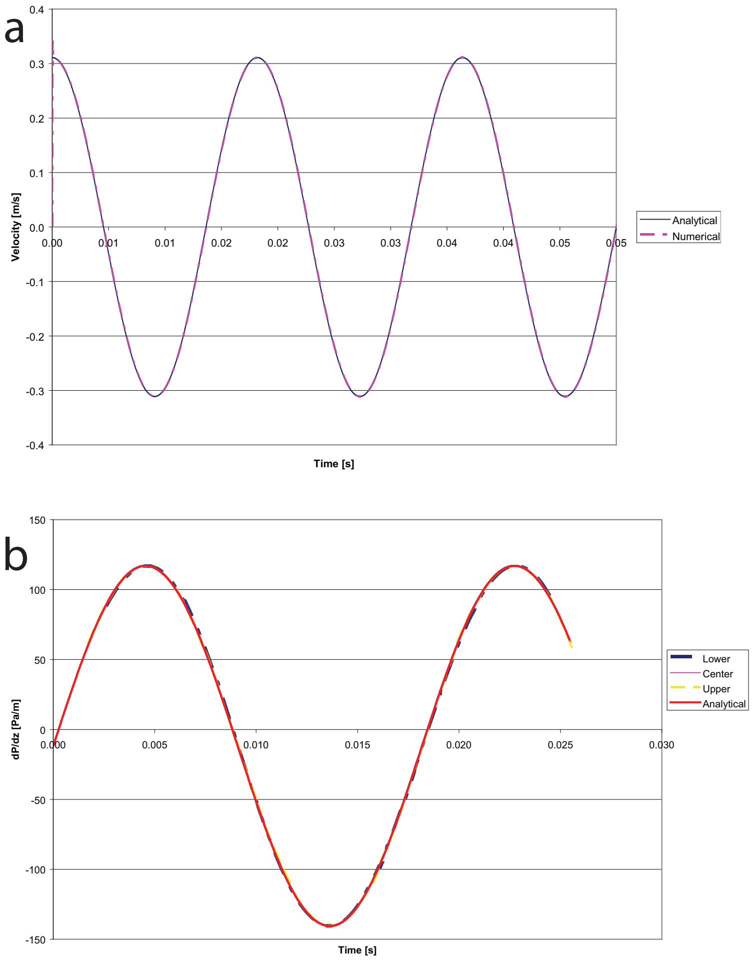

Figure 2.9: *The vibration induced oscillation of vertical gas velocity* (u_z) *and vertical pressure gradient* (dP/dz) *for a closed, vibrated box. In Fig. 2.9a, the analytical solution and the induced gas velocity are presented. In Fig. 2.10a, the percentage correct velocity vectors is shown, where the velocity vectors were marked as being correct if the velocity difference is smaller than 2 % of the analytical value. The dips occurring around* $u_z = 0.0$ *m/s are due to the selection criterium, where the relative error goes to infinity as* u_z *approaches 0.0 m/s (i.e., at maximum amplitude). In Fig. 2.9b, the vertical pressure gradient of the lower, center and upper cells are shown, where the lower and upper cells are 'cut' by the bottom and top wall, respectively. Additionally, the analytical solution is provided. In Fig. 2.10b, the percentage of correct pressure gradients is shown. Similar to the velocity, dips occur around* $dP/dz = 0.0$ *Pa/m (bottom goes through equilibrium position) for similar reasons.*

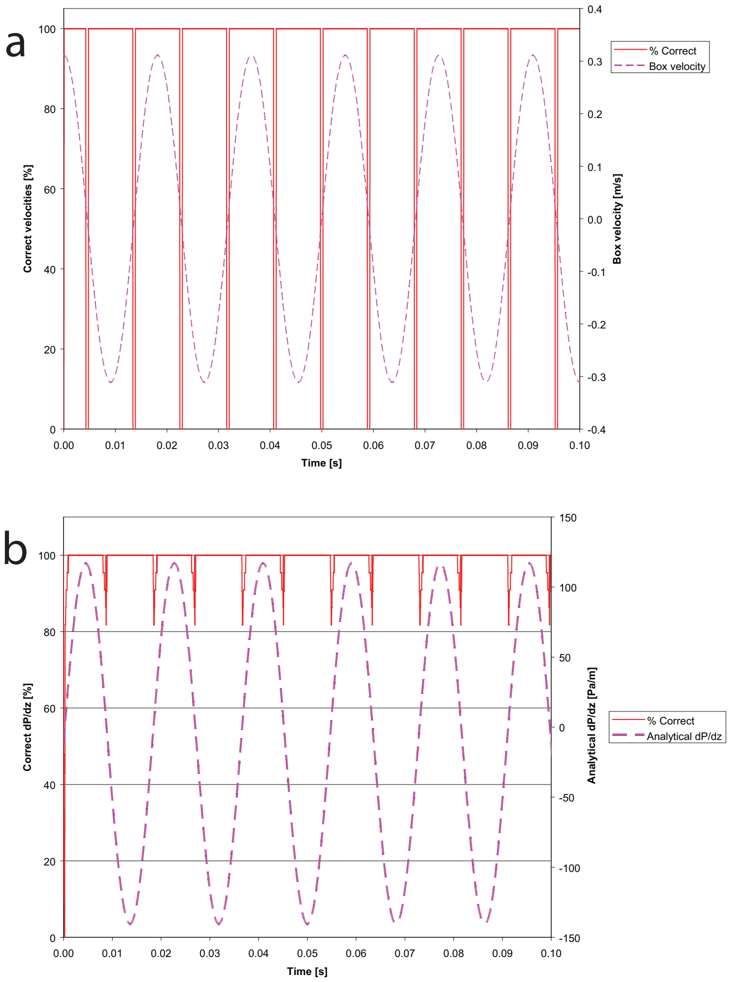

Figure 2.10: *Correct vertical gas velocities* (u_z) *and vertical pressure gradient* (dP/dz) *in time.*

dimensionless acceleration (Γ, which gives the maximum acceleration normalized with gravity) of the plate at the chosen vibration conditions is 10.95. Therefore, in the presence of gravity, the pressure gradient in the box will be between -140.5 and 117.0 Pa/m, as is confirmed by Fig. 2.9b.

For the case with gas-fluidization and simultaneous vibration we use the same column setup as mentioned above, except that the bottom and top cells have different boundary conditions (influx and prescribed pressure). The superficial gas velocity (u_{bg}) is 0.20 m/s. Theoretically, the gas velocity in the laboratory frame should be (see Eq. 2.23):

$$u_z = A_z \omega_z \cos(\omega_z t) + u_{bg} \tag{2.47}$$

with $\omega_z = 2\pi f_z$. See Fig. 2.11.

Comparing Fig. 2.9b and Fig. 2.11b, the form of the pressure gradient is the same as in the case without gas-fluidization. This is as expected since we have a constant gas influx with no accelerations in addition to those induced by the walls and gravity. Furthermore, super-imposed on the vibration velocity, one indeed finds the applied superficial gas velocity u_{bg}.

We also checked the effect when both the upper and lower walls have prescribed pressure boundary conditions (i.e., the walls are 'open'). For this test, the gravity acceleration needs to be set to 0.0 m/s^2 (or the gas would continue to accelerate due to the lack of a bottom). We did not find that any velocity or pressure gradients were developed during the vibration (not shown here), as was to be expected.

2.4.2 Granular bed pressure drop

To verify the effect of boundary penetration on the two-way coupling between gas and particles, the pressure gradients were verified with the Ergun equation (Eq. 2.12). The bed consists of $8 \times 1 \times 25$ cells and the bed dimensions are $0.064 \times 0.004 \times 0.2$ m^3. The used particles have a diameter of 1 mm. As a result, in our computational cells (dimensions $8.0.10^{-3} \times 4.0.10^{-3} \times 8.0.10^{-3}$ m^3), $8 \times 4 \times 8$ particles are stacked in the x-, y- and z-direction, respectively. This leads to an uniform porosity 0.476. The number of particles is 24576, so that a total bed height of 12 completely filled computational cells is obtained. The particles are ordered according to a cubic structure. We use a superficial gas velocity of 1.0 m/s and accordingly, a pressure gradient dP/dz of -16800 Pa/m should be found (Ergun equation). In table 2.1, it can be seen that the pressure gradient corresponds well with the value that was obtained from the Ergun equation.

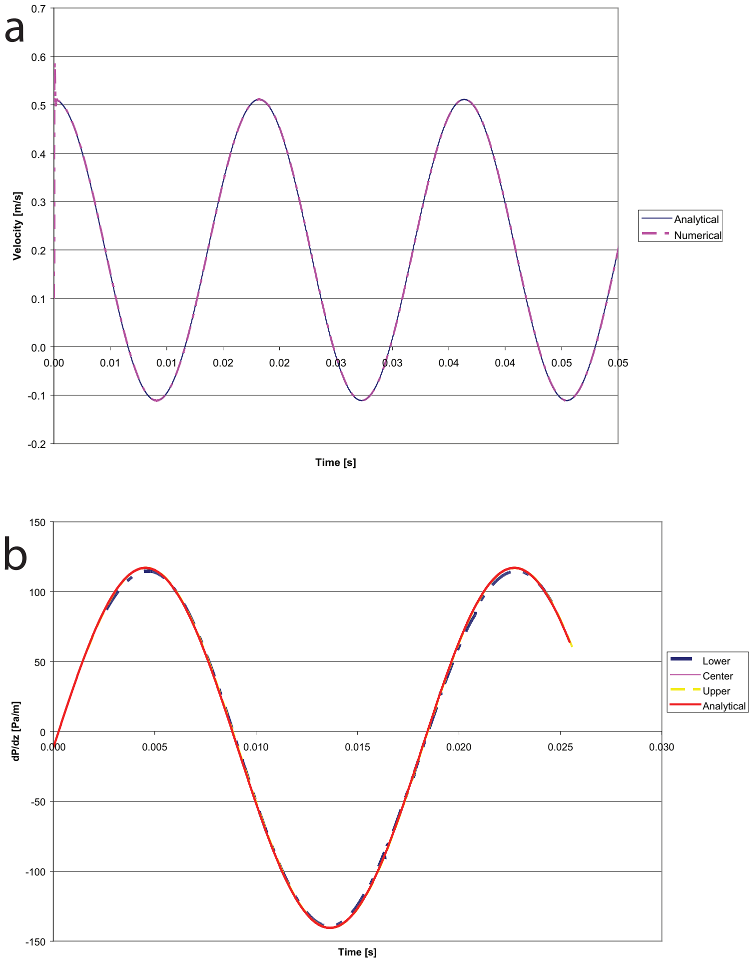

Figure 2.11: *The vibration induced oscillation of vertical gas velocity* (u_z) *and vertical pressure gradient* (dP/dz) *for a vibrated box with simultaneous gas-fluidization. In Fig. 2.11a, we show the wall velocity plus superficial gas velocity* (u_{bg}) *and the induced gas velocity* (u_z)*. In Fig. 2.12a, the percentage correct velocity vectors is shown. The velocity vectors were marked as being correct if the velocity difference is smaller than 2 % of the analytical value. Again, dips occurring around* $u_z = 0.0$ *m/s. Note that these dips occur when* $u_z = 0.0$ *(Eq. 2.47). In Fig. 2.11b, the vertical pressure gradient of the lower, center and upper cells are shown. Small deviations from the analytical solution can be observed, which are caused by the removal of Cartesian cells at that particular time. The analytical solution is also shown. In Fig. 2.12b, the percentage of correct pressure gradients is shown. Similar to the velocity, dips occur around* $dP/dz = 0.0$ *Pa/m (bottom goes through equilibrium position) for similar reasons.*

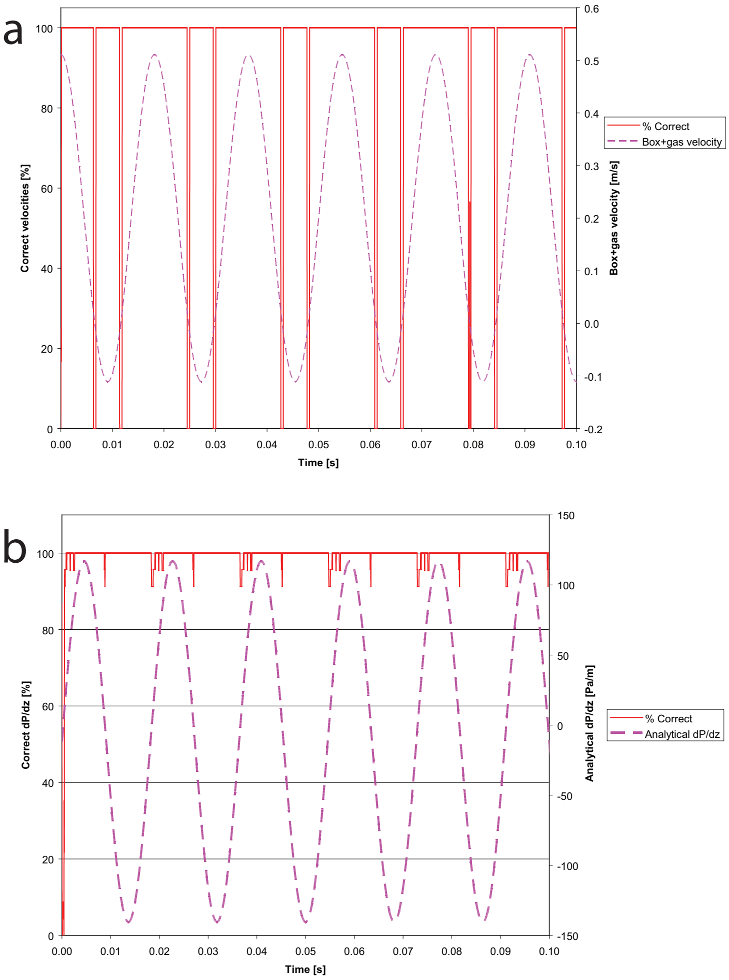

Figure 2.12: *Correct vertical gas velocities* (u_z) *and vertical pressure gradient* (dP/dz) *in time.*

Cell	0 %	12.5 %	25.0 %	37.5 %	50.0 %	62.5 %	75.0 %	87.5 %
1	-16771	-16769	-16768	-16767	-16765	-16763	-16760	-16756
2	-16782	-16780	-16779	-16777	-16775	-16773	-16770	-16766
3	-16804	-16802	-16801	-16799	-16797	-16795	-16792	-16788
4	-16826	-16825	-16823	-16821	-16819	-16817	-16814	-16810

Table 2.1: *Pressure gradient in vertical direction for the lower 4 cells. The percentages indicate the position of the plate, i.e., 75 % means that 75 % of the lowest Cartesian cell is occupied by the bottom wall.*

Appendix C: Computational flow chart

In the schematic of Fig. 2.13, the computational flow chart can be found.

```
Initialise
Output Manager
while ($t < T_{stop}$)
  DEM
  t=t+DT
  Flagmatrix
  Wall In Cell
  Update Walls
  Setup Cell List
  Lagrange to Staggered
  Flowsolve
  Output Manager
End
```

Figure 2.13: *Computational flow chart of Discrete Particle Model, with vibrations included.*

In 'Initialise', the input variables are read from file. In 'Output Manager', relevant data is saved in files. After this, a loop is entered, where in 'DEM' the collisions are performed. In 'Flag Matrix' the flag matrix - which may be different from the previous time level due to the moving walls - is determined. In 'Wall In Cell', the cell void fraction (ε) is adjusted for the presence of walls (Eq. 2.30). In 'Update Walls', the measures needed when adding/removing cells are performed if walls have changed from one Cartesian cell to another during the last time step. In 'Setup Cell List', particle numbers are attributed to the Cartesian cell in which their center of mass is located, so that 'Lagrange to Staggered' can be used to account for the particle volumes in ε, (see Eq. 2.30). After this, new gas velocities and pressures are calculated in 'Flowsolve'. This loop is repeated until T_{stop} is reached.

Bibliography

[1] S. Ergun, 'Fluid flow through packed columns', Chem. Engng. Progs. **48**, p. 89 (1954).

[2] C.Y. Wen, Y.H. Yu, 'Mechanics of fluidization', Chem. Engng. Progs. Symp. Ser. **62**, p. 100 (1966).

[3] R.B. Bird, W.E. Stewart, and E.N. Lightfood, 'Transport phenomena', John Wiley & Sons, New York (1960).

[4] P.A. Cundall, O.D.L. Strack, 'A discrete numerical model for granular assemblies', Géotechnique **29**, p. 47 (1979).

[5] B.P.B. Hoomans, J.A.M. Kuipers, W.J. Briels, W.P.M. van Swaaij, 'Discrete particle simulation of bubble and slug formation in a two-dimensional gas-fluidised bed: a hard-sphere approach', Chem. Eng. Sci. **51**, p. 99 (1996).

[6] M.J.V. Goldschmidt, J.A.M. Kuipers, W.P.M. van Swaaij, ‘Hydrodynamic modelling of dense gas-fluidised beds using the kinetic theory of granular flow: effect of coefficient of restitution on bed dynamics’, Chem. Eng. Sci. **56**, p. 571 (2001).

[7] Y. Tatemoto, Y. Mawatari, K. Noda, ‘Numerical simulation of cohesive particle motion in vibrated fluidized bed’, Chem. Eng. Sci. **60**, p. 5010 (2005).

[8] R.J. Hill, D.L. Koch, A.J.C. Ladd, ‘The First Effects of Fluid Inertia on Flows in Ordered and Random Arrays of Spheres’, J. Fluid Mech. **448**, p. 243 (2001).

[9] M.J.V. Goldschmidt, ‘Hydrodynamic Modelling of Fluidised Bed Spray Granulation’, Ph.D. Thesis University of Twente, 2001.

[10] M.A. van der Hoef, M. Ye, M. van Sint Annaland, A.T. Andrews IV, S. Sundaresan, J.A.M. Kuipers, ‘Multi-scale modeling of gas-fluidized beds’, Adv. Chem. Eng. **31**, p. 65 (2006).

[11] M.P. Allen, D.J. Tildesley, ‘Computer simulations of liquids’, Oxford Science Publications, Oxford (1990).

[12] C.S. Peskin, ‘The immersed boundary method’, Acta Numerica **11**, p. 480 (2002).

[13] M. Uhlmann, ‘An immersed boundary method with direct forcing for the simulation of particulate flows’, J. Comp. Phys. **209**, p. 448 (2005).

[14] J. Li, J.A.M. Kuipers, ‘Flow structure formation and evolution in circulating gas-fluidized beds’, China Particuology **2**, p. 1 (2004).

[15] M.A. van der Hoef, R. Beetstra, J.A.M. Kuipers, ‘Lattice-Boltzmann simulations of low-Reynolds-number flow past mono- and bidisperse arrays of spheres: results for the permeability and drag force’, J. Fluid Mech. **528**, p. 233 (2005).

3

Wall-induced Granular Convection

ABSTRACT

In this chapter, wall-driven convective motion in granular systems under vibration is investigated. A pseudo-2D experimental set-up was constructed in which the convection was generated via a controlled roughness at the side walls. The optical measurement technique Particle Image Velocimetry was used to obtain whole field particle velocity information. This allows for direct 'one-to-one' comparison with results obtained from numerical simulations. It was found that the model was capable of reproducing trends that were observed in our own experiments and those reported in literature. However, the convection strength was usually over-predicted in the simulations.

3.1 Introduction

When a non-equilibrium state is created in a continuous medium (i.e., a medium that may be described by Navier-Stokes type equations), convection currents can occur, a phenomenon that has drawn the interest of many researchers in the past. In liquids for example, temperature gradients can cause the formation of circulation patterns, the so called Rayleigh-Bénard convection [2]. In granular media subjected to vertical vibrations, convection currents may also be observed depending on the applied vibration parameters and the properties of box and particles. Two mechanisms have been proposed which explain the origin of the currents; the first mechanism recognizes the fluid-like behavior of the granular material and an analogy to Rayleigh-Bénard type convection is proposed, to which end a 'granular temperature' is introduced. The second mechanism is based on the observation that particles go down near the side walls and up in the center of the bed. In this case, wall friction causes the development of convection currents. It is now generally accepted that the first mechanism (diffusion of temperature) is at work in relatively dilute granular systems, while the second mechanism (wall-driven convection) is found in dense systems [1, 15]. In this chapter we focus on dense granular systems, where wall friction is dominant.

Clément *et al.* [4] were among the first to report on the capital role that boundaries and solids friction can play on roll formation and heaping, on the basis of 2D experiments. Knight *et al.* [9] used magnetic resonance imaging (MRI) and tracer particles to probe convective granular flow in a non-intrusive manner. They coated the interior walls of their 3D experimental set-up with particles in order to control the wall roughness and thus insure reproducible flow. In their particular 3D set-up, they characterized both the depth and radial dependence of the vertical flow velocity. Hsiau and Chen [12] studied granular convection in a 2D vertically vibrated bed, where the convection was generated by roughened side walls. They used image processing techniques and particle tracking to obtain the particle velocity field and found that the convection flow rate possessed a power law dependence on the vibration velocity amplitude.

With this study, we aim to obtain further experimental data for the wall-driven convective motion in granular systems. On the one hand, we want to investigate the viability of the optical measurement technique particle image velocimetry (PIV) for obtaining the particle flow field in a vertically vibrated system. On the other hand, we want to compare the experimentally obtained velocity data directly with numerical simulations using the model described in Chapter 2, both qualitatively and quantitatively. Apart from this, convection is considered to be important in the well-known Brazil Nut Effect (size segregation) [6–8] and in the segregation of fine bronze and glass particles (Chapter 4, Leaper *et al.* [3]).

In this experimental study, the wall-driven convection is generated by attaching glass beads with the same diameter as the bed material ($d_p \sim 2.5$ mm) to the side walls. We determine the time-averaged particle velocity field using particle image velocimetry (PIV) and compare this velocity data with calculation results from our simulation model. We also perform a sensitivity analysis of the simulation results with respect to some of the simulation parameters. The layout of this chapter is as follows. We will start with a description of the optical measurement technique (PIV) that was employed. After this, we briefly discuss the set-up of both the experimental and simulation systems, and finally we present the results of both experiments and simulations and draw conclusions.

3.2 Particle Image Velocimetry

3.2.1 Introduction

The measurement technique employed in this work is particle image velocimetry (PIV). PIV, originally developed in the field of experimental fluid dynamics, constitutes a non-intrusive optical measurement technique which can be used to obtain the instantaneous fluid velocity field of a continuous fluid [5, 11]. To visualize the flow in transparent fluidic systems, small tracer particles are dispersed. As the fluid is illuminated by a laser sheet, the tracer particles reflect light and an image can be recorded. The basic philosophy of PIV is to record two images with a short time delay and determine the displacement of the tracer particles between the two images with a correlation algorithm. Another method (Particle Tracking) also uses the displacement of particles to determine the velocity, but the difference between the two is the seeding density. Particle Tracking does not allow for high seeding concentrations, since in that case the identity of the individual tracers may be lost. To allow for the higher seeding concentrations, PIV follows tracer *patterns* instead of individual tracers, by means of correlation algorithms. In subsequent analysis, the images are divided in multiple areas and a velocity field can be obtained. More recently, PIV has also been successfully applied to granular systems [14, 16]. In this case no laser is required, since the particles are now illuminated directly from the front using halogen lamps. Since granular systems are opaque in nature, these measurements are restricted to the study of particles in the vicinity of the cell faces.

3.2.2 Correlation peak

We now focus on the construction and interpretation of the correlation diagram, and how these can be used to assess the quality of the PIV results. When a PIV analysis is initiated, an image is subdivided into small ‘interrogation’ areas of size $N \times N$ pixels. These interrogation areas do not need to be strictly adjacent to each other. Usually, they overlap, so that a more detailed velocity field is obtained. For each interrogation area a cross-correlation is performed between two subsequent images, according to:

$$R(s_x, s_y) = \frac{1}{N^2} \sum_{i=1}^{N} \sum_{j=1}^{N} (I'[i,j] - I')(I"[i+s_x, j+s_y] - I") \tag{3.1}$$

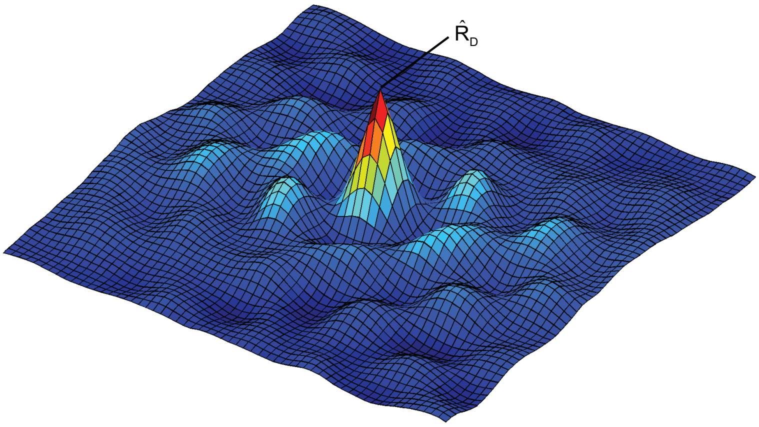

Figure 3.1: *Example of a cross correlation peak diagram.*

for every displacement vector (s_x, s_y). $I'[i,j]$ is the intensity of pixel (i,j) in the first image and $I"[i+s_x, j+s_y]$ is the intensity of pixel $(i+s_x, j+s_y)$ in the second image. Fluctuating noise is eliminated by subtracting the average intensities I' and $I"$ of the first and second interrogation area, respectively. The number of calculations, necessary for the cross-correlation can be limited by using fast Fourier transformations (FFT), with the disadvantage that due to the assumption that the input is of a periodic nature, the thus obtained correlation field is biased for large displacements of the order of the interrogation size. To prevent this, areas of pixels with a value of zero are arranged around the original interrogation areas (zero padding), so that the incorrect correlations yield a correlation value of zero.

Note that at larger displacements (s_x, s_y), the image area that is effectively correlated decreases. This means that the correlation value at that displacement is lower than it otherwise would be, causing that the velocity distribution is biased towards lower velocities. To correction for this, $R(s_x, s_y)$ is divided by the estimated in-plane particle loss to obtain the 'true' cross-correlation $\hat{R}(s_x, s_y)$ [16].

Eventually, the correlation procedure yields a 'landscape' of peaks for varying displacements (s_x, s_y) as shown in Fig. 3.1. The tallest peak $\hat{\mathrm{R}}_{\mathrm{D}}$ will be the peak that represents the actual particle displacement; however there will also be random noise peaks which vary in time. The larger the difference between $\hat{\mathrm{R}}_{\mathrm{D}}$ and the largest noise peak, the more accurate the results of the PIV analysis generally are.

The highest peak for an interrogation area is located at a discrete pixel location, due to the discrete nature of the input signal. This would introduce an error of ± 0.5 pixels in the determined displacement. The accuracy can be increased substantially by curve fitting on the dominant displacement peak. In our case, the displacement is determined by applying a (multi point) Gaussian peak fit to the correlation peak [16]. Of course, the instantaneous velocity can now be obtained by dividing the displacement with the time delay between the images and the magnification of the camera, i.e., $\mathbf{v} = \mathbf{s}/(m\Delta t)$.

Often, the above mentioned method for obtaining the displacement is used twice (called ‘window shifting’). The displacement found in the first evaluation is used to shift the interrogation area in the second image and as a result, a better correlation can be obtained. Further post-processing of the velocity field usually consists of a median test on the obtained vector field [10], which is used for validation. The median filter sorts all neighboring velocity vectors by their magnitude. The median value is the middle value of this ordered sequence and the velocity vector under inspection is considered valid if the deviation with the median is below a certain threshold. Irregular vectors that do not seem to fit in the overall field are marked. After all post-processing, a time-averaged velocity field can be obtained from a sequence of instantaneous velocity fields.

As mentioned in the introduction, usually image pairs are obtained by using a small time delay between the two images so that the displacement curve can be estimated by a linear translation. However, to capture convection rolls in our experimental system, instead we choose the delay between the images in such a way that the bottom position and the granular bed have returned to equilibrium position. In other words, we use a time delay of $1/f_z$, so that we only record the average displacement during one vibration cycle.

3.2.3 Dealing with mixtures

When PIV is applied to granular mixtures, usually no seeding material needs to be added to the granular flow as is common in fluids, since the granular material itself can be used as ‘tracer’. We used a mixture of red and blue glass particles with approximately the same diameter. In the gray scale recordings with the high speed camera, the red particles have a higher intensity, while the blue particle appear as dark spots. The reason for choosing such a particle mixture is as follows. Mixtures of equal-sized particles under vibration can show ordered structures when the particles are closely packed. This commonly occurs when the vibrating plate is in its equilibrium position, moving upward, since at that time the granular bed is compactified. On the one hand, this close packing of the particles is desired, since it allows us to evaluate the net displacement of the particles during one vibration cycle: the observation that the granular bed is in the same position as before, allows to compare the images that can otherwise not be correlated (i.e., in fluidized beds). On the other hand, the ordered structure is problematic when the correlation peak is determined, since it can cause that multiple correlation peaks with similar heights are found. This is due to the inability of the correlation algorithm to distinguish between different rows of particles. The introduction of pattern-breaking dark particles can alleviate this ambiguity, as will be shown in section 3.4 where we will study the correlation signals found with two mixtures of blue and red particles. In the first mixture, the amount of blue particles was 2.7 % and in the second it was 25 %.

3.3 Experimental and simulation set-up

The experimental system consists of a box with a cross-sectional area of 15×1.5 cm and a height of 60 cm, (see Fig. 3.2 for a schematic overview). The principle faces consist of glass plates, the side walls are aluminum strips, to which particles have been attached using an epoxy resin. This set-up gives us a well-defined roughness of the side walls, which is necessary to (i) obtain a reproducible and stable convective current [9, 12, 13] and (ii) obtain the same roughness in the simulation. The particles are attached to the side walls in 6 vertical columns using a cubic stacking. As a result, the cross-sectional area has been reduced to 14.5×1.5 cm. The bottom consists of a sintered metal plate. The particles used in the vibrated bed consist of red and blue glass spheres with a diameter d_p of 2.473 mm and 2.334 mm, respectively; blue particles were also glued to the side walls. The small difference in diameter did not lead to significant segregation during the experiments. The entire system can be viewed as effectively 2D, since the size of the y-direction (depth of the bed) is limited to 6 particle diameters.

The experimental box is mounted on a shaker (Tira TV 50301), which can deliver a well-defined, sinusoidal driving, with a force up to 2700 N. The sinusoidal driving is specified by a vibration frequency f_z and amplitude A_z. The acceleration Γ, non-dimensionalized by gravity, is defined as:

$$\Gamma = \frac{A_z {\omega_z}^2}{g_z} \tag{3.2}$$

with g_z the acceleration due to gravity and $\omega_z = 2\pi f_z$. Further, the non-dimensionalized velocity amplitude is defined as:

$$V_b = \frac{A_z \omega_z}{\sqrt{g_z d_p}} \tag{3.3}$$

An accelerometer (Endevco Isotron 751-100) measures the vibration characteristics and a control loop ensures that the desired operating conditions are obtained. A high speed digital camera (LaVision Imager Pro) is positioned in front of the bed to record the images for PIV analysis, where two halogen lamps are used to illuminate the set-up. The air in the box was humidified in order to avoid effects of static electricity.

The granular bed consists of approximately 20,000 particles. A mixture of 75 % red and 25 % blue spherical glass particles is used, which corresponds to a granular bed height of approximately 15 cm. Optical access to the lower 6 mm of the bed is not possible for construction reasons and therefore no velocity information can be obtained for that region.

Experiments were carried out with vibration parameters in the range of 20 to 50 Hz and amplitudes in the range of 0.9 to 5.62 mm, so that the dimensionless acceleration Γ ranges from 4 to 25.

In the simulations, we used the discrete particle model for vibrated beds as described in Chapter 2. For this particular system, ‘roughened’ side walls have been

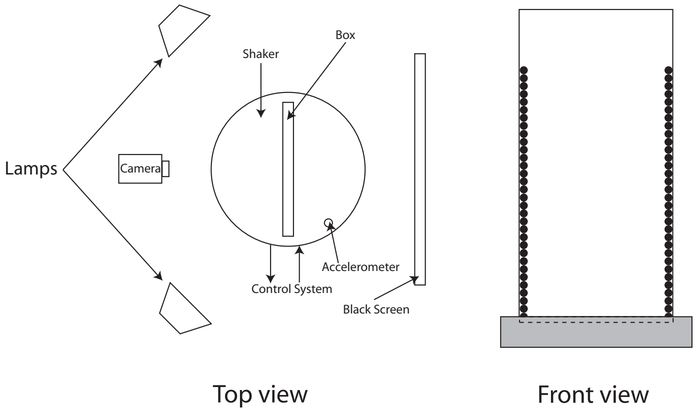

Figure 3.2: *A schematic overview of the experimental set-up.*

implemented, which are detailed in the same chapter. We used particles with the same diameter as in the experiments, namely 15,000 red particles ($d_p = 2.473$ mm) and 5,000 blue particles ($d_p = 2.344$ mm). The density (ρ_p) of the particles is 2525 kg/m^3. The value for the normal and tangential restitution coefficient (e_n and e_t) is 0.97 and 0.33, respectively, and the friction coefficient μ_{pp} is set to 0.10. For the wall interactions we use the same values. For the normal spring stiffness k_n we use a value of 20,000 N/m and for the tangential stiffness a value of 6425.3 N/m is used. The time step used for updating the flow field information is 5.0.10^{-5} sec.

For quantitative comparison between experiment and simulation, we need to obtain the instantaneous velocity fields from the simulation. In order to do so, the simulated box was treated in the same manner as the experimental box: the 'interrogation' areas were chosen the same size and for each area, the average velocity was determined as:

$$v_{x,j} = \frac{\sum_{i=1}^{n} (x_{i,t+\Delta t} - x_{i,t})}{n\Delta t} \qquad \forall i \in \text{cell } j \tag{3.4}$$

and

$$v_{z,j} = \frac{\sum_{i=1}^{n} (z_{i,t+\Delta t} - z_{i,t})}{n\Delta t} \qquad \forall i \in \text{cell } j \tag{3.5}$$

where 'v' is the average velocity in the interrogation area, x_i and z_i the coordinate of particle i, n the number of particles with the center of mass in the computational area and $\Delta t = 1/f_z$ the elapsed time between the data sets. Only the particles at the front wall of the simulated box were included in the analysis, in analogy to the experimental PIV results.

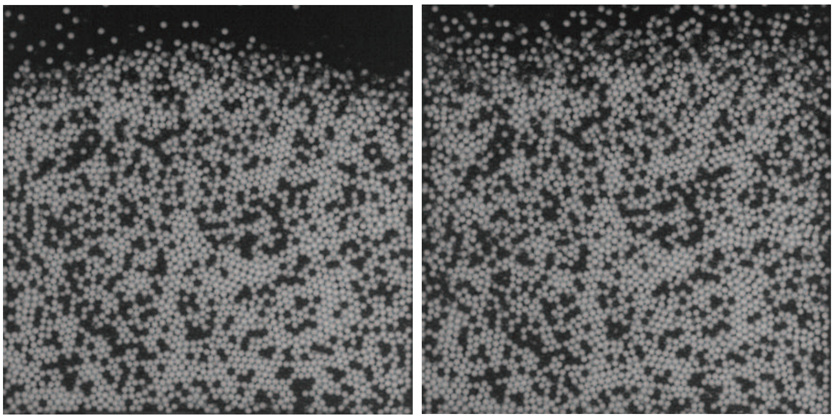

Figure 3.3: *Two images, taken with a time interval of 0.05 sec ($f_z = 20$ Hz). The packed structure of the bed can be clearly observed. Mixture with 25 % blue and 75 % red particles.*

3.4 Results and discussion

In this section we discuss the results obtained from both the experiments and the simulations. We will start, however, with an investigation on the suitability of the modified PIV correlation method that we used in obtaining the instantaneous particle velocity field.

3.4.1 Correlation diagram

The feasibility of the image pairs used for correlation was studied by analysis of the obtained correlation diagrams under severe vibration conditions, namely $f_z = 20$ Hz, $A_z = 5.62$ mm ($\Gamma = 9.04$). As mentioned earlier, the PIV analysis is carried out in two stages. In the first stage, the velocity vectors are determined, which are subsequently used in the second stage for window shifting, so that a better correlation can be obtained. In all cases, zero-padding was employed to avoid problems associated with periodicity. Additionally, a filter for avoiding correlation of the background was used and configured in such a way that all background pixels that are below a certain intensity were set to the value of 0. This threshold value was determined to be the intensity of regions where no particles were present. Two particle mixtures were investigated: one with 25 % blue particles and another with 2.7 %. In the images, the particles have a diameter of approximately 8 pixels and the size of the interrogation area equals 64×64 pixels.

Correlation: 25 % blue particles

In Fig. 3.3, we first consider a particle mixture of 25 % blue particles (dark) and the 75 % red particles (light). In Fig. 3.4, the resulting instantaneous displacement

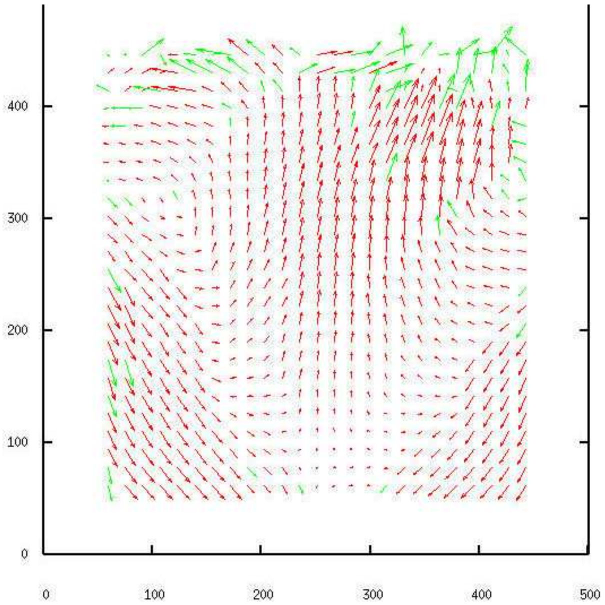

Figure 3.4: *Resulting displacement vector field, obtained from the images of Fig. 3.3. The vector (1,1) is located in the upper left. The x- and z-axis specify the location of the vectors in pixels. Of the 625 obtained vectors, 82 were marked as outliers when a median filter was applied. Usually, the outliers are found at the top side of the granular bed and near the walls.*

field obtained from Fig. 3.3 is shown. In order to test whether the correlation peak could be correctly determined from the images in Fig. 3.3, an analysis on the first correlation was performed, i.e., the step in which the vectors for window shifting are determined. For different sections of the image (near the side walls, top and in the middle of the bed), the correlation diagram was constructed and analyzed. It was found that the upper section of the granular bed (i.e., the upper 5 rows of vectors) usually show multiple peaks in the correlation diagram. This anomalous correlation was attributed to the fact that the granular bed shows severe expansion in that region (as can be seen in Fig. 3.3), during which the correlation between patterns are lost. Also the two columns nearest to the roughened side walls often exhibit these problems. Here however, anomalous correlation was caused by loss of pattern and the strong velocity gradients inside the correlation cell. By contrast, the other areas are not so strongly affected by these problems, commonly giving an unanimous correlation peak, see e.g. Fig. 3.7.

After window shifting is applied, the second correlation plane shows improvement for the areas near the walls and for the interior cells, however, the correlation of the top part is still variable and unreliable. In conclusion, we found that PIV analysis could be successfully applied to the interior cells of the granular bed, but near the walls and the top of the granular bed problems could arise, due to loss of

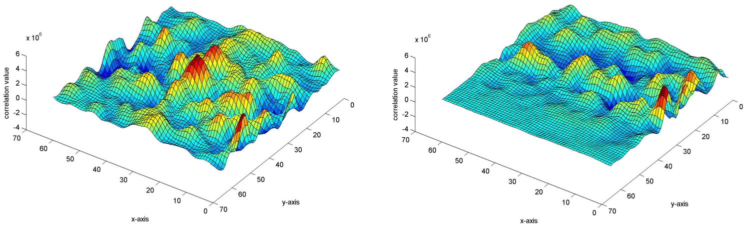

Figure 3.5: *Correlation diagram without window shifting of the top left (1,1) and right vectors (24,2) of Fig. 3.4. Multiple correlations can be observed.*

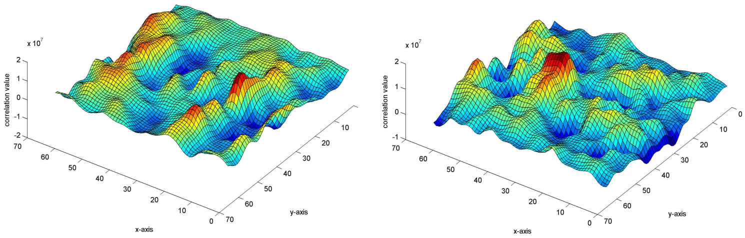

Figure 3.6: *Correlation diagram without window shifting near the right (1,15) and right (25,13) walls of Fig. 3.4. Multiple correlations can be observed.*

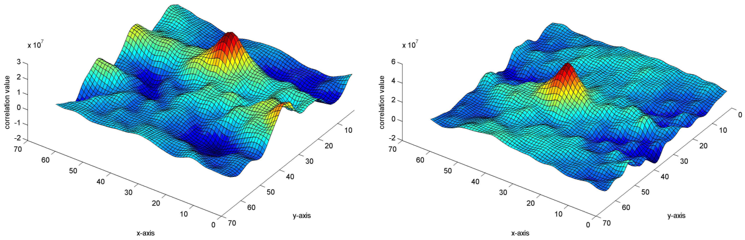

Figure 3.7: *Correlation diagram without window shifting for interior cells (15,15) and (20,20). Usually, unanimous peaks are found.*

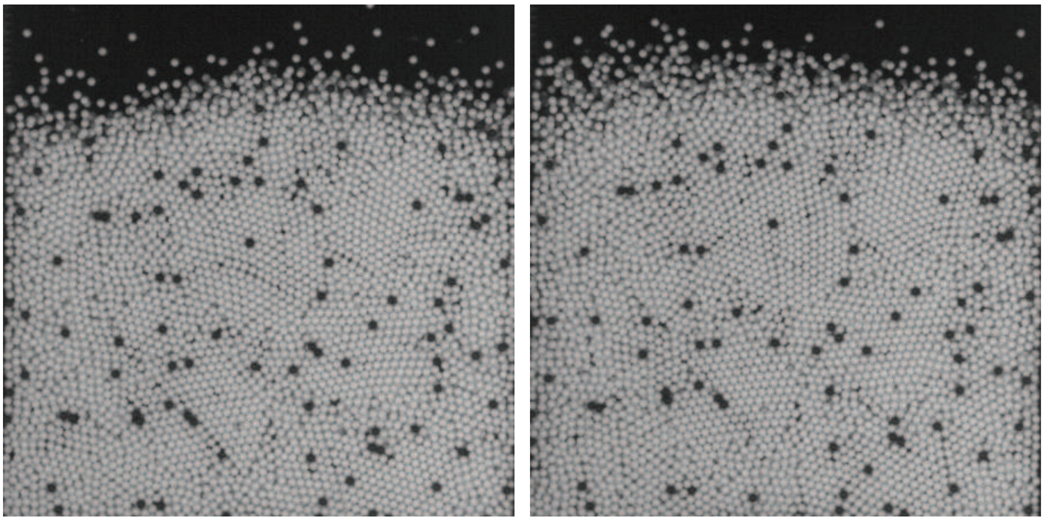

Figure 3.8: *Two images, with a time interval of 0.05 sec ($f_z = 20$ Hz). The packed structure of the bed can be clearly observed. Mixture with 2.7 % blue and 97.3 % red particles.*

patterns and presence of strong velocity gradients. We further found that the median filter usually rejected more vectors than necessary, e.g. some rejected vectors in the lower (packed) section of the bed did not seem wrong on the basis of visual inspection (Fig. 3.4) considering the rest of the vector field. A remedy would be to adjust the discard value for each different experiment. However in practice this is too labor intensive: for this reason we choose a single, relatively large discard value since it is better to reject a few good vectors than accept a few outliers.

Correlation: 2.7 % blue particles

We next performed a similar analysis as in the previous section on an experiment under the same vibration conditions but now with a mixture of particles, with only 2.7 % blue particles seeded. See Fig. 3.8 and Fig. 3.9. Obviously, the obtained displacement field shows more outliers compared to vector fields obtained from images with 25 % blue particles. Although the obtained instantaneous displacement field looks quite reasonable, the correlation diagrams (Fig. 3.10 to 3.12) show that the signal to noise ratio was unsatisfactory in most diagrams: often it was not clear what displacement was correct.

This can be understood by the observation that the amount of blue particles is much lower compared to the previous case (2.7 % vs. 25 %), causing that particle patterns are more or less similar. Many more possible correlations can be observed in the form of ridges or multiple peaks of similar size. Even in the packed sections problems are occurring, which was not the case for the 25 % mixture. Window shifting does not alleviate the problems. In conclusion, we found that mixtures with 2.7

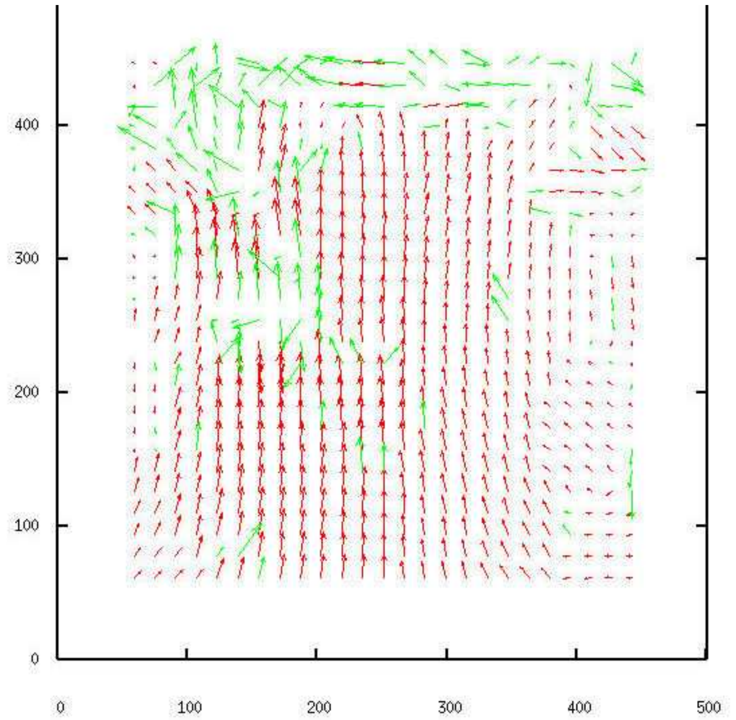

Figure 3.9: *Resulting displacement vector field, obtained from the images of Fig. 3.8. The vector (1,1) is located in the upper left. The x- and z-axis specify the location of the vectors in pixels. Of the 625 obtained vectors, 162 were marked as outliers when a median filter was applied. Usually, the outliers are found at the top side of the granular bed and near the walls.*

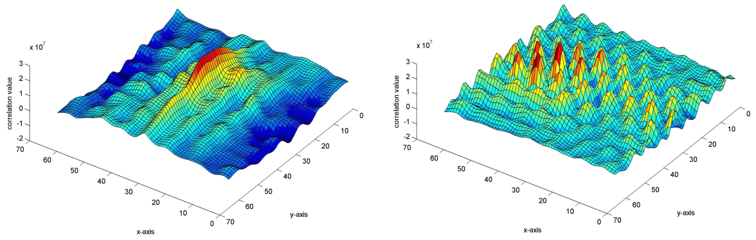

Figure 3.10: *Correlation diagram without window shifting near the left (1,20) and right wall vectors (25,20) of Fig. 3.9. Multiple correlations can be observed.*

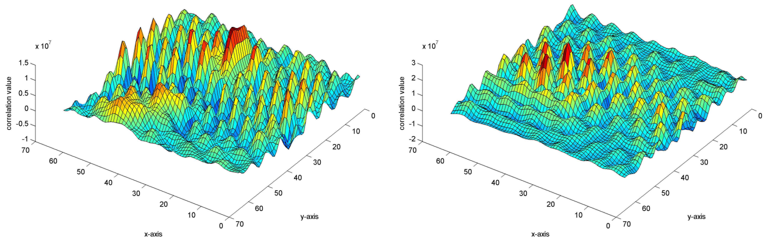

Figure 3.11: *Correlation diagram without window shifting for interior cells (15,15) and (20,20) of Fig. 3.9. Multiple correlations can be observed.*

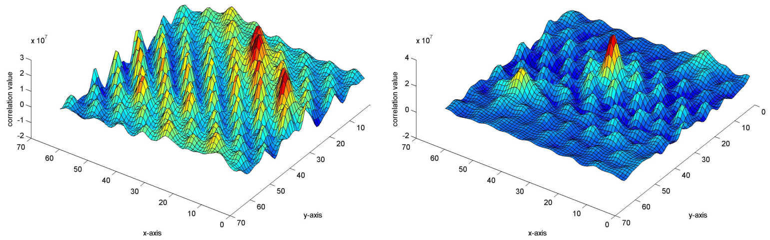

Figure 3.12: *Correlation diagram without window shifting for interior cells (10,20) and (20,15). of Fig. 3.9. Multiple correlations can be observed.*

% blue particles were less suitable for the PIV analysis than the 25 % mixtures.

3.4.2 Data processing

In this section we will discuss the post processing of images obtained from experiments as well as the data obtained from the simulations. We will first discuss the parameters used to obtain the instantaneous velocity fields, that is, the average velocity field after one vibration cycle.

In the construction of the vector plot, we used interrogation areas with an overlap of 75 % so that a sufficient number of vectors could be obtained (i.e., 625). For the construction of the time-averaged vector field, a total of 800 instantaneous fields were used. The averaging method calculates the average displacement for a specific interrogation area, where vectors that have been marked by the median test are not taken into account for the time averaging.

The results from data sets with different vibration parameters or from within a data set, were compared on basis of 3 criteria. For comparison of qualitative nature, (i) the time-averaged vector field is used. For more quantitative comparisons, (ii) a velocity histogram and (iii) radial velocity profiles of the time-averaged field were used. To construct the velocity histogram, the number of v_x and v_z components in a certain velocity interval were counted. The data is displayed as the percentage of velocity vectors in a certain interval and can be determined in a regular as well as a cumulative manner: in a regular velocity histogram, vectors are added to the appropriate velocity interval, whereas in the cumulative plot, all the values equal to or smaller than a maximum value are taken into account. The velocity histogram provides a means to extract the relevant information from a large number of vectors, where the whole vector field can be taken into account. The distribution in v_x and v_z vectors is a measure for the circulation time of the granular material. A larger spread in vectors corresponds to a shorter recycle time and thus to stronger convection. This type of plot, however, does not immediately give information about the location of convection centers or boundary layers near the roughened side walls. The depth dependent radial velocity profiles are used to provide such information.

3.4.3 Simulation results

In order to compare the results obtained for the different vibration parameters and other simulation parameters, it is convenient to specify a base case. The choice of these parameters is arbitrary and we have chosen a case with amplitude $A_z = 2.5.10^{-3}$ m and frequency $f_z = 30$ Hz, so that $\Gamma = 9.05$. Two identical simulations for the base case were performed, only with different initial situations. We found that the convective flow was not always stable and that this had a strong effect on the time-averaged velocity field. Every now and then 'sloshing' (strong horizontal movement between the side walls) could be observed, decreasing the convection strength found in the time-averaged velocity field. Note that also in the experiments some sloshing was observed, only much less frequent and for shorter periods of time, where the dominant form of motion was a stable convection

Using the base case, we determined the minimum number of vibration cycles after which no significant changes occurred in the time-averaged velocity field. It was found that for cases where the convective motion was stable, 200 vibration cycles were enough to obtain a stable average. In practice we used 400 vibration cycles. Time intervals in which instabilities (such as sloshing) occurred, were excluded from the averaging procedure.

In Fig. 3.13 and Fig. 3.14, we show the radial velocity profile for two time intervals of the base case. In Fig. 3.13 we used 200 instantaneous vector fields for averaging and in Fig. 3.14, we used 400. It is found that the profile is axi-symmetric and radial symmetric with respect to the convection centers, which are located at a height of 67 mm and centered 28 mm from the side walls in this particular case.

Since the roughness/friction of the wall is known to have an influence on the convection, it is interesting to evaluate the effect of friction μ_{pw} at the two principle faces on the convection velocity of the base case, also since the precise value of μ_{pw} is not known. Therefore, in addition to the standard value of 0.1, we also examined values of 0.3 and 0.6. As expected, we found that the increased wall friction led to significantly reduced convection velocities at the front and back walls. We found that the convection velocity in the center of the granular bed did not differ strongly from the velocities at the front and back walls at the standard conditions ($\mu_{pw} = 0.1$), but that the difference increases with the wall friction: velocities in the center

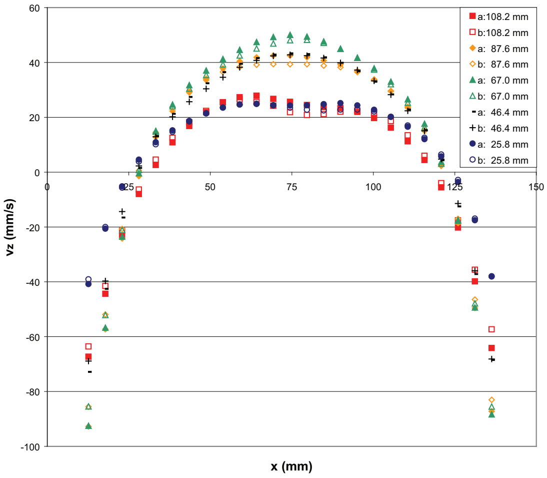

Figure 3.13: *Radial velocity profiles at different heights, for the simulation base case* $A_z = 2.5.10^{-3}$ *m,* $f_z = 30$ *Hz. 200 instantaneous vector fields were used to produce the time-averaged velocity field. Two different time intervals 'a' and 'b', marked with filled and empty symbols, are evaluated. The figure shows that the profiles are nearly the same for both time intervals, the largest deviations are located at the side walls.*

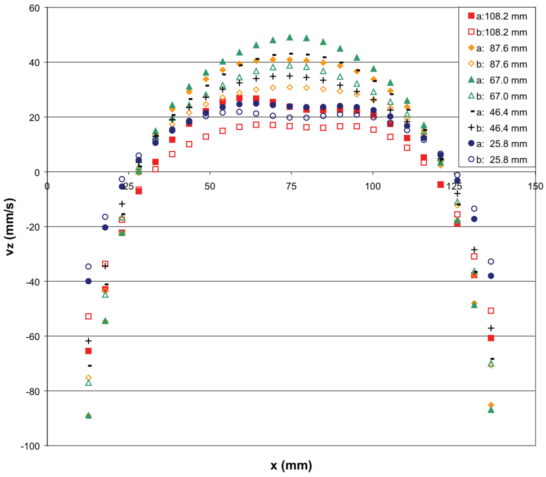

Figure 3.14: *Radial velocity profiles at different heights, for the simulation base case* $A_z = 2.5.10^{-3}$ *m* $f_z = 30$ *Hz. 400 instantaneous vector fields were used to produce the time-averaged velocity field. Two different time intervals, marked with filled and empty symbols, are evaluated. The figure shows larger difference between the intervals, since the interval marked by crosses showed sloshing behavior for a short duration.*

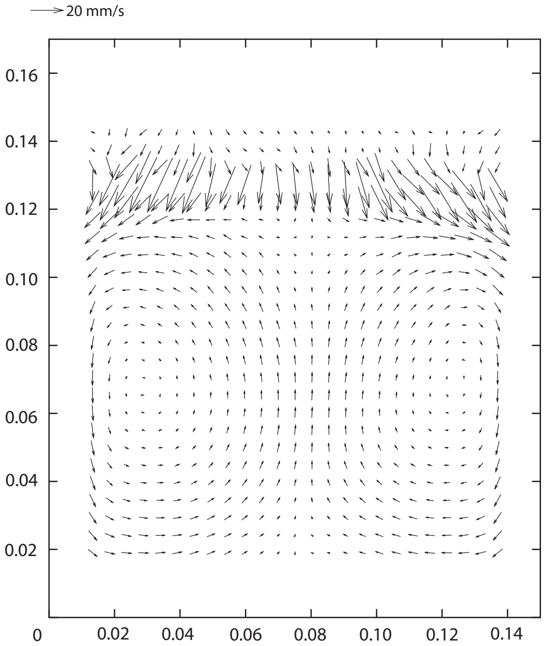

Figure 3.15: *Experimental time-averaged velocity field for vibration parameters* $A_z = 1.41.10^{-3}$ *m and* $f_z = 40$ *Hz. 800 instantaneous fields were used for averaging. The top vectors are not used in analysis, due to the severe expansion (see for example Fig. 3.3).*

were always larger than those at the walls.

The effect of the normal spring stiffness is an important parameter in soft-sphere type of collision models and the sensitivity of the results to it should always be investigated. We therefore increased k_n from the standard value of 20,000 N/m to 40,000; 80,000 and 160,000 N/m. It was generally found that with an increasing stiffness, the circulation velocity was reduced. Probable cause could be that the granular dynamics at the roughened side walls were different due to the increased spring stiffness, where at a higher spring stiffness it is more difficult for particles to pass along the rough walls.

3.4.4 Experimental results

Reproducibility of results is important and we therefore first focus on this matter for the base case of $A_z = 2.5.10^{-3}$ m and $f_z = 30$ Hz. A sample of a time-averaged velocity field can be found in Fig. 3.15. Hereto, we compared cumulative velocity histograms for six different experiments performed on the same day and found the reproducibility was good (see Fig. 3.16). However, results obtained from experiments at different days could deviate strongly (see Fig. 3.17).

We next compare the results of experiments and simulations. As was already

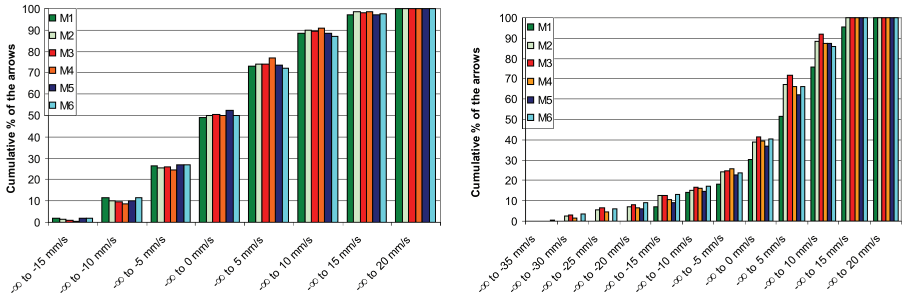

Figure 3.16: *Experimental cumulative velocity histograms for velocity components v_x and v_z for vibration parameters $A_z = 2.5.10^{-3}$ m and $f_z = 30$ Hz. Six different experiments are compared for reproducibility, which was generally to be found satisfactory.*

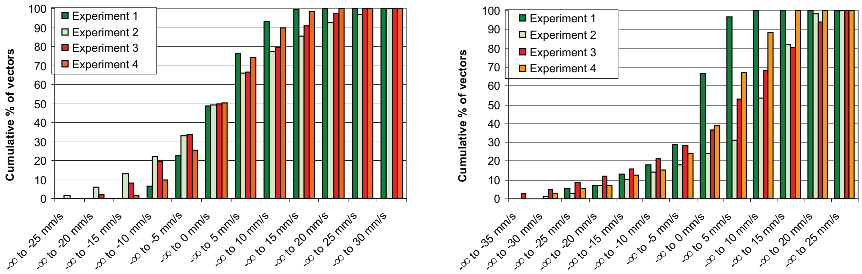

Figure 3.17: *Experimental cumulative velocity histograms for velocity components v_x and v_z for vibration parameters $A_z = 2.5.10^{-3}$ m and $f_z = 30$ Hz. For experiments carried out at different days the reproducibility is worse.*

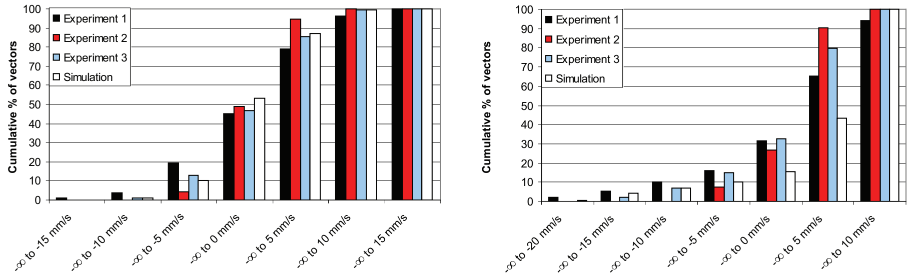

Figure 3.18: *Experimental and simulation cumulative velocity histograms for velocity components v_x (left-hand side) and v_z (right-hand side) for vibration parameters $A_z = 1.41.10^{-3}$ m and $f_z = 40$ Hz. From the figure, it follows that the simulations over-predict the experimental velocities for the vertical direction. The horizontal direction shows a reasonable agreement.*

f_z and A_z	10 % [mm/s]	90 % [mm/s]
20 Hz / 5.62 mm	-30.0	50.0
30 Hz / 2.50 mm	-15.0	11.0
40 Hz / 1.41 mm	-7.5	7.5
50 Hz / 0.90 mm	-1.5	3.0

Table 3.1: *Velocity boundaries in the cumulative velocity plot in vertical direction. The table depicts the velocity range starting from which at least 10 % or 90 % of the vectors is present. The range is a measure for convection strength, where a larger range indicates stronger convection. All experiments were performed at a constant acceleration of* $\Gamma = 9.1$.

pointed out in the previous section, the simulation results often showed fluctuations in the obtained velocity histogram. For a number of simulations, the order of magnitude of the vectors corresponds well to those of the vectors in the experiments. However, for other cases, the simulations usually over-predict the convection strength, see for example Fig. 3.18.

Also, the simulation results were found to be still depending on spring stiffness and wall friction coefficient. Therefore, we can only compare trends in the simulations and the experiments. By doing so, we found that at constant acceleration Γ and increasing frequency f_z, the size distribution of the vectors in the time-averaged flow field decreased (i.e., the convection strength decreased). See table 3.1.

Effectively, the dimensionless velocity V_b (Eq. 3.3) decreases with increasing f_z. The observation that the convection strength decreases with decreasing V_b at constant Γ confirms the experimental findings of Hsiau *et al.* [13]. Direct comparison of the experiments and simulations showed that the trends of the experiments and simulations agree well with each other and with results obtained in literature, only quantitatively do they differ.

We further investigated the width of the down flow region near the side walls at different heights in the granular bed. This width is considered to be important for segregation phenomena based on size. If the size of the down flow region is comparable with the size of the large particles, they can re-enter the granular bed [6]. In connection to this, a ‘whale effect’ [7, 8] was found, in which the particles periodically go up and down. We investigated the width of this down flow region by making a radial velocity profile of the vertical velocity component, for five different heights (see Fig. 3.19). This figure is typical for most experimental data. Although the location of the down flow region varies per set of vibration parameters, the height dependence is weak. This confirms the findings of Hsiau *et al.* [12] and Knight *et al.* [9], who show that the sign change in the vertical velocity to be always at more or less the same radial position.

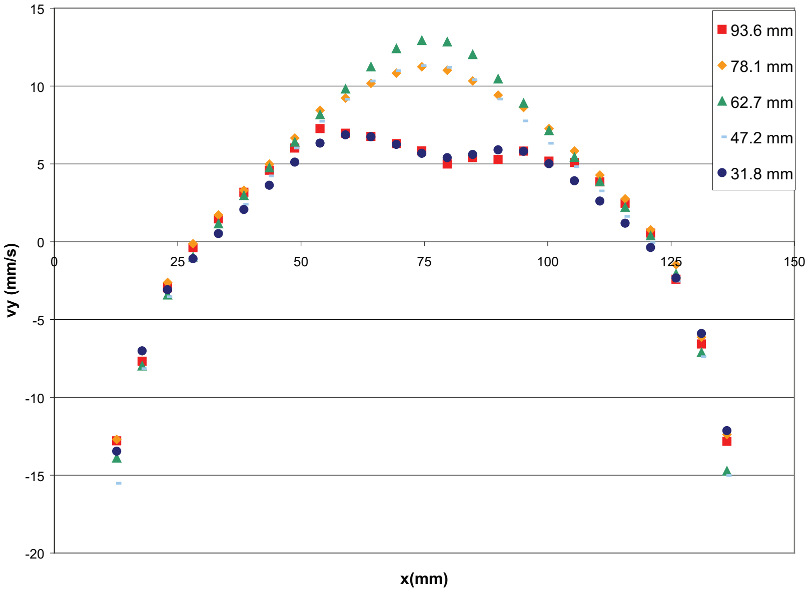

Figure 3.19: *Experimental radial velocity profiles at different heights for vibration parameters* $A_z = 1.88.10^{-3}$ *m and* $f_z = 40$ *Hz.*

3.5 Conclusions

We performed experiments and simulations for a pseudo-2D granular bed under vibration. Convection was generated by the application of a controlled surface roughness to the side walls in both experiment and simulation. We found that with some adaption, the Particle Image Velocimetry (PIV) method could be successfully applied to the experimental system, although in the sections near the side walls and the top of the granular bed problems arise due to the loss of pattern and the occurrence of strong velocity gradients. Sufficient seeding of dark particles was required in order to distinguish patterns in the regularly packed structures that were observed in our experiments. The use of 25 % dark particles was sufficient for our purposes.

We had some problems with the reproducibility of the experimental convective flows, so that deviations up to 20 % could be observed in the cumulative velocity histogram. Additionally, sometimes stable convection was hindered by some kind of sloshing/jamming behavior and this phenomenon was found to have a strong effect on the time-averaged flow field. In the simulations, similar sloshing behavior was sometimes observed.

From the simulations we found that the friction of the principle cell faces (μ_{pw}) becomes important when its value is increased. For the standard value of 0.1, the particles at the principle cell faces have approximately the same velocity as the interior particles. Increase of the friction decreased the convection strength at front and back wall, and introduced velocity gradients in the depth direction of the box. The normal spring stiffness was also found to be important: in general it seemed that an increased normal spring stiffness decreased the size range of velocity vectors, indicating weaker convection.

Bibliography

[1] P. Eshuis, K. van der Weele, D. van der Meer, R. Bos, D. Lohse, ‘Phase Diagram of Vertically Shaken Granular Matter’, arXiv:physics/0608283 v1, 29 Aug (2006).

[2] S. Chandrasekhar, ‘Hydrodynamic and Hydromagnetic Stability’, Edited by Mott, Bullard and Wilkinson, p 9. (Oxford University Press, London, 1961).

[3] M.C. Leaper, A.J. Smith, M.R. Swift, P.J. King, H.E. Webster, N.J. Miles, S.W. Kingman, ‘The behaviour of water-immersed glass-bronze particulate systems under vertical vibration’, Gran. Mat. **7**, p. 57 (2005).

[4] E. Clément, J. Duran, J. Rachjenbach, ‘Experimental Study of Heaping in a Two-Dimensional “Sandpile”’, Phys. Rev. Lett. **69**, p. 1189 (1992).

[5] R.D. Keane, R.J. Adrian, ‘Optimization of particle image velocimeters: II. Multiple pulsed systems’, Meas. Sci. Techn. **2**, p. 963 (1991).

[6] J.B. Knight, H.M. Jaeger, S.R. Nagel, ‘Vibration-Induced Size Separation in Granular Media: The Convection Connection’, Phys. Rev. Lett. **70**, p. 3728 (1993).

[7] T. Pöschel, H.J. Herrmann, ‘Size segregation and convection’, Europhys. Lett. **29**, p. 123 (1995).

[8] J.A.C. Gallas, H.J. Herrmann, T. Pöschel, S. Sokolowski, ‘Molecular Dynamics Simulation of Size Segregation in Three Dimensions’, J. Stat. Phys. **82**, p. 443 (1996).

[9] J.B. Knight, E.E. Ehrichs, V.Y. Kuperman, J.K. Flint, H.M. Jaeger, S.R. Nagel, ‘Experimental study of granular convection’, Phys. Rev. E **54**, p. 5726 (1996).

[10] J. Westerweel, ‘Efficient detection of spurious vectors in Particle Image Velocimetry Data’, Exp. Fluids **16**, p. 236 (1994).

[11] J. Westerweel, ‘Fundamentals of Digital Particle Image Velocimetry’, Meas. Sci. Techn. **8**, p. 1379 (1997).

[12] S.S. Hsiau, C.H. Chen, ‘Granular convection cells in a vertical shaker’, Powd. Tech. **111**, p. 210 (2000).

[13] S.S. Hsiau, P-C. Wang, C-H. Tai, ‘Convection cells and segregation in a vibrated granular bed’, AIChE Journal **48**, p. 1430 (2002).

[14] J.M. Link, C. Zeilstra, N.G. Deen, J.A.M. Kuipers, ‘Validation of a Discrete Particle Model in a 2D Spout-Fluid bed using non-intrusive optical measuring

techniques', Can. J. Chem. Eng. **82**, p. 30 (2004).

[15] J.M. Pastor, D. Maza, I. Zuriguel, A. Garcimartín, J.-F. Boudet, 'Time resolved particle dynamics in granular convection', arXiv:cond-mat/0402040 v2, 16 Dec (2005).

[16] W. Dijkhuizen, G.A. Bokkers, N.G. Deen, M. van Sint Annaland, J.A.M. Kuipers, 'Extension of PIV for measuring granular temperature field in dense fluidized beds.', AIChE Journal **53**, p. 108 (2007).

4

Air-induced Segregation of Fine Bronze and Glass Particles

ABSTRACT

In this chapter, the effect of air on the density segregation of fine, equal-sized bronze ($\rho_s = 8900$ kg/m^3) and glass ($\rho_s = 2525$ kg/m^3) particles under vertical sinusoidal vibrations is investigated by numerical simulation. Both the bronze-on-top and the sandwich configurations as observed in previous experiments by Burtally et al. are found. The simulations allow us to give a detailed explanation of the phenomena. The key observation is the precise timing of the decompaction of the bed with the oscillating gas flow, which will cause the bronze to move to top, due to the difference in acceleration from the air drag. For higher frequencies, the different inertia in collisions will cause the bronze clusters on top to sink through the bed, leading to a sandwich formation. We further investigated the effects of pressure and air forcing, the effect of friction and restitution of kinetic energy in collisions and the box size on the segregation behavior. We find that also friction has a large influence on the sandwich formation.

4.1 Introduction

Granular media subject to vertical vibrations have been the subject of much research in the past decades, not only out of intrinsic scientific interest, but also because of the numerous applications in industry [1]. Most of these studies were concerned with relatively large particles ($>$ 1 mm), where the effects of air can be safely ignored. However, for smaller particles, the effects of air cannot be neglected and a whole new range of interesting phenomena may occur. Pak *et al.* [2] found that the surrounding air plays a crucial role in heap generation, whereas Möbius *et al.* [3, 16, 17] found that the air pressure has a profound effect on the rising time of a large intruder, submerged in a bed of smaller particles, to the extent that the intruders might even sink: the reverse Brazil nut effect. However, one of the most remarkable observations was made by Burtally *et al.* [4, 5], who found experimentally that a mixture of fine bronze and glass particles of equal size (55 μm radius) segregates under vertical vibrations, but only when air is forced through the granular bed. The effect appears to be very robust, and was also found in numerical simulations with very few particles (3,000) and a simplified description of the gas phase [6], yet it is currently not understood in detail why this phenomenon happens. The goal of this work is to shed light on the mechanism underlying these remarkable effects, by means of extensive numerical simulations of systems containing 30,000 spherical particles.

In the experiments of Burtally *et al.*, it was found that the characteristics of the density segregation were directly dependent on the shaking amplitude and frequency. They summarized their findings in a ‘phase diagram’ of acceleration vs. frequency in which each area corresponds to a typical segregation behavior (see Fig. 4.1). During vibration, two major forms of segregation can be observed. The first shows clustering of the bronze particles on top of the granular bed (‘bronze-on-top’), the second results in clustering of the bronze particles between two glass layers (‘sandwich’). Additionally, some metastable regions have been found that show fluctuations between bronze-on-top and sandwich structures. It is clear that the air plays a dominant role in these effects, since no significant segregation is observed under vacuum conditions. One of the effects of the air is that particles are slowed down due to the gas drag. This effect will be stronger for the glass particles due to their lower inertia, however, this would not explain why the heavy particles cluster at the top. Moveover, it was found both experimentally [5] and numerically [6] that air must be *forced* through the granular bed for significant segregation to occur, implying that the mere presence of air is not sufficient.

In order to get better insight into the mechanisms responsible for these segregation phenomena, we have performed computer simulations of the glass-bronze bed under vertical sinusoidal vibration, using a hybrid granular dynamics-computational fluid dynamics code [7]. In this code, the dynamics of the gas phase are governed by the full Navier-Stokes equations, with a two-way coupling between the gas and the solid phase. One of the advantages of numerical simulation is that detailed information can be obtained which is impossible to extract via direct experimentation, such as the gas forces acting upon the bronze and glass particles during a vibration cycle. Moreover, the influence of particle parameters such as the coefficient of restitution and friction can be systematically studied.

This chapter is organized as follows. First, we will discuss the simulation conditions that we used for the bronze-glass system. Then we will show the simulation results for a particular reference system, that is, for a fixed set of parameters connected with the particle properties (coefficient of restitution and friction), gas-phase properties (pressure) and system dimensions (box size and number of particles). For this system we systematically scan the experimental phase diagram of Burtally *et al.* [5] and focus on the mechanism behind the two major forms of segregation. Next, we vary the parameters that were hitherto kept fixed, in order to see what their effect is on the segregation. In particular, we determine the effect of pressure and air forcing, the effect of friction and restitution of kinetic energy in collisions, and the box size on the segregation behavior. Finally, we will shorty summarize and draw conclusions.

4.2 Simulation conditions

The simulation method that we used, is detailed in Chapter 2 and will not be further discussed here. For the simulation conditions - unless stated otherwise - the coefficient of restitution is set to 0.97 for the normal and 0.33 for the tangential direction, and the friction coefficient μ_{pp} is set to 0.1, for all particle-particle interactions. These values have been determined from collision experiments for glass particles with a radius of of 750 μm, and were also found to be the most realistic values in a previous simulation study of gas-fluidized beds [8]. It is not *a priori* obvious, however, that the same parameters apply to 55 μm radius particles, or for bronze-bronze and glass-bronze interactions. Unfortunately, for such small particles these parameters are very difficult to measure. For this reason, we have tested the effect of varying the collision parameters in section 4.6. For particle-wall interactions we use the same parameters as for particle-particle interactions.

In principle, the normal spring stiffness (k_n) in the soft-sphere collision model is related to a physical property of the particle material, namely the Young modulus. For computational reasons however, the spring stiffness is set to a much lower value, so that the time step used for the integration of the equations of motion of the particles can be kept relatively large; the drawback is that the overlap between the spheres is larger than the deformation that occurs during a collision in the real situation. We tested the effect for a bronze-on-top as well as a sandwich system using a normal spring stiffness of 20, 200 and 2000 N/m. Although the formation time of the sandwich can differ when another stiffness is used, it did not affect the final results of the calculations. Therefore, in this work, a spring stiffness in normal direction of 20 N/m was used. The corresponding value of the tangential spring (k_t) was 6.425 N/m for the reference collision parameters. The time step used for integrating the equations of motion of the particles was 2.08.10^{-6} s and the one for updating the gas phase information 2.5.10^{-5} s.

We used free-slip boundary conditions between the gas phase and the box walls.

The box itself is a closed system, containing air at atmospheric pressure without gas leaving or entering the system. When so desired, the bottom and top wall could be made permeable for the gas phase, by applying prescribed-pressure boundary conditions, so that the effect of air forcing may be investigated. Using this method, the build up of pressure at the top of bottom of the box can not occur.

4.3 Simulation results for the reference system

We will first study the effect of varying the frequency and amplitude for one particular system - to which we refer as the reference system - where all parameters associated with the solid phase, the gas phase, and the system dimensions, are held fixed. These parameters have been chosen such that they are as close as possible to the experimental conditions. With respect to the system size, we could not match the experimental conditions of Burtally *et al.*: the ground area of the experimental box was 40×10 mm^2 and the granular bed height approximately 20 mm. In order to make the simulation feasible with respect to computation time and computer memory, we had to reduce our simulation system to 8.25×0.65 mm^2 with a granular bed height of approximately 6.5 mm. However, we found that the main segregation phenomena were not affected by modifying the system size. More details on the finite size effects are given in section 4.6, in which we will also investigate the effect of the gas and particle properties on the segregation phenomena.

In our reference system we have an initial situation of 7,500 bronze particles ($\rho_s = 8900$ kg/m^3), randomly mixed with 22,500 glass particles ($\rho_s = 2525$ kg/m^3). Both particle species have a radius of 55 μm, where a Gaussian size distribution ($\sigma = 7.5$ μm) was applied as to avoid excessive ordering of the bed under less vigorous shaking conditions. Note that the box is of limited depth, so that the gas flow field is effectively two-dimensional. We stress, however, that the *particles* can move in three dimensions. As mentioned by Burtally *et al.* [5], the separation is essentially a two-dimensional phenomenon, so that limited depth of the system should not have a significant effect on the observations. We tested this by performing three-dimensional simulations for both bronze-on-top as well as sandwich conditions, using a system with equal width and depth (ground area 4.4×4.4 mm^2) and found similar results.

We have studied different sets of vibration parameters corresponding to the various regions in the experimental phase diagram by Burtally *et al.*. We found that the model is able to successfully predict the main observations by Burtally *et al.*, namely the bronze-on-top configuration for low frequencies, and the sandwich formation for high frequencies. Note that this is the first time that the sandwich structure is reported from numerical simulations. The results from our simulations are marked in the experimental phase diagram in Fig. 4.1. The transient behavior of the metastable regions E, F and G could not be reproduced, however. As in the experiments, we found that no significant segregation occurred under vacuum conditions (see also Fig. 4.7), which we modeled by deactivating the coupling between the gas and particle phase. Also for ambient pressure with porous top and bottom

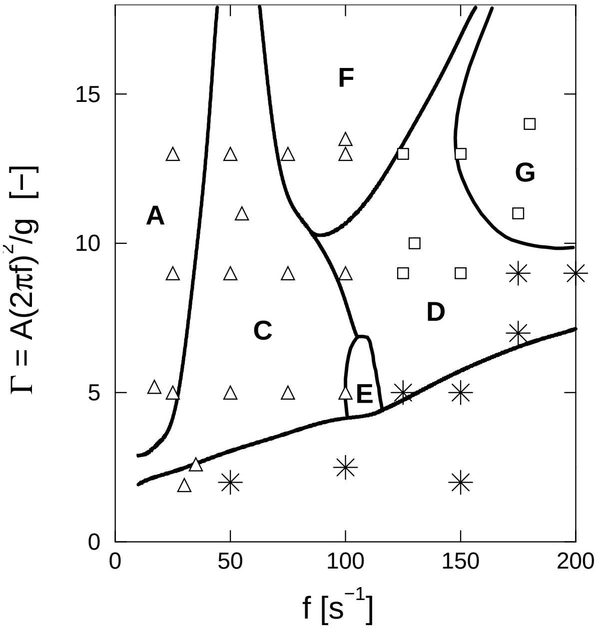

Figure 4.1: *Diagram of acceleration vs. frequency, indicating the different types of segregation for the glass-bronze system, as taken from Burtally et al. [5]. The following segregation phenomena were observed in their experiments. Region A and C: bronze-on-top; Region D: sandwich formation; Regions E, F, G: fluctuations between sandwich and bronze-on-top configurations. The symbols mark the simulation results of this work for the reference system: triangles for bronze-on-top configurations, squares for sandwich configurations, asterix for no segregation. In the simulations we did not find fluctuations between bronze-on-top and sandwich configurations.*

wall, we did not observe any segregation, which was also reported by Burtally *et al.* [5]. More details on this are given in section 4.6. It is interesting to note that in a similar simulation study with 3,000 particles by Milburn *et al.* [15], fluid-driven convection rolls were observed within the separate layers, which strengthened the separation mechanism. In our simulations we did not observe any significant fluid-driven convection, which was most likely caused by the absence of Faraday tilting at our conditions.

4.4 Why does the bronze move to top?

We next want to understand what mechanism is responsible for the bronze particles moving to the top at low frequencies. To this end, we focus on a system driven with a vibration frequency f_z of 55 Hz and a vibration amplitude A_z of 0.9 mm, leading to a dimensionless acceleration $\Gamma = A_z(2\pi f_z)^2/g_z$ of 11. Initially, the

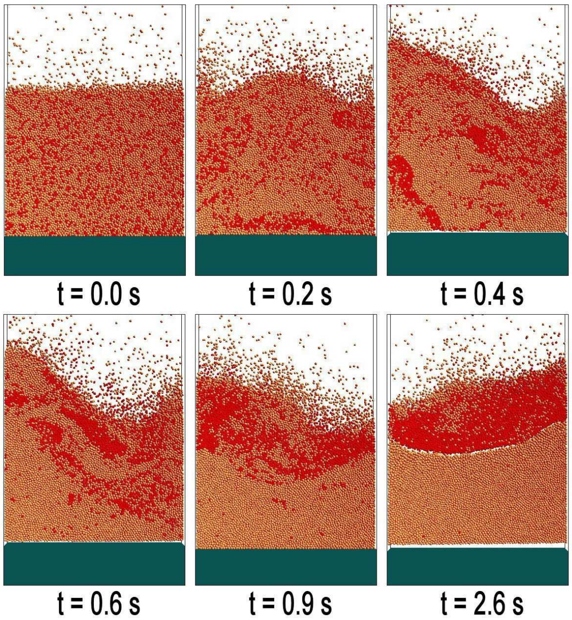

Figure 4.2: *A series of snapshots leading to the bronze-on-top structure* ($A_z = 0.9$ *mm*, $f_z = 55$ *Hz*, $\Gamma = 11$). *Small bronze clusters are formed which migrate to the surface of the granular bed where a layer of bronze is formed that eventually covers the entire width of the box. After segregation, the upper bronze particles are quite active and the bed surface shows severe tilting, however, bronze remains on top.*

system is well mixed, however as time proceeds, bronze and glass start to segregate, see Fig. 4.2. For all of our simulations at atmospheric pressure, we found that the granular bed moves in phase with the bottom plate. Animations reveal that within a single vibration cycle during segregation (i.e., around $t = 0.3$ s), initially bronze and glass are going up together with the bottom plate. When the bed is lifted from the plate, the light glass particles loose momentum more quickly than the heavy bronze particles, and one can clearly observe the glass particles flowing downwards relative to the bronze particles. When the bed is falling down on the bottom plate, the opposite phenomenon is observed. Again the bronze retains its momentum (but now downwards) longer than the glass, however the relative movement is much less in this case since the bed is compactified, in particular in the bottom region. The observation that compaction can lock particles against further movement has been reported previously for the Faraday heap [9] and for the Brazil nut effect [10, 17]. Deactivation of the gravity confirms these findings. When this is done for a segregated bronze-on-top system, the particles rapidly spread throughout the box. The bronze and glass mix, that is, we find small bronze and glass clusters randomly throughout the box. Compact regions do not occur and the locking effect is not present.

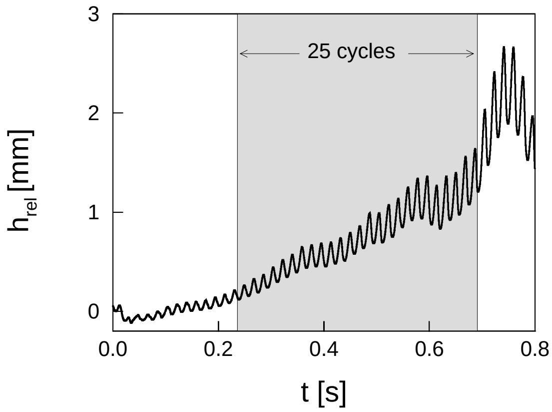

Figure 4.3: *Position of the bronze relative to the glass as a function of time for the bronze-on-top system. For* $h_{\mathrm{rel}} = 0$*, the system is completely mixed, whereas* $h_{\mathrm{rel}} \sim 3$ *corresponds to the situation as shown in Fig. 4.2 on the bottom right. The shaded area marks the data that we used for further analysis by averaging, as shown in Fig. 4.4.*

We now want to quantify the visual observations. In Fig. 4.3 we show the relative position of the bronze and glass particles:

$$h_{\mathrm{rel}} = \langle h_{\mathrm{bronze}} \rangle - \langle h_{\mathrm{glass}} \rangle \ , \tag{4.1}$$

where $\langle h_{\mathrm{i}} \rangle$ is the averaged height of particle species i. It can be seen that the bronze gradually moves upward. Since the motion of the granular bed is in phase with the bottom plate, we average the data of interest over 25 vibration cycles in order to minimize the effect of the fluctuations, where the averaging window is indicated in Fig. 4.3. We found that for this particular time frame the bronze-on-top movement was most clearly observed, and less pronounced for times < 0.2 and > 0.7 s. We start the analysis on the basis of Fig. 4.4 at the point when the bottom plate moves through the equilibrium position. When the granular bed looses contact with the bottom plate, a void is formed between them. As the size of the void increases, the pressure drops so that gas is sucked into the granular bed causing negative gas accelerations on both particle species. As the size of the void starts to decrease, the pressure beneath the granular bed increases and the gas accelerations become positive. The lower section of the granular bed regains contact with the bottom plate and as the granular bed is compacting, the vibration cycle is complete. During this vibration cycle, two regions are distinguished: one of negative and one of positive gas accelerations. These accelerations are a direct result of the interaction between the movements of the granular bed and the bottom plate, which has the effect of a piston, inducing positive and negative pressure gradients within a cycle. The forces acting on the glass and bronze particles are equal (since the particles have equal size), however the accelerations are different, due to the different mass. Note that these accelerations can be almost an order of magnitude larger than grav-

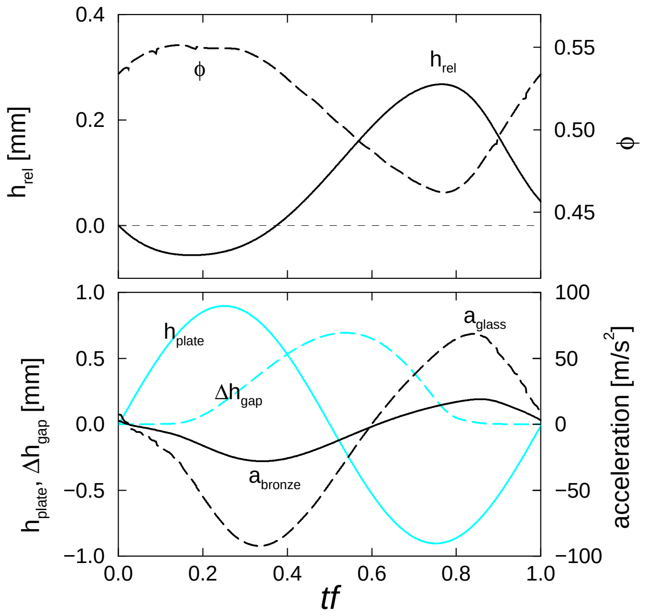

Figure 4.4: *Evolution of the quantities of interest within one cycle for the bronze-on-top system, obtained by averaging over 25 cycles (see Fig. 4.3). Top graph: relative position h_{rel} of the bronze and glass particles (black line) and packing fraction ϕ of the bed (black dashed line). Lower graph: position h_{plate} of the bottom plate (gray line) and the width Δh_{gap} of the gap between the granular bed and bottom plate (gray dashed line). The black solid and black dashed line represent the average acceleration in the vertical direction due to the total force from the gas phase on a bronze and a glass particle, respectively. Note that all quantities are periodic in time, except for the relative position of the bronze and glass particles (black line in top graph), which ends up slightly higher at $tf = 1$ (as compared to $tf = 0$) due to the bed compaction starting at $tf = 0.8$, which hinders the relative movement of the particles. Because of this effect, bronze will gradually move to the top.*

ity. It can be seen from Fig. 4.4 that when the system is most densely packed, h_{rel} does not change significantly, i.e., there is no relative movement. Only when the packing fraction decreases, that is when the granular bed expands in free flight, a significant relative movement occurs. In the regime of negative accelerations, glass moves downward relative to the bronze. At $tf = 0.6$, the direction of the accelerations is changed, causing the relative movement of glass to slow down, come to a stop, and eventually reverse: glass is going up (i.e., h_{rel} becomes smaller again). However, at this time the packing fraction starts to increase since contact between granular bed and bottom plate has been regained: compaction starts from the bottom plate up. Due to the compaction the relative movement becomes much more difficult, so that the bronze cannot regain the position it had at the beginning of the cycle, but ends up slightly higher. After a number of such cycles, the bronze

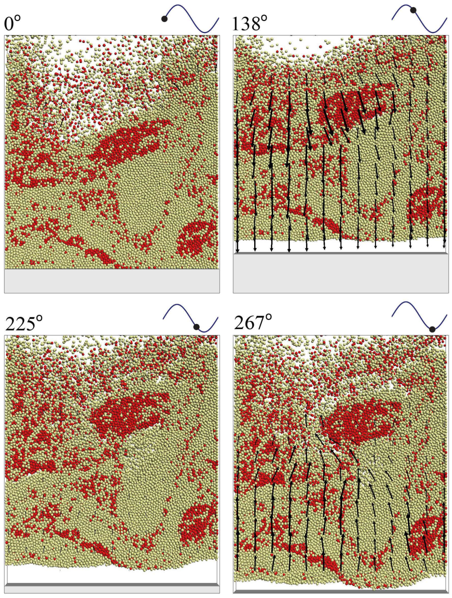

Figure 4.5: *A simulation for bronze-on-top conditions, at four successive phases during one vibration cycle. The vectors indicate the air drag on the particles averaged per CFD cell (only one out of every 2 vectors is shown).*

will have moved to the top of the granular bed (see Fig. 4.3). Note that the difference in gravitational force on the bronze and glass particles does not play a role in this mechanism, but rather the difference in the particle's *inertia*. In Fig. 4.5, the pumping effect of the air during a vibration cycle is visualized in more detail.

4.5 Sandwich system

We next focus on a 'sandwich' system, which is obtained by setting the vibration parameters to $f_z = 130$ Hz and $A_z = 0.147$ mm ($\Gamma = 10$). In Fig. 4.6 we show some snapshots of the simulation. Note that the time scale on which the layer is formed is much longer than for the bronze-on-top system, which already suggests that another mechanism will be responsible for the observed behavior. A similar analysis as for the bronze-on-top system was performed for the first 2 seconds of this simulation. The rate at which (some of) the bronze initially clusters at the top is a factor 25 lower. How can this difference be explained? Due to the smaller amplitude, the void between granular bed and bottom plate is much smaller for the sandwich than for the bronze-on-top system (1.5 vs. 6.5 particle diameters). The time of flight of the granular layer will be smaller for the sandwich system, resulting in a increased packing fraction, varying between 0.56 and 0.59 (compared

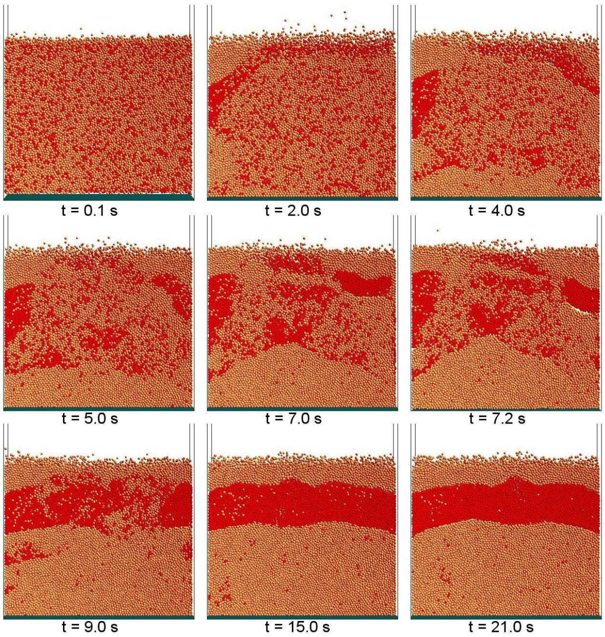

Figure 4.6: *A series of snapshots for the sandwich system* ($A_z = 0.147$ *mm,* $f_z = 130$ *Hz,* $\Gamma = 10$)*. After the formation of the glass-bronze-glass sandwich, the configuration was stable for the time that we simulated (60 s).*

to a 0.45-0.55 for the bronze-on-top system, see Fig. 4.4). This will make it more difficult for the particles to move relative to each other. However, after some of the bronze has clustered on top, a completely different phenomenon is observed. When a bronze cluster at the top becomes sufficiently large, it becomes too heavy for the bed to support it, and it suddenly 'falls' through the bed, setting up a large-scale convection roll. Within this motion, the glass-rich layer just below the bronze cluster is pushed to the bottom where it compactifies, so that the bronze cluster cannot reach the bottom, but ends up in the middle of the bed. This happens first at both side walls (see Fig. 4.6 at $t = 5.0$ s), but eventually all top bronze clusters sink through the bed, so that a bronze-rich middle layer is formed, leaving an almost pure glass layer at the top. At the same time, the weak 'bronze-on-top' mechanism that is still at play causes the middle bronze-rich layer and the bottom glass-rich layer to exchange their impurities. The final result is an almost perfect separation of glass and bronze into a sandwich structure. Note that for water immersed systems, Leaper *et al.* [11] found that vertical vibration would always lead to bronze-on-top, even when initially sandwich structures are formed, suggesting that the sandwich structure might be a metastable state. In our simulation in air, we found that the sandwich layer was stable for the time that we simulated (60 s). Although sometimes convection rolls could be observed within the three separate layers, the apparent shear between the layers did not induce global mixing. Leaper *et al.* explained this with the observation that the granular convection occurs only while the gap is open, at least for water-immersed glass/bronze systems.

The observations for both the bronze-on-top as well as the sandwich system suggest that different segregation mechanisms dominate for different vibration parameters. Convective motion - during which bronze moves downward - can be observed at low amplitude and high frequency vibrations, while relative movement due to the forcing of air is dominant at the higher amplitude vibrations. To further look into this, we studied the vibration series at acceleration $\Gamma = 9$. We varied the vibration frequency from 25 Hz to 200 Hz, with steps of 25 Hz, keeping the acceleration at a constant value of 9, so that the amplitude becomes smaller. We found that when we move from the bronze-on-top to the sandwich region of the experimental phase diagram (i.e., we increase the vibration frequency), the convective mechanism becomes more important. At 25 and 50 Hz, we find the regular relative movement type of segregation. The simulations at 75 and 100 Hz start to show characteristics of the sandwich system: large glass clusters moving downward near the walls. Only for 125 and 150 Hz, a sufficiently large amount of bronze follows in the wake of the glass to form the sandwich. Note that when the vibration frequency is increased, the formation of the sandwich requires an increasingly longer time and for frequencies beyond 175 Hz ($\Gamma = 9$), we did not observe significant segregation for the time that we simulated.

We further investigated the sinking behavior of the bronze clusters under sandwich conditions. The question that arises is which effect is responsible for this sinking behavior: (i) the difference in heavy mass, i.e., the different gravity force on the bronze and glass particles, or (ii) the difference in inertial mass in collisions, which will cause a bronze cluster to penetrate the glass layer when pounding on it in the second part of the vibration cycle. To answer this question we have performed purely artificial simulations, where we modified the differential masses. The different values for the masses are summarized in table 4.1. We first investigated case (a), where the particles have the same gravity. Hereto, we choose the standard particle densities of 8900 and 2525 kg/m^3 for the particle species, but rescaled the acceleration due to gravity with 4100/2525 for glass and 4100/8900 for bronze so that the gravity force is the same for both species. Doing so, we still observed the sinking of the bronze clusters, although less pronounced than under ‘real’ conditions, so that the final result is a mixed sandwich and bronze-on-top state. We chose a value of 4100 kg/m^3, in order to keep the total mass of the granular bed to the same value as under reference conditions. However, we also investigated scaling with 2500 instead of 4100 kg/m^3 and found similar results. We next investigated case (b): the effect of the particles having the same inertial mass in collisions. To this end, we used a density of 4100 kg/m^3 for both particle species. We then rescaled the gas and gravity accelerations of glass and bronze by 4100/2525 and 4100/8900, respectively. Thus, the differential effects of drag and gravity were restored, and the effects of differential mass in collisions removed. We found that the characteristic sinking of bronze clusters as precursor to sandwich formation did not occur. We finally investigated case (c), namely the effect of having only a difference in gas forces. Here,

	Ref	(a)	(b)	(c)
M_b/V_p	8900	4100	8900	4100
M_g/V_p	2525	4100	2525	4100
$I_{b,coll}/V_p$	8900	8900	4100	4100
$I_{g,coll}/V_p$	2525	2525	4100	4100
$I_{b,gas}/V_p$	8900	8900	8900	8900
$I_{g,gas}/V_p$	2525	2525	2525	2525

Table 4.1: *Values of the different densities [kg/m^3] in the artificial sandwich simulations. The subscripts 'b' and 'g' denote bronze and glass, respectively. M_b is the heavy mass, $I_{b,coll}$ the inertia in collisions and $I_{b,gas}$ the inertia due to the gas. V_p is the volume of a particle.*

again, we used a density of 4100 kg/m^3 for both particle species and rescaled only the gas accelerations of glass and bronze by 4100/2525 and 4100/8900, respectively. We now found that bronze goes to the top even for vibration conditions where normally sandwich structures are observed.

From the observations in our artificial simulations, it becomes clear that under 'real' conditions the different inertia in collisions makes that the bronze clusters on top sink through the bed, leading to the sandwich formation.

4.6 Varying the gas, particle and box parameters

4.6.1 Effects of pressure

From the experiments of Burtally *et al.* [4, 5], the simulations of Biswas *et al.* [6] and from this work (section 4.3 and [18]) it is clear that the forcing of air through the system is responsible for the segregation phenomena. Indeed, we found that when simulating the system at vacuum conditions, no segregation is found, irrespective of the shaking parameters. A series of snapshots for one particular system ($f_z = 55$ Hz, $\Gamma = 11$) is shown in Fig. 4.7. The bed surface was unstable and surface waves traveled from sidewall to sidewall. The bronze particles showed only a tendency to form small clusters (typical size less then ten particles), but remained mixed with the glass particles. Further evidence of the importance of air forcing was obtained by applying prescribed-pressure boundary conditions to the bottom and top wall of the box. Effectively, such a boundary condition prohibits pressure build-up, as is experimentally the case when a porous plate with negligible pressure drop is used. We found for both bronze-on-top as well as the sandwich case that if either the bottom or the top wall was made porous, segregation would still occur. However, if *both* walls were made porous, no segregation occurred. We also carried out simulations with larger particles (0.5, 1.5 and 2 mm diameter) under shaking conditions where for 110 μm diameter particles a bronze-on-top configuration was found. Convection rolls developed in the granular bed and some slight coarsening could be observed. However, no major segregation did occur for these larger particles, confirming the importance of the gas for smaller sized particles.

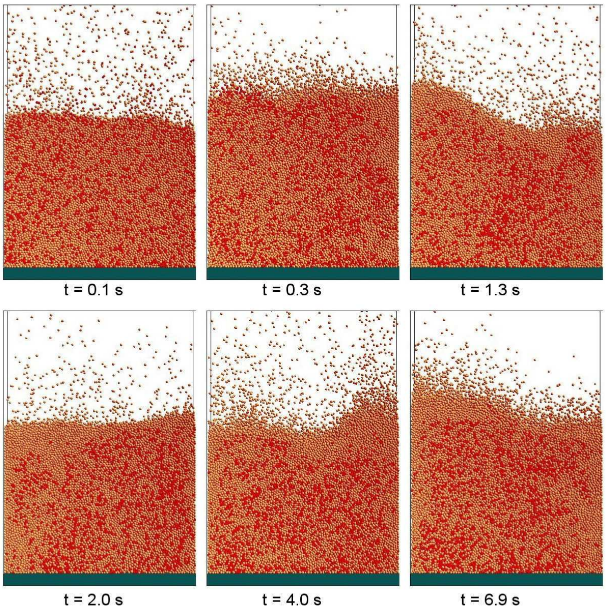

Figure 4.7: *A series of snapshots for the bronze-on-top vibration parameters* ($A_z = 0.9$ *mm,* $f_z = 55$ *Hz,* $\Gamma = 11$) *for vacuum conditions. The granular bed moves wildly and no significant clustering is observed.*

Since the presence of air has such a pronounced influence even at atmospheric pressure, it is interesting to see what happens when we increase the pressure further to 100 bar, again for both regimes C and D. Note that even for 100 bar, the density of the gas phase is still small compared to the density of the particles (5 %), so that we can still neglect the 'added mass' force associated with the displacement of the continuous phase.

For regime C, we find that at 100 bar bronze clusters are formed almost immediately (within 0.1 s) throughout the granular bed, see Fig. 4.8. The clusters coalesce and move to the top. The most important difference with the simulations at atmospheric pressure is that the tilting of the bed surface during the segregation is suppressed. When the bronze particles have reached the bed surface, some small bronze clusters remain in the glass phase and also in the bronze phase a few glass particles remain. We remind that, at atmospheric conditions glass can be found in the bronze phase and occasionally glass is even spilled over the bronze due to surface tilting; the 100 bar simulations however exhibit nearly no tilting. Glass particles remaining in the bronze-rich layer eventually move downwards to join the bulk glass layer underneath. The result is much purer bronze phase as compared to the atmospheric case.

When the pressure for regime D (sandwich structure) is increased to 100 bar we observe *slower* clustering compared to the atmospheric case. While we find a

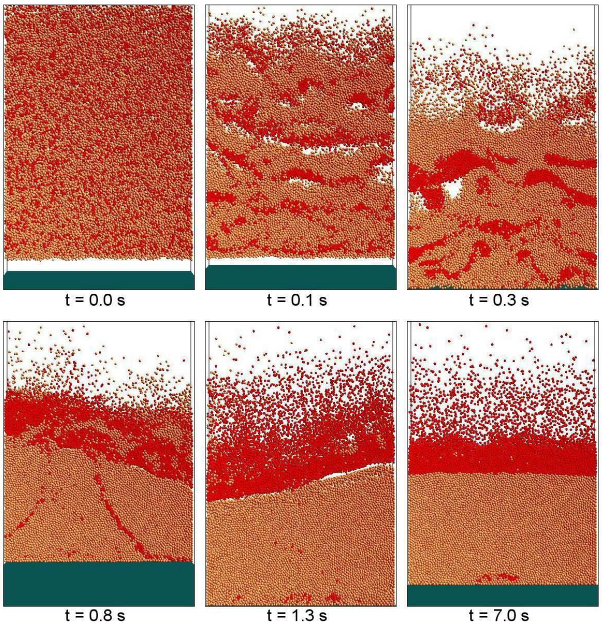

Figure 4.8: *A series of snapshots leading to the bronze-on-top structure ($A_z = 0.9$ mm, $f_z = 55$ Hz, $\Gamma = 11$) for 100 bar gas phase pressure. The bronze particles immediately form clusters, that move to the top of the granular bed. In contrast to atmospheric pressure, the bronze layer contains only a few glass particles and almost no surface tilting is observed.*

sandwich in approximately 10 seconds for atmospheric pressure, for the 100 bar simulation we observe a sandwich only after 30 seconds. We find that the bronze clusters fall through the granular bed at a much slower rate compared to the atmospheric case. Apparently, the increased density (and thus drag force) at higher gas pressures hinders the sinking of bronze clusters; it may be that the bronze-on-top effect becomes more important. Leaper *et al.* [11], who did experiments for water immersed systems, suggest that the 'sandwich' itself may be a metastable state. Following this line, this may explain why the sandwich is more slowly formed in our high pressure simulations.

4.6.2 Effect of particle parameters

We next study the effect of the particle-particle and particle-wall interaction parameters, in particular those that determine the magnitude of the energy dissipation in collisions, i.e., the normal restitution and friction coefficients. It is well known that dissipation drives the formation of clusters in mono-disperse systems like fluidized beds [13] or vibrated beds with multiple compartments [12].

We first study the effect of the particle-particle friction coefficient μ_{pp} and the particle-wall friction coefficient μ_{pw} on the bronze-on-top and sandwich system,

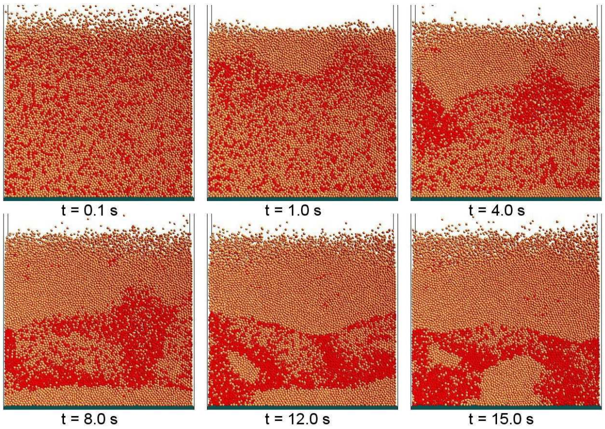

Figure 4.9: *A series of snapshots for the sandwich system* ($A_z = 0.147$ *mm,* $f_z = 130$ *Hz,* $\Gamma = 10$)*, with all friction deactivated. The sandwich is not formed and the bronze gathers at the bottom of the box.*

whilst keeping the other interaction parameters and the gas phase properties the same as for the reference system. We start our analysis with the bronze-on-top case. For the reference system ($\mu_{pp} = \mu_{pw} = 0.1$), the final bronze and glass layers are large and well-defined. Tilting of the bed surface is regularly observed, which occasionally leads to glass from the lower layer spilling over the bronze layer on top. When we redo this simulation, but now with all friction deactivated we find the segregation to be much less pronounced. Although bronze still moves to the top, the top layer is less compact and with a much higher glass content in the top bronze layer. The simulation with only wall friction activated shows similar behavior. By contrast, when we only activate the particle-particle friction (keeping the wall friction to zero), we find that the bronze layer only contains up to 10 % of glass and we observe nearly no surface tilting. It appears that the particle-particle friction is required for a good separation, while wall friction enhances tilting. In a similar manner, we tested the effect of increasing one or both of the friction components to the value of 0.4, while the other value remained at the standard value of 0.1. We found that the qualitative behavior in all three cases was similar to the reference system, that is, bronze clustering and moving to the top after which tilting and subsequent glass spilling is observed. The amount of tilting could be reduced by deactivating the friction of the the two principle box faces.

We carried out similar tests for the sandwich system, the results of which are summarized in table 4.2. In the case that there is no particle-particle friction, we made the remarkable observation that bronze gathers at the bottom of the box, see Fig. 4.9. Starting from an initially mixed state, the bronze appears to percolate downward through the granular bed and a nearly pure glass layer is growing near the bed surface. The boundaries between bronze-rich and glass-rich sections are

$\mu_{\mathrm{pp}} \downarrow \quad \mu_{\mathrm{pw}} \rightarrow$	0.0	0.1	0.4
0.0	Bottom	Bottom	Bottom
0.1	Middle (40 s)	Middle (10 s)	Top
0.4	Middle (20 s)	Middle (10 s)	Top

Table 4.2: *Final position (bottom, middle or top) of the bronze layer for various combinations of the particle-particle (pp) and particle-wall (pw) friction coefficient. The frequency is set to $f_z = 130$ Hz, the dimensionless acceleration to $\Gamma = 10$. In parenthesis we show the time it roughly takes to form the sandwich structure, starting from a mixed state. The central box ($\mu_{pp} = \mu_{pw} = 0.1$) represents the reference system shown in Fig. 4.6. The case $\mu_{pp} = \mu_{pw} = 0.0$ is shown in Fig. 4.9.*

diffuse. We made this observation for all three values of μ_{pw}. When we only have particle-particle friction activated, we still find the sandwich, although the formation time is longer. Next, as in the bronze-on-top system, we increased one or both of the friction components to the value of 0.4, while the other value remained equal to 0.1. When we increased the wall friction to 0.4, we found that the bronze moves to the top via large scale convection currents, and not as the mechanism discussed in section 4.3. When both friction components are set to 0.4, we also find that the bronze moves to the top. When $\mu_{pp} = 0.4$ and $\mu_{pw} = 0.1$, we find the sandwich structure. While in the reference system also some convective motion was observed, we suspect that the strong convective current that brings the bronze to the top for $\mu_{pw} = 0.4$ is generated by the wall. As observed before in the $\mu_{pw} = 0.0$ cases, the wall friction does not seem to be strictly required for the system to lead to a sandwich structure, which suggests that the gas forces and particle-particle friction are sufficient to obtain a sandwich structure. However, when the wall friction dominates ($\mu_{pw} = 0.4$), wall generated convection will deposit the bronze on the top.

We further investigated the effect of wall friction by deactivating the friction between wall and particles only for the principle cell faces, leaving the friction with the two smaller sidewalls and the bottom plate intact. For the $f_z = 55$ Hz, $\Gamma = 11$ case, we observe the regular formation process, namely bronze moving to top, where the main difference with the reference system was that the amount of interface tilting was strongly reduced. For $f_z = 130$ Hz, $\Gamma = 10$, we observed the same behavior as in the reference case (sandwich formation), although the sinking appeared to proceed more readily. For a deep (19.5 mm) granular bed (see also Section 4.6.3), we found that the final depth of the sandwich depended on the presence of friction on the principle cell faces.

We further investigated the role of the wall friction coefficient in 3D simulations, where the ground area was 4.4×4.4 mm^2 and granular bed height 6.5 mm (105,600 particles). For the standard friction parameters, we found the sandwich structure, while deactivation of all friction shows bronze gathering at the bottom of the box, which we also found for the pseudo-2D systems. Having only inter-particle friction, we again found the sandwich, but - as we also observed in the pseudo-2D systems, the formation time is longer.

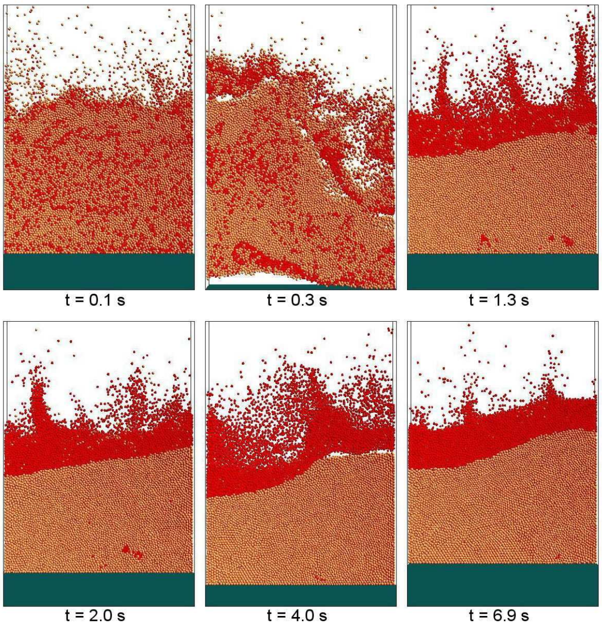

Figure 4.10: *A series of snapshots leading to the bronze-on-top structure (*$A_z = 0.9$ *mm,* $f_z = 55$ *Hz,* $\Gamma = 11$*) with low restitution coefficients. Bronze jets emerge from the bronze layer. These jets are formed by the increased energy dissipation in bronze-bronze collisions, caused by the low value of the normal restitution coefficient.*

We next consider the effect of the normal restitution coefficient. We first note that all the collision parameters used in the reference system were obtained via an experimental measurement technique as described in Kharaz *et al.* [14] for glass particles with a radius of 750 μm. Since the normal restitution coefficient depends - amongst other parameters - on the size of the particle, it is best to assume that the parameters used in this simulation are not extremely accurate. Additionally, we do not know the interaction parameters for bronze-glass and bronze-bronze collisions. However, we do expect that the normal restitution coefficient for bronze-bronze collisions is smaller than the one for glass-glass interactions since bronze is more easily deformed than glass. Since the precise value of the restitution coefficient is not known, we can only test the sensitivity of the results with respect to these collision parameters. We did a simulation for the bronze-on-top system in which we used extremely low restitution coefficients, while keeping the other parameters to the reference values. For the glass-glass interactions we used a normal restitution coefficient of 0.6, for the bronze-glass interactions a value of 0.4 and for the bronze-bronze interactions a value of 0.2. Note that the change in normal restitution coefficient requires a change in the value for the corresponding tangential spring stiffness (see Eq. 2.18).

Under atmospheric conditions at $f_z = 55$ Hz and $\Gamma = 11$, we find that the bronze moves to the top as in the reference system, where the purity of both phases is nearly perfect. Although tilting is observed, it is less frequent and no spilling of glass on top of the bronze layer is observed. Additionally, when bronze particles are launched from the top surface, bronze jets are formed, caused by the low normal restitution coefficient (see Fig. 4.10). When we do such a simulation for $f_z = 130$ Hz and $\Gamma = 10$, we see the regular formation of the sandwich.

For both cases, we also investigated the effect of having a high value for the normal restitution coefficient, namely 0.995. For these cases, we found similar results as for the 0.97 cases.

In conclusion, we find that the particle-particle and particle-wall collision parameters have a limited influence on the segregation phenomena, *except* for the friction coefficient for the sandwich system. In that case, the bronze layer may end up on top, in the middle, or even on the bottom, depending on the values of the parameters. The common values $\mu_{pp} = \mu_{pw} = 0.1$ derived for glass-glass interactions seem to correspond best with the experimental observations.

4.6.3 Effect of the box dimensions

We have studied the effect of different box dimensions and granular bed height on the two major segregation forms, namely the sandwich and the bronze-on-top formations. For the bronze-on-top section, we choose $f_z = 55$ Hz, $A_z = 0.9$ mm ($\Gamma = 11$) and for the sandwich section $f_z = 130$ Hz, $A_z = 0.147$ mm ($\Gamma = 10$). We used two different widths for the box (8.25 and 16.5 mm) and for each of these, three granular bed heights were tested (3.2, 6.5 and 9.7 mm). We found that the observations were the same as for the reference system for all combinations of box width and granular bed height.

As mentioned earlier, we also performed simulations for a 3D geometry (ground area 4.4×4.4 mm^2, granular bed height 6.5 mm, 105,600 particles), where the gas phase is now evaluated in all three dimensions and also for these cases did we find both the sandwich as well as the bronze-on-top structure. In Fig. 4.11, the sandwich formation for the 3D case is shown.

We next investigated the effect of the aspect ratio (width vs. height of the granular bed) on the behavior of the sandwich formation in more detail by increasing granular bed height from 6.5 mm to 19.5 mm, while keeping the width constant at the reference value of 8.25 mm. The aspect ratio was therefore increased from 0.8 for the reference system to 2.4. We found that for $f_z = 55$ Hz, $\Gamma = 11$, eventually the bronze-on-top configuration was formed, although the formation time is longer than in the reference system. For the sandwich configuration ($f_z = 125$ Hz, $\Gamma = 9$), we investigated two cases: (i) with and (ii) without wall friction on the principle cell faces. For both cases, we found a sandwich structure, although the final position of the bronze layer was different: the layer was located deeper below the granular bed surface for situation (ii).

In conclusion, we found that the occurrence of the bronze-on-top and sandwich structures did not depend much on the box width or granular bed depth. It must be remarked, however, that the final position of the bronze layer in the sand-

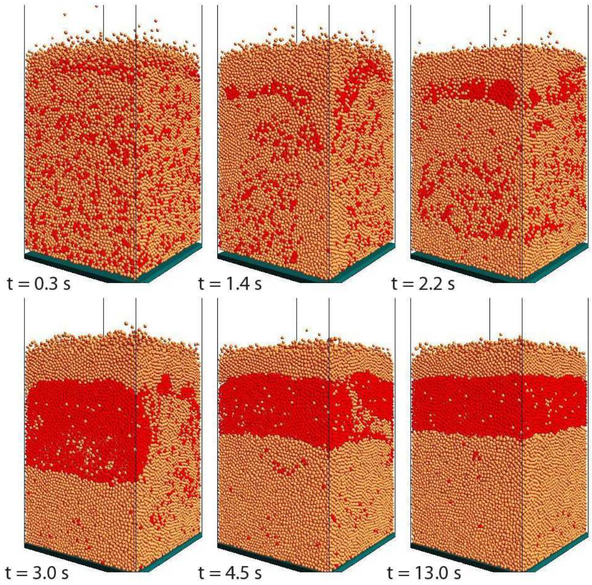

Figure 4.11: *A series of snapshots from a 3D simulation, leading to a sandwich structure* ($A_z = 0.147$ *mm*, $f_z = 130$ *Hz*, $\Gamma = 10$).

wich structure depended on the friction coefficients, as illustrated earlier in table 4.2.

4.6.4 Particle density ratio, initial situation and gravity

We studied the effect of the density ratio $\rho_{bronze}/\rho_{glass}$ with simulations for the standard bronze-on-top case ($f_z = 55$ Hz) and sandwich ($f_z = 130$ Hz) vibration parameters. Instead of using the density of glass (2525 kg/m^3), we used 1000 kg/m^3, thereby increasing the density ratio from 3.6 to 8.9. For bronze-on-top vibration conditions, we observed the regular tendency of the bronze moving to the top. However, the bronze does not easily remain on top, but exhibits tilting and forms a more sandwich-like structure. For $f_z = 130$ Hz, we observe the regular formation of the sandwich structure, but the time required to do so is much smaller (2 s compared to 10 s for the reference system). Apparently, for both the bronze-on-top as well as the sandwich system, the inertia in collisions of the bronze could explain these observations, since the reduction of mass means that the 'glass' layer underneath is less able to withstand the pounding of the bronze clusters on top.

We investigated the effect of the initial situation of the granular bed (mixed or segregated) on the segregation. A simulation at bronze-on-top conditions with an initial sandwich structure still resulted in a bronze-on-top structure. However, having a simulation at sandwich conditions with an initial bronze layer at top did not lead to the sandwich formation.

We then determined the dependence of the observed segregation phenomena for bronze-on-top and sandwich conditions on the presence of the gravity force. To this end, we deactivate the gravity in a box with a height of 0.016 m. The other simulation parameters are the same as in the reference situation. Since gravity is deactivated, the preferential direction of segregation can now be both upwards or downwards. Additionally, there is less mechanical energy input due to a smaller number of collisions with upper and lower system walls. For bronze-on-top conditions, we observe a number of bronze clusters meandering through the box. These clusters merge and break up continuously. The observed glass clusters are much larger. Like the bronze clusters, they are unstable and meander through the bed. Two porous sections with particles moving at high velocities (granular gas), are formed between the bottom and top.

4.6.5 Mixtures with 3 components

Up to now, in our reference system we have considered mixtures containing only 2 components, namely 7,500 bronze and 22,500 glass particles. We now consider a 3 component mixture, where in addition to the bronze ($\rho_s = 8900$ kg/m^3) and glass ($\rho_s = 2525$ kg/m^3), an additional component 'X' with a density of 6000 kg/m^3 is defined. The composition of the mixture was chosen as 5,000 bronze, 5,000 'X' and 20,000 glass particles. We investigated three sets of vibration parameters namely (i) $f_z = 55$ Hz, $\Gamma = 11$ (bronze-on-top), (ii) $f_z = 130$ Hz, $\Gamma = 10$ (sandwich), and (iii) $f_z = 75$ Hz, $\Gamma = 9$ (bronze-on-top), where the observation for reference conditions was placed in parenthesis.

For case (i), we found that both bronze and X went to the top and remained there in a mixed state. For case (ii), we found that initially bronze and X sink as in the regular sandwich formation process, however the final position was only just below the bed surface and therefore does not deserve the title of 'sandwich'.

Interestingly, for case (iii) we found that bronze and X went to the top as in case (i), but after this, separation continued so that eventually a bronze-X-glass structure was obtained. See Fig. 4.12. In contrast with case (i), bronze and X could separate and we suspect that this was caused by the less severe movement of the upper section of the granular bed.

We further investigated the absence of the sandwich in case (ii) by performing a simulation with a deeper granular bed (9.5 mm, compared to reference value of 6.5 mm). We changed the vibration parameters to ($f_z = 125$ Hz, $\Gamma = 9$) and also increased the relative amount of glass. The mixture consisted of 7,500 bronze, 7,500 'X' and 30,000 glass particles. We found that sinking of bronze and X was initiated, but again the particles remained too close to the granular bed for the structure to be called a sandwich. We suspect that the sandwich formation was hindered by the dilution of the bronze with the lower density component X.

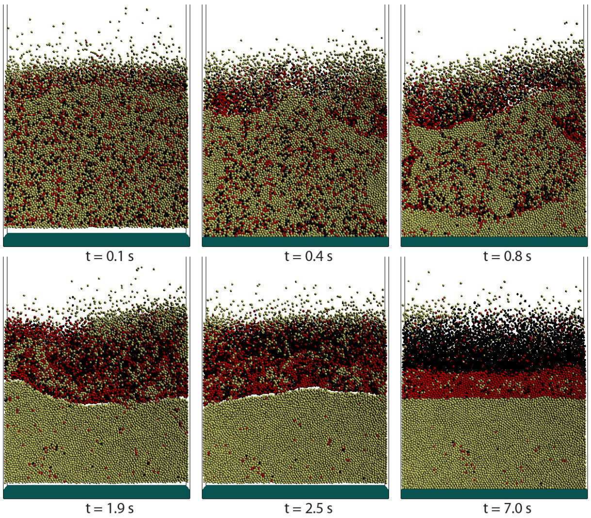

Figure 4.12: *A series of snapshots leading to the bronze-X-glass structure ($A_z = 0.4$ mm, $f_z = 75$ Hz, $\Gamma = 9$). Bronze and X move up together to the top. After this, they slowly segregate into separate layers.*

4.7 Conclusions

We have found that most of the phenomena that have been observed experimentally for vertically shaken beds of glass and bronze particles, are captured by our hybrid granular dynamics-computational fluid dynamics model. In particular, we found both the bronze-on-top and the sandwich structure for roughly the same shaking conditions as in the experiments, and also that these structures disappeared when the interaction of the particles with the air was switched off. Only the metastable regions, fluctuating between bronze-on-top and sandwich formations, are not observed. We suspect that this is mainly caused by the limited size of the system ($8.25 \times 0.65 \times 6.5$ mm) that we studied. We found that two distinct mechanisms are responsible for segregation. (i) For low vibration frequencies, the difference in acceleration from the gas drag causes the bronze to gradually move to the top, due to the pumping of air in combination with the cyclic compaction and decompaction of the bed. This effect appears to be very robust and relatively independent on the gas and particle properties that we studied. (ii) For higher vibration frequencies, the difference in inertial mass in collisions causes the bronze clusters on top to penetrate the glass-rich layer below in the second part of the cycle, when the falling bed is hitting the bottom plate. For lower frequencies and higher amplitudes, the first mechanism dominates due to the longer period of free flight, and bronze will always move to the top. For higher frequencies and lower amplitudes, the combination of mechanism (i) and (ii) leads to the sandwich formation.

The formation of the sandwich structure, however, appears to be a rather subtle process, and the state is much less robust. It has not been found in previous simulation studies, and we observed that it is rather sensitive on the particle properties; under the same shaking conditions, the bronze layer was found to end up in the middle (i.e., sandwich), on top *or* on the bottom, depending on the values for the friction coefficients. The state might not even be stable, as was already suggested from water-immersed experiments by Leaper *et al.*. Clearly the formation and stability conditions of the sandwich structure requires much further investigation.

Bibliography

[1] H.M. Jaeger, S.R. Nagel, R.P. Behringer, 'Granular solids, liquids, and gases', Rev. Mod. Phys. **68**, p. 1259 (1996).

[2] H.K. Pak, E. Van Doorn, R.P. Behringer, 'Effects of Ambient Gases on Granular Materials under Vertical Vibration', Phys. Rev. Lett. **74**, p. 4643 (1995).

[3] M.E. Möbius, B.E. Lauderdale, S.R. Nagel, H.M. Jaeger, 'Size separation of granular particles', Nature **414**, p. 270 (2001).

[4] N. Burtally, P.J. King, M.R. Swift, 'Spontaneous Air-Driven Separation in Vertically Vibrated Fine Granular Mixtures', Science **295**, p. 1877 (2002).

[5] N. Burtally, P.J. King, M.R. Swift, M. Leaper, 'Dynamical behaviour of fine granular glass/bronze mixtures under vertical vibration', Gran. Mat. **5**, p. 57 (2003).

[6] P. Biswas, P. Sánchez, M.R. Swift, P.J. King, 'Numerical Simulations of Air-driven Granular Separation', Phys. Rev. E **68**, 050301 (2003).

[7] M.A. van der Hoef, M. Ye, M. van Sint Annaland, A.T. Andrews IV, S. Sundaresan, J.A.M. Kuipers, 'Multi-scale modeling of gas-fluidized beds', Adv. Chem. Eng. **31**, p. 65 (2006).

[8] M.J.V. Goldschmidt, J.A.M. Kuipers, W.P.M. van Swaaij, 'Hydrodynamic modelling of dense gas-fluidised beds using the kinetic theory of granular flow: effect of coefficient of restitution on bed dynamics', Chem. Eng. Sci. **56**, p. 571 (2001).

[9] B. Thomas, A.M. Squires, 'Support for Faraday's View of Circulation in a Fine-Powder Chladni Heap', Phys. Rev. Lett. **81**, p. 574 (1998).

[10] M.A. Naylor, M.R. Swift, P.J. King, 'Air-driven Brazil nut effect', Phys. Rev. E **68**, 012301 (2003).

[11] M.C. Leaper, A.J. Smith, M.R. Swift, P.J. King, H.E. Webster, N.J. Miles, S.W. Kingman, 'The behaviour of water-immersed glass-bronze particulate systems under vertical vibration', Gran. Mat. **7**, p. 57 (2005).

[12] R.M. van der Meer, J.P. van der Weele, D. Lohse, 'Sudden Collapse of a Granular Cluster', Phys. Rev. Lett. **88**, 174302 (2002).

[13] J. Li, J.A.M. Kuipers, 'Flow structure formation and evolution in circulating gas-fluidized beds', China Particuology **2**, p. 1 (2004).

[14] A.H. Kharaz, D.A. Gorham, A.D. Salman, 'Accurate measurement of particle impact parameters', Meas. Sci. Techn. **10**, p. 31 (1999).

[15] R.J. Milburn, M.R. Swift, P.J. King, 'The effects of fluid-driven convection on the separation of binary mixtures', in 'Powders and Grains', Edited by Garcia-Rojo, Hermann and McNamara, p. 1029 (Taylor & Francis Group, London, 2005).

[16] M.E. Möbius, X. Cheng, G.S. Karczmar, S.R. Nagel, H.M. Jaeger, 'Intruders in the Dust: Air-Driven Granular Size Separation', Phys. Rev. Lett. **93**, 198001 (2004).

[17] M.E. Möbius, X. Cheng, P. Eshuis, G.S. Karczmar, S.R. Nagel, H.M. Jaeger, 'Effect of air on granular size separation in a vibrated granular bed', Phys. Rev. E **72**, 011304 (2005).

[18] C. Zeilstra, M.A. van der Hoef, J.A.M. Kuipers, 'Simulation study of air-induced segregation of equal-sized bronze and glass particles', Phys. Rev. E **74**, 010302 (2006).

5

Solids Circulation in Gas-vibro Fluidized beds

ABSTRACT

In this chapter, the effects of vibrations on the fluidization behavior of a granular bed are studied. After a short literature overview, describing the effects that vibrations may have on the (fluidization) behavior, we focus on the solids circulation rate and its dependence on the vibration parameters. An experimental study was performed in a pseudo-2D bed, and the optical measurement technique Particle Image Velocimetry was employed to obtain whole field velocity information. Additionally, computer simulations were performed and the time-averaged fields were compared. In both simulations and experiments, it was found that the solids circulation rate at constant f_z *increased with acceleration* Γ*, in agreement with experimental findings in literature; by contrast, no clear trend could be observed at constant* Γ *when the value of* f_z *was varied, which is somewhat surprising, since in the visual observations the bubble behavior was clearly affected. Gas-vibro fluidization generally exhibited larger circulation rates as compared to conventional gas-fluidization. When the simulations and experiments were compared quantitatively, it was observed that the circulation rate in the simulations was larger than in the corresponding experiment. From a limited parameter study, it was found that this may be caused by the particle-wall friction which is probably larger in the experiments than assumed in the simulations.*

5.1 Introduction

In a well-operated fluidized bed reactor, there is an intensive contact between the solids phase and the gas phase, so that heat and mass transfer rates can be maximized. Very fine particles, that is, A and C powders in the Geldart classification, have a high surface area per unit volume of the reactor, which makes them very attractive for processes involving gas/solid and solid/solid reactions. However, when the size of the particles in the powders becomes less than, say, 10 μm (C powders), the effect of the attractive forces between particles becomes relatively large and agglomerates can be formed. These agglomerates can cause the formation of stable channels and the fluidization behavior becomes poor since the gas will preferably flow through the channels. Similar problems can occur when sticky particles are used.

Fortunately, there are methods to overcome or avoid the formation of stable channels. One of these methods is the (vertical) vibration of the fluidized bed (gas-vibro fluidization), where the transfer of vibration energy into the granular assembly can diminish or even completely suppress channeling. Another method to destroy the channels is the use of pulsed gas-fluidization, on which we will elaborate later.

Gas-vibro fluidization knows many (potential) applications which are all related to enhancing the fluidization quality of difficult-to-fluidize particles. One can think of the drying of organic fine particles, or the removal of organic solvents from particles [4]. Also enhanced mixing of particles with different properties can be achieved, a typical example of which is the mixing of differently sized nano-particles for the preparation of nano-composites [22], but also granulation of small particles or the nitriding of steel [5]. The surface-coating (for example chemical vapor deposition) of small particles is also a potential application, especially for gas-fluidization under low pressures [10, 16]. Also, some chemical reactions have been carried out under gas-vibro conditions, such as methane oxidative coupling [6]. The reason for this is that most of the catalysts for this process contain alkaline or alkaline earth compounds, which were often found to melt under operating conditions, leading to agglomeration of the catalyst and potential de-fluidization. So, maintaining a properly fluidized bed is important in order to avoid formation of hot spots.

One of the most important industrial applications of gas-vibro fluidized beds is where they are employed as dryers of the plug flow type, where horizontal transport is imposed by a forward directed gas flow [28]. This equipment operates with a limited height of bed material (say 60 cm), and for this reason most research papers on this topic consider only shallow powder layers (usually smaller than 20 cm).

In this chapter, we will employ both experiments and numerical simulations to investigate the effect of the vibration on the solids circulation rate in gas-vibro fluidized beds. This quantity is an important index for heat transfer via the particle phase, and is strongly influenced by the bubble behavior. The experiments can give an indication as to how far the numerical model is able to predict the gas-vibro fluidization behavior.

Gas-vibro			Pulsed
Vertical	**Horizontal**	**Twist**	
[1–6], [10–12], [14] [19]*, [20–22] [23]*, [25], [29]*	[4], [11], [20]	[4], [7], [9], [11] [13], [15–17], [24]	[8], [18], [26,27]*

Table 5.1: *Overview of the literature discussed in this chapter. The references marked with an asterix are simulation studies.*

The chapter is organized as follows: we will first give an overview of experimental and simulation work in literature, where we will mainly focus on gas-vibro fluidization, only briefly touching upon the subject of pulsed gas-fluidization. We will shortly summarize advantages and disadvantages of gas-vibro fluidization and point out some remaining challenges. Next, we will describe the experimental setup and briefly discuss the measurement technique (PIV), where the reader is referred to Chapter 3 for a more elaborate coverage of the technique. Following this, we will discuss the simulation method, and more specifically the simulation parameters that we used. Finally, we will discuss the experimental observations and compare these with the model predictions, where we focus upon the solids circulation rates of a conventional gas-fluidized bed, and observe how these are affected by applying different vibration parameters.

5.2 Literature overview

5.2.1 General

Gas-vibro fluidized beds are conventional gas-fluidized beds to which mechanical vibrations are applied. When applied to cohesive or wet powders, it improves the quality of fluidization since the vibration reduces the formation of agglomerates. Usually, the vessel is vertically shaken using sinusoidal driving, where the vibration frequency (f_z) and amplitude (A_z) determine the strength of the vibration. A key parameter in vibrated granular beds is the ratio of the maximum acceleration of the bed to the acceleration from gravity:

$$\Gamma = \frac{A_z(2\pi f_z)^2}{g_z} \tag{5.1}$$

In literature, fluidized beds are most commonly vibrated in the vertical direction, but also vibrations in the horizontal plane have received attention [4, 11, 20]. Even ‘twist’ vibration - in which the object vibrates in multiple planes - has been applied [4, 7, 9, 11, 13, 15–17, 24]. A comprehensive overview with respect to the subjects of different papers is provided in table 5.1. There is currently some controversy about how the vibration energy is precisely transferred in gas-vibro fluidized beds. Some authors observe that the kinetic energy, gained by particles when colliding with the bottom plate, is lost in the lower sections of the granular bed due to the inelasticity of particle collisions, so that the vibrations have no significant effect on the behavior of particles located higher in the bed [2, 3, 14, 19, 21, 23]. Others argue that the vibrations induce pressure and gas velocity fluctuations and that this is the dominant energy transfer mechanism, where even particles that are far removed from the bottom plate may be affected [10, 12, 29].

Another way to induce a fluctuating force into a granular assembly is by the application of a periodically fluctuating gas flow, also called ‘pulsed gas-fluidization’. In recent experiments, Coppens *et al.* [18] found that pulsed gas-fluidization can result in ordering of bubble patterns, that is, the bubbles are rising in well-defined rows, staggered with respect to the previous one. Wang and Rhodes [26, 27] extended this work with their 2-dimensional DEM model and claim to have observed similar ordered bubble patterns. On the basis of other simulations with cohesive particles, they conclude that pulsed gas-fluidization could induce similar effects as the gas-vibro fluidized bed in cohesive powders, that is, suppression of stable channels. Wang and Rhodes further report that the benefits of pulsed gas-fluidization include reduced gas bypassing and gas channeling, thereby enhancing gas-particle contact in fluidized beds. Different types of pulsation can be applied: in one type, the gas pulsation involves alternatingly turning on and off the entire gas flow. As a consequence, however, the existence of an inactive phase can potentially lead to a decrease in heat transfer and additionally, the pulsation would be difficult to control, since the entire gas flow is varied.

Coppens *et al.* [18] chose a different approach, where the superficial gas velocity $u(t)$ is of the following form: $u(t) = u_0 + u_s \sin(\omega_z t)$ with u_0 the time-averaged superficial gas velocity, and u_s the amplitude of the flow oscillations. The advantages of this second type of pulsation are that (i) there is no inactive phase and (ii) the controllability of the gas flow is improved since only a part of the superficial gas velocity needs to be varied. For certain combinations of pulsation frequency and gas flow, Coppens *et al.* found that uniformly injected gas very quickly rearranged itself to form a regular row of bubbles, staggered with respect to the previous row. In their experiments with air and sand, the bubble patterns survived up to a height almost equal to the width of the granular bed. These interesting observations lead to believe that that chaotic movement of bubbles can be ordered using gas pulsation.

We finally note that a third type of pulsation was applied by Pence *et al.* [8], where the pulsation was induced by having a pulsating secondary air flow opposite to the (constant) fluidization flow.

5.2.2 Overview of literature results

In general, a bed is at minimum fluidization (mf) when the pressure drop over the packed bed is equal to the weight of the particles per area of the column, i.e., the gas-forces acting on the particles equal the gravitational forces. The gas velocity u$_{mf}$ at this condition can be determined either by slowly increasing the gas velocity (increasing gas velocity method) or by starting from a well-fluidized condition and slowly decreasing it (decreasing gas velocity method). As discussed before, cohesive or sticky powders are difficult to fluidize, so that in that case a lower pressure drop is expected. Usually, for such powders, the decreasing gas velocity method for determining u_{mf} is advised since the fluidized state provides an initial condition which is more reproducible compared to a settled bed [5, 7, 10, 24].

Under gas-vibro conditions, many researchers [1–3, 5, 7, 16], report a decrease of u_{mf} for gas-vibro fluidized beds, and this effect is commonly attributed to the increased packing fraction of the initial packed bed, since the applied vibrations lead to granular compaction. The pressure drop at these velocities is also lower, which means that the energy input from the gas phase is smaller than usual. Although not specifically mentioned in literature, this energy deficiency is balanced by the energy input via vibrations.

We now come to a short survey of the experimental findings. It has been suggested that gas-vibro fluidization under low pressures can be of interest for the purpose of coating very fine particles [7, 10, 16]. According to Wank *et al.* [10], atomic layer deposition - used for obtaining ultra-thin films - may require reduced pressure, and vibrations can assist in obtaining the fluidized state. Also, the drying of thermo-labile substances such as foods and pharmaceuticals can be done under reduced pressure, which allows the fluidized bed to operate at lower temperatures [16].

It has been reported by Yi *et al.* [12] and Mawatari *et al.* [13] that gas-vibro fluidization can increase the gas velocity window of homogeneous fluidization for Geldart A powders. They attribute this to the break-up of bubbles into the emulsion phase. Jin *et al.* [21] found that vibrations may even increase homogeneity for Geldart B and D powders.

Zhou *et al.* [20] investigated the bubble motion pattern and rise velocity in horizontally and vertically vibrated beds. For vertical vibrations, they found that all the bubble rise velocities are larger compared to those in the absence of vibration, although for frequencies larger than a certain threshold, no further increase of the rise velocity was observed. Mawatari *et al.* [25] investigated 60 μm glass beads under vertical vibration and performed experiments at a fixed frequency of 40 Hz, so that the vibration strength could only be modified via the vibration amplitude. They observed that when the vibration strength Γ was increased beyond a certain threshold value, the descending particle flow was enhanced, so that the area available for rising bubbles was reduced and coalescence of bubbles was promoted.

Vibrations need not to be limited to vertical vibration only, and horizontal vibrations or a combination of horizontal and vertical vibrations may also be used. Some researchers [4, 19] found a negative effect on the fluidization quality when only horizontal vibrations are applied in a gas-vibro fluidized bed, resulting in cracks between the side walls and the granular bed and gas bypassing. Mawatari *et al.* [11] and Mori *et al.* [4] found from their experiments that the application of horizontal components (which may be in combination with vertical vibration) was more effective for breaking channels in cohesive powders.

Finally, with respect to pulsed gas-fluidization, one of the key findings of DPM-type simulations by Wang and Rhodes [26, 27] was the formation of a large horizontal void structures near the vertically vibrated gas distributor [26], which was found to be in phase with the pulsation frequency. From this, it was argued that the pulsation frequency must not be chosen too small, in order to avoid the formation of large bubbles. It was further found that the form of the applied signal (square or sinusoidal) did not significantly influence the observations. A very interesting observation in their simulations was that pulsed gas-fluidization can break agglomerates, which is also observed in gas-vibro fluidization. However, experimental work is required to make a more definite conclusion on this subject.

5.2.3 Summary and Challenges

To summarize, the most important advantages of adding vibrations to gas-fluidized systems are: (i) Incipient fluidization at lower pressure drop and superficial gas velocities. (ii) Many fine and adhesive particles are completely fluidized under a low gas velocity: flow conditioners or mechanical stirring are not necessary to fluidize such systems [5]. Also, wet particles are more readily fluidized. (iii) Elutriation of fine particles is controllable since the fluidization behavior is not only governed by the gas-velocity, but also by the vibration parameters [4, 14]. (iv) The common advantages of gas-fluidized beds are still present [4]. Disadvantages included: (i) Energy costs of moving equipment. (ii) Attrition of granular material is possible due to collisions with the bottom plate.

Clearly, a number of challenges remain in understanding the effects of gas-vibro fluidization. Firstly, which energy transfer mechanism distributes the vibration energy into the granular bed? This could be via direct collisions, but it is expected that this mechanism becomes less important as the granular bed height is increased. Another mechanism could be the transfer via pulsations in the air velocity and subsequent pressure gradients. The question is at which bed height these effects dampen out, due to dissipation via the gas-particle drag. Secondly, what is the role of vibrations in widening the homogeneous fluidization window of Geldart A powders? Additionally, to what extent can homogeneity be improved for Geldart B/D particles? And finally, what are the effects of the vibration on the solids circulation rate, which is closely linked to the bubble behavior? In this research we focus on the last item. We finally note that the modeling of cohesive powders is usually done with much larger particles, since then a larger time step can be used when using a DPM method. In such a case, (artificially) larger cohesive forces are used in order to keep the Bond number (ratio of the attractive force and the gravitational force) constant. If the pulsation effects are important as an energy transfer mechanism, one could wonder if ratio between gas forces and cohesive forces is the same as in simulations with ‘real’ small particles or in experiments.

5.3 Experimental set-up and procedures

We performed gas-vibro fluidization experiments in a pseudo-2D gas-fluidized bed, which has dimensions of $15\times1.5\times60$ cm^3 (see Fig. 5.1 for a schematic

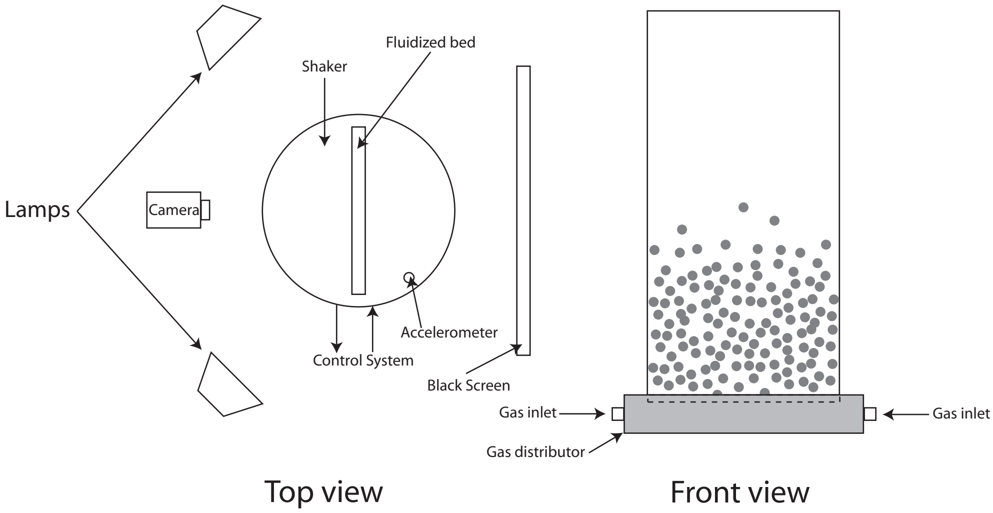

Figure 5.1: *Experimental set-up for gas-vibro fluidization. Two halogen lamps illuminate the box surface for the camera recordings, where a black screen is placed behind the set-up in order to provide contrast between the (light) particles and bubbles.*

overview). The principle cell faces consist of glass plates and the sidewalls are aluminum strips. The gas-distributor is attached to the base of the set-up, where an even gas distribution is achieved by using a sintered steel plate of thickness 2 mm with an average pore size of approximately 10 μm. For construction reasons, optical access to the lowest 6 mm of the bed, just above the gas distributor, was not possible. The entire construction was mounted on a shaker (Tira TV 50301), which can deliver a well-defined, sinusoidal driving, with a force up to 2700 N. An accelerometer (Endevco Isotron 751-100) measures the vibration characteristics and a control system ensures that the desired operating conditions are obtained. A high speed digital camera (LaVision Imager Pro) is positioned in front of the bed to record the images for PIV analysis, where two halogen lamps are used to illuminate the set-up. Air was used as fluidization gas, which was humidified by adding steam in order to reduce effects of static electricity. Due to this humidification procedure, it was difficult to keep the gas temperature at the ambient temperature values of 293 K: during the day temperatures could increase to 303 K, leading to an increase in the superficial gas velocity of approximately 3 %. However, it is expected that the effect on the observations is small, especially compared to the effects caused by the vertical vibrations.

We performed experiments with glass beads with a narrow size distribution, where the average diameter was 1.015 +/-0.02 mm and the height of the settled granular bed was 15 cm. We determined the minimum fluidization velocity (u_{mf}) of these particles and found it to be 0.65 m/s. In the experiments, we used a superficial gas velocity of 1.5 × u_{mf} (i.e., 0.98 m/s). The measurement procedure was as

Γ	$\mathbf{f_z}$	$\mathbf{A_z}$	$\mathbf{V_b}$
0.5	5	$4.97.10^{-3}$	1.58
0.5	7.5	$2.21.10^{-3}$	1.05
0.5	10	$1.24.10^{-3}$	0.79
1	6	$6.90.10^{-3}$	2.63
1	7.5	$4.42.10^{-3}$	2.10
1	10	$2.49.10^{-3}$	1.58
1	12.5	$1.59.10^{-3}$	1.26
2	7.5	$8.84.10^{-3}$	4.20
2	10	$4.97.10^{-3}$	3.15
2	12.5	$3.18.10^{-3}$	2.52
2	15	$2.21.10^{-3}$	2.10
5	12.5	$7.95.10^{-3}$	6.31
5	15	$5.52.10^{-3}$	5.25
5	17.5	$4.06.10^{-3}$	4.50
5	20	$3.11.10^{-3}$	3.94

Table 5.2: *Vibration parameters of the experiments and simulations. Here, f_z and A_z are the vibration frequency [s^{-1}] and amplitude [m], respectively. V_b is the velocity amplitude [-], defined as* $V_b = \frac{A_z \omega_z}{\sqrt{g_z d_p}}$.

follows. Once the system was set into vibration at the desired shaking parameters, we let the fluidized bed initialize at working conditions for 2 minutes, after which the measurements were performed. These measurements consist of recording image pairs with the high speed digital camera, which allows for the measurement of the instantaneous velocity fields (more details on this in the next section). For the camera settings that we used, the maximum duration of the measurements was 2 minutes.

We investigated 4 different values for the acceleration (Γ), where the vibration parameters are displayed in table 5.2. There were certain limitations for the vibration parameters, since the maximum amplitude of the shaker was 10 mm. Additionally, from preliminary experiments it had become clear that small variations in the vibration frequency could lead to different bubble behavior. Therefore, we chose to increase the vibration frequency only in small steps of 2.5 Hz.

5.4 Particle Image Velocimetry

The high speed digital camera was triggered using an external, programmable, wave form generator (Velleman Instruments PCG10/8016) so that it could operate in so-called PIV (Particle Image Velocimetry) mode. Essentially, the camera records 2 consecutive images with a very small delay (in our case 3.33 ms) and we recorded 7 images pairs per second, for a duration of 2 minutes, which results in a total of 840 image pairs.

We obtained the instantaneous particle velocity fields from the image pairs by software analysis using the PIV software DaVis. The principles of PIV analysis can be found in Chapter 3. Since the camera has a fixed position with respect to the vibrated box, care must be taken in the selection of the vectors to be included in the time averaging. In order to avoid artifacts resulting from PIV analysis of the box itself, we only use the vectors at positions where the vibrating walls are never present.

5.5 Simulation method

The simulation method is described in detail in Chapter 2, where a model is presented for the inclusion of vibrations in conventional gas-fluidized beds, using the discrete particle model with unresolved gas-particle interaction. A disadvantage of the method is that the code can become instable if there is nearly no gas left in the cells. Usually, adapting the grid size in the z-direction can alleviate this problem. In our simulations, the size in the x-direction of the CFD cells was 3 mm, the size in the y-direction was 6.09 mm and the size in the z-direction was 4 mm. For a few cases, it was found that a 5 mm grid spacing in z-direction was more stable. Note that we used a smaller column depth in the simulations as compared to the experiments, in order to minimize the number of particles and thus computational time. Even by doing this, the simulations still required 156,000 particles. To test the effect of the column depth, we performed a simulation where we used a depth of 1.5 cm - as in the experiments - which increased the amount of particles to 390,000. For the latter simulation, we used a parallelized version of the code, calculating on four CPU's. For the case with the smaller amount of particles, we used a single CPU.

It was computationally not feasible to run simulations for 2 minutes realtime, as in the experiments; instead, we increased the output data rate in the simulations to 25 Hz (in the experiments it was 7 Hz). We ran the simulations for 20 seconds, discarding the initial 4 seconds to avoid possible start up effects.

The particles in the simulation had the same size distribution as in the experiments. For the description of the collisions, we used a normal and tangential restitution coefficient of 0.97 and 0.33, respectively, both for the particle-particle and the particle-wall interactions. For the Coulomb friction coefficients (μ_{pp} and μ_{pw}) we used a value of 0.10. As described in Chapter 4, it was found in a previous simulation study that these values were the most realistic ones for 1.5 mm glass spheres. For the normal and tangential spring stiffness (k_n and k_t), we used values of 2500 N/m and 803 N/m, respectively and a time step DT of $2.5.10^{-5}$ s was used for solving the gas flow field, while the time step to integrate the equation of motion for each particle was 5.10^{-6} s. As is customary, we also investigated the effect of doubling the values of the spring stiffnesses to 5000 N/m and 1606 N/m, respectively. From the RMS analysis (measure for circulation rate) for conventional gas-fluidization we found an slight increase of the circulation rate with approximately 6 %, which we found acceptable. From the simulations, velocity fields were generated at fixed intervals in time.

An advantage of simulations is that all microscopic data - which is difficult or impossible to measure experimentally - is readily available. This allows us to calculate, apart from the velocity field, also the *flux* field, from the instantaneous local particle *flux* $\mathbf{f_i} = \varepsilon_s \cdot \mathbf{v_i}$, with ε_s the packing fraction and $\mathbf{v_i}$ the average local particle velocity. Note that in our experimental set-up, it was difficult to measure the instantaneous local packing fraction experimentally.

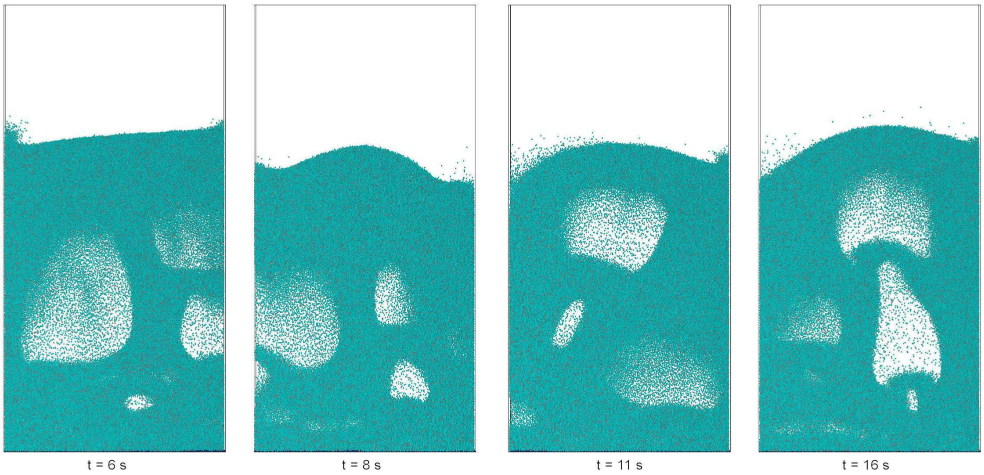

Figure 5.2: *Snapshots of a simulation of conventional gas-fluidization (no vibrations) at 1.5* u_{mf} *(*$u_{mf} = 0.65$ *m/s).*

5.6 Results and discussion

This section is organized as follows. First, we will present the visual observations in the simulations and experiments. Then, we will discuss the analysis of the obtained velocity fields, where the main goal is to obtain a measure of the circulation rate. After that, we investigate trends in the solids circulation rate of the simulations as a function of the vibration parameters and finally, we discuss the trends in the experiments and compare with those observed in the corresponding simulations.

5.6.1 Visual observations

We prepared animations of the simulation results for visual inspection. However, since it is impossible to estimate the solids circulation rates from the animations, we primarily focused on the bubble behavior in the gas-vibro fluidized bed for different frequencies at constant Γ and compared with those of a conventional gas-fluidized bed with no vibrations (see Fig. 5.2). At $\Gamma = 0.5$, we observed that bubble formation was suppressed for $f_z = 5$ Hz, and that large bubbles rose in the center of the bed. For $f_z = 7.5$ Hz and $f_z = 10$ Hz, this was less the case and bubbles can more often seen to rise simultaneously from different locations in the bed. At $\Gamma = 1.0$, we observe a larger gap between the bottom of the granular bed and the vibrating plate for all frequencies, where for $f_z = 6$ Hz and $f_z = 7.5$ Hz we observe the formation of ‘arches’, that is, curvatures at the bottom of the solids bed (see Fig. 5.3). The arches are also observed in the experiments (see Fig. 5.4). At these frequencies, the (predominantly large) bubbles rise through the center region although the horizontal location is constantly changing and the formation of smaller

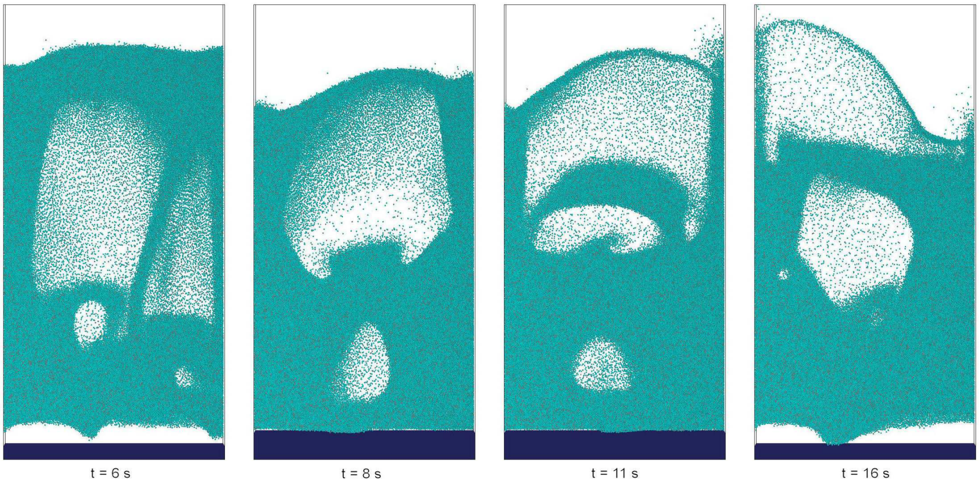

Figure 5.3: *Simulation of gas-vibro fluidization, where* $f_z = 7.5$ *Hz and* $\Gamma = 2.0$. *Note the arches at the bottom of the bed.*

bubbles is suppressed. For larger values of f_z, the effect was smaller. At $\Gamma = 2.0$, we observe similar behavior as at $\Gamma = 1.0$, namely the arching and bubble suppression at low frequencies and a decline of the effect with increasing f_z. $\Gamma = 5.0$ is not different in this respect, where in all investigated cases bubble formation was suppressed and (predominantly large) bubbles rise through the bed. Again, the arching behavior became less pronounced as f_z increased. It seemed that the bubble behavior is most strongly affected at low values of f_z and large values for A_z. All these observations were corroborated by the experiments.

Solids circulation rates in gas-fluidized beds are usually dominated by the behavior of the gas bubbles: a bubble pushes away granular material and in its wake, particles are sucked upward. A striking example is the circulation pattern in spout-fluidized beds [30], where the central jet dominates the solids flow pattern. In our experiments, we observed the formation of bubble trains for the following combination of vibration parameters: (f_z, Γ) is (6, 1.0), (7.5, 2.0), (10, 2.0), (12.5, 5.0) and (15, 5.0). These trains were reminiscent of spout fluidization. However, they were instable, could meander through the bed and were found at large values of A_z.

5.6.2 Data treatment

The analysis of the vector data obtained from the simulations - where the prime goal is to get a measure of the solids circulation rate - was performed using two methods: (i) root mean square (RMS) analysis of the time-averaged field and (ii) cumulative histograms. We used both methods since the histograms alone were not as clear as those in Chapter 3, since the range of particle velocities was much smaller for gas-vibro fluidized beds than for the vibrated beds. It is stressed that

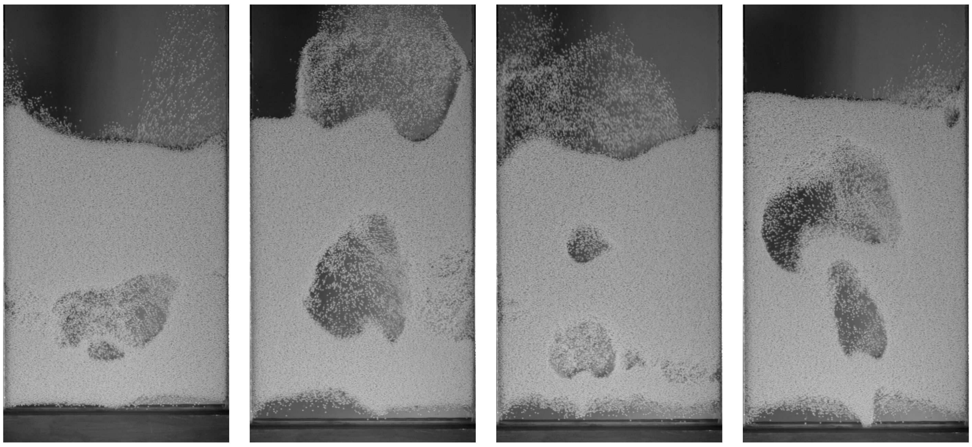

Figure 5.4: *Experiment of gas-vibro fluidization, where* $f_z = 7.5$ *Hz and* $\Gamma = 2.0$. *Note the arches at the bottom of the bed.*

the *spatial* RMS value of a time-averaged velocity field is used as a measure of the circulation rate. This in contrast to a *temporal* RMS value, which is a statistical measure of the magnitude of a varying quantity.

The RMS value of N vectors lengths in a time-averaged (flux or velocity) field is defined as:

$$\sqrt{\frac{\sum_{i=1}^{N}(\mathbf{v_i} \cdot \mathbf{v_i})}{N}} \tag{5.2}$$

with N the number of vectors and $\mathbf{v_i}$ the velocity vector. The calculated RMS data for the simulations as well as the experiments can be found in Appendices A and B, and we will discuss trends in these RMS values later. The question that first arises is which kind of vectors are to be compared: the particle *velocity* $\mathbf{v}$, or the particle *flux* $\mathbf{f} = \varepsilon_s \cdot \mathbf{v}$? When performing PIV, the software determines the local particle velocity, but does not specify the amount of particles represented by that velocity. In regular PIV, one usually works with a fluid, which has a constant density. In gas-fluidized beds, however, the local packing fraction (and thus the 'fluid' density) fluctuates strongly due to gas bubbles passing by, so that trends predicted by the velocity may be different from those predicted by the flux. Unfortunately, in contrast to the simulations, determining the time-averaged particle fluxes experimentally is non-trivial, since we cannot accurately measure the packing fraction. In earlier work, performed by Link *et al.* [31], a packing fraction was estimated in a pseudo-2D bed by analyzing the PIV recordings with a particle detection algorithm, but this could only be done accurately when the particle diameter (expressed in pixels) was sufficiently large (around 10 pixels) and the contrast between particles and background was high, allowing for accurate distinction of the boundary between the two. In this experimental work, the particle diameter is smaller (around 5 pixels) and the contrast is lower since the particles were partially translucent, so that we are limited to comparing the time-averaged velocity fields.

In order to draw meaningful conclusions from the time-averaged velocity fields of the experiments, we need to demonstrate that trends in circulation rate are similar, whether we study particle velocities or fluxes. This was tested in the simulations, where the local packing fraction ε_s (and thus the particle flux) is readily available and we found that the choice for either one did not affect the trends that we observed.

We performed simulations of 20 s realtime, where the initial 4 s were discarded to eliminate start-up effects. In the remaining 16 s, we collected the velocities and positions of all particles at a rate of 25 Hz so that we obtain a total of 400 data sets. Note that for the particle velocity averaging in the simulations, we used the entire particle bed, whereas in the experiments only the particles at the principle cell faces are visible and can be analyzed. Therefore, in order to investigate possible wall effects in the simulations, we also determined the average particle fluxes caused exclusively by the particles present within 2 mm (corresponding to 2 d_p) from the principle cell faces. For the value of the particle-wall friction that we used ($\mu_{pw} = 0.10$, which is typical for glass), we found the same results for the averages as when using the entire particle bed. We therefore conclude that - in our simulations - no velocity gradients exist within the depth of the bed. Based on this, we assume that the PIV measurements of particles at the principle cell faces describe the entire pseudo-2D bed behavior.

We investigated if the simulated time was sufficient for obtaining a converged average vector field. An example of a time series is shown in Fig. 5.5, where the vibration frequency was 15 Hz ($\Gamma = 2.0$). We used a cumulative histogram to assess if the time-averaged flux or velocity fields have become stable, and to compare the circulation rate with simulations for other vibration parameters and the case of no vibration. The choice of the height of the area of interest for the evaluation is rather arbitrary, however. We compared the results from analyzed areas up to 19 cm and up to 24 cm, where the difference is the amount of freeboard taken into account (e.g., see Fig. 5.5). In the experiments we performed an extra analysis for up to 16 cm. At all times, we excluded the region where the bottom is moving: for example, if the amplitude of vibration is 0.5 cm, the lower boundary for analysis is $2\times0.5 = 1$ cm and the upper boundary 20 cm. We found that the choice of area did not affect the observed trends in the circulation rate.

The flux and velocity histogram data for the cases of Fig. 5.5 can be found in Appendix C. It shows that the distribution of the particle flux and velocity in the gas-vibro fluidized bed becomes stable after t = 16.0 s, which we also observed in the other simulations that we performed.

5.6.3 Trends from simulations

We will now study the effects of vibration on the solids circulation rate on the basis of the RMS data from Appendix A. As mentioned earlier, we also studied trends using cumulative histograms of which a sample is given in Fig. 5.6. Since similar

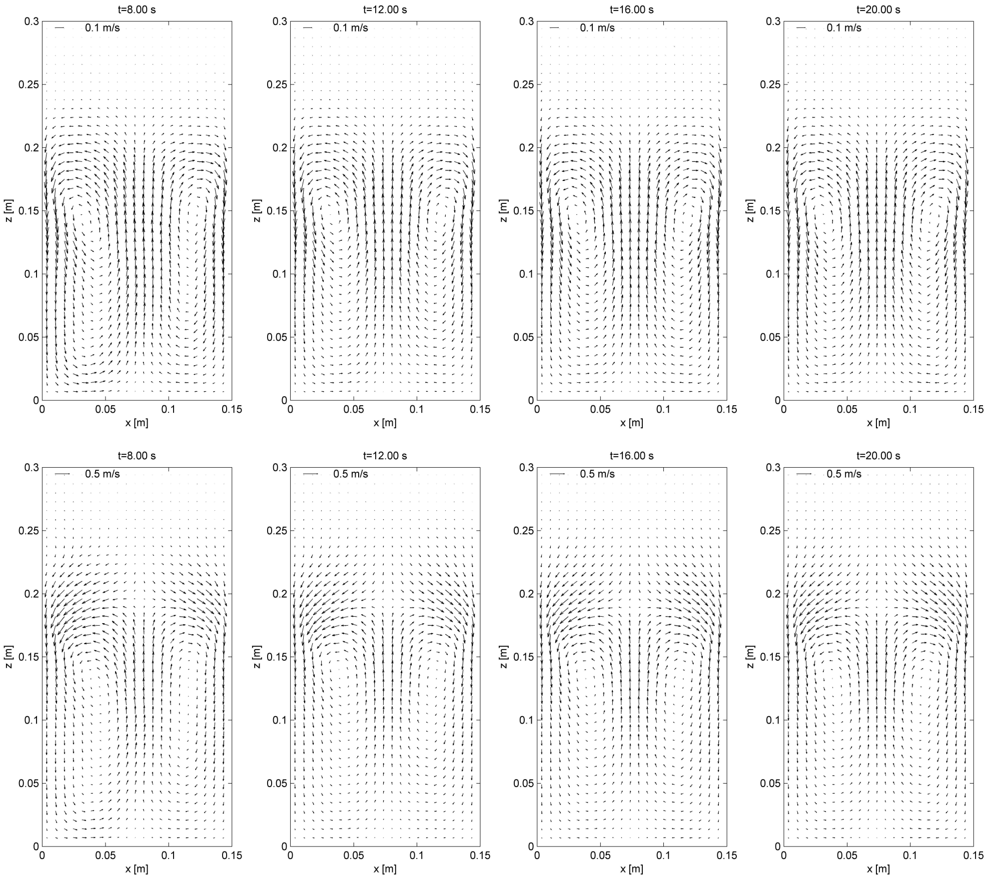

Figure 5.5: *Simulation results for a granular bed vibrated at 15 Hz ($\Gamma = 2.0$), simultaneously gas-fluidized at 1.5 u_{mf} (0.98 m/s). The time-averaged particle flux and the time-averaged velocity field are displayed on the upper and lower rows, respectively. The averages were taken from t = 4.0-20.0 s. Each vector represents the average of an area of 7×7 mm^2, where the overlap between areas was 50 %. For the sake of clarity, we have plotted only one out of every 4 vectors. From t = 16.0 s, there are no significant changes in both series. This can be better observed in the cumulative histograms, which are found in Fig. 5.12 (Appendix C). Note that the velocity vectors in the freeboard of the bed (above 0.19 cm) in the graphs on the second row are predominantly oriented in the negative z-direction. This in contrast to the graphs in the first row, where the variation of the fluxes is smooth.*

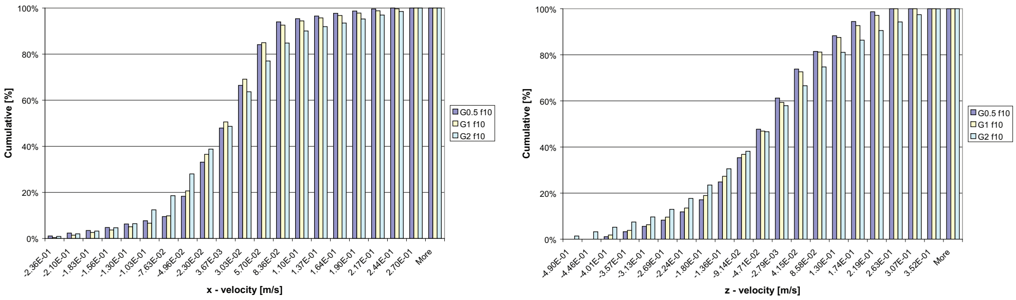

Figure 5.6: *Cumulative histogram for the x- and z-velocity for the simulations performed with a constant vibration frequency of $f_z = 10$, simultaneously gas fluidized at 1.5 u_{mf} (0.98 m/s). The figure demonstrates the trends for increasing Γ at constant f_z, namely that the velocity range and the circulation strength increase with Γ.*

trends were observed, we will base our discussion on the RMS values. We investigated three cases, namely at constant acceleration Γ [-], at constant vibration frequency f_z [s^{-1}], and at constant vibration amplitude A_z [m]. We will start with the analysis for constant acceleration Γ, using either $\Gamma = 0.5$, 1.0, 2.0 or 5.0. As a reference, the data for conventional gas-fluidization without vibration is also shown. See tables 5.3 and 5.4 in Appendix A for the RMS data.

At $\Gamma = 0.5$, we find that the circulation rates are slightly increased as compared to conventional gas-fluidization, and even more so at $\Gamma = 1.0$. However, there is not a clear trend in the circulation rates when we increase f_z. Also at $\Gamma = 2.0$, all the cases display stronger circulation rates compared to conventional gas-fluidization, and we also observe that they decrease in strength with increasing f_z (i.e., decreasing vibration amplitude), except for $f_z = 7.5$ Hz and $f_z = 10$ Hz which are similar. Finally, at $\Gamma = 5.0$ all cases display stronger circulation rates, but they are hardly affected by the vibration frequency.

We next investigate the effect of increasing the acceleration (Γ) at constant f_z, effectively increasing the vibration amplitude. As follows from table 5.2, there are a limited amount of vibration frequencies that were tested with more than two values at Γ. These are $f_z = 7.5$ Hz, $f_z = 10$ Hz and $f_z = 12.5$ Hz. See Fig. 5.7. In all the series, we found - both for particle flux as well as velocity histograms - that the circulation rates increased with increasing acceleration. We continue with the analysis of a batch at constant value of A_z. As can be seen in table 5.2, we allowed for a small variation in the chosen amplitude. See Fig. 5.8. We first tested at $A_z \sim 2.2$ mm, with (f_z, Γ) is (7.5, 0.5), (10, 1.0) and (15, 2.0). It was found that increasing the frequency (and thus the acceleration) leads to a larger circulation rate. The effect is also found for $A_z \sim 5$ mm, where we used (f_z, Γ) is (5, 0.5), (7.5, 1.0), (10, 2.0) and (15, 5.0).

We next investigate the effect of some assumptions and simplifications that we made in the simulated system, namely the effect of the particle-wall friction coeffi-

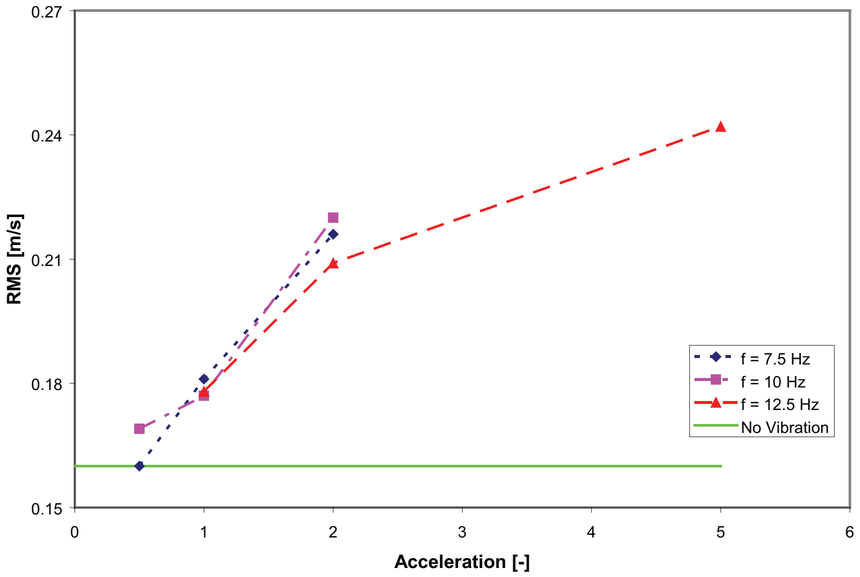

Figure 5.7: *RMS values [m/s] of the velocity fields of the simulations, obtained from an analyzed area with a height of 19 cm, which excludes most of the freeboard. The figure shows that for constant f_z, the circulation rate increases with the acceleration Γ.*

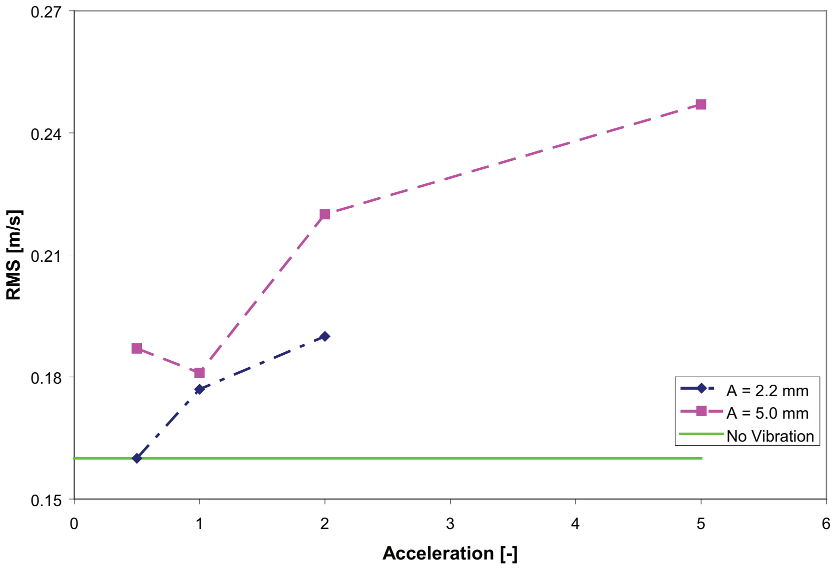

Figure 5.8: *As in Fig. 5.7, but now for different values of A_z.*

cient (μ_{pw}) and the box depth. In order to investigate the effect of μ_{pw} on the circulation rate, we increase the value from the standard value of 0.1 to 0.3 for two cases, namely one at conventional gas-fluidization and one at gas-vibro fluidization conditions: $f_z = 10$ Hz ($\Gamma = 2.0$). For both cases, it was found that the circulation rate was strongly reduced: for the flux at conventional gas-fluidization we now found a RMS value of $4.49.10^{-2}$ m/s (was $7.36.10^{-2}$ m/s) and for the gas-vibro fluidization case we found a value of $5.01.10^{-2}$ m/s (was $1.06.10^{-1}$ m/s). These observations were also made if choosing a larger area of analysis or when studying particle velocities instead of fluxes. The observation that μ_{pw} can have such a profound effect on the observed solids circulation rate makes it clear that a quantitative comparison with the experiments will become difficult, as we did not measure μ_{pw} experimentally, but instead used the value of 0.1.

In order to test what effect the box size has on the results, we performed a simulation with a depth comparable to what is used experimentally, namely 15 particle diameters instead of the 6 used in the regular simulations. Since the number of particles increases from 156,000 to 390,000 we used a version of the code in which the particle collision section was parallelized. Although the computational efficiency was low (approximately 50 %), it allowed us to perform such simulations within a reasonable time frame. For the tested case ($f_z = 7.5$ Hz, $\Gamma = 2.0$), we find that the circulation rate is stronger when we simulate the larger box (flux 0.131 m/s, velocity 0.276 m/s) compared to the smaller box (flux 0.103 m/s, velocity 0.216 m/s): apparently the simulations with depth of 6 particle diameters suffer from a finite size effect. Although this limits the quantitative comparison of the circulation rate, we expect that a qualitative analysis can still be performed.

5.6.4 Trends from experiments

We performed experiments to verify the trends observed in the simulations. We found that analysis of PIV data obtained at 7 Hz for 2 minutes was enough to obtain a (constant) time-averaged velocity field, see Appendix C. We did not further analyze cumulative histograms for the experiments. Instead, we analyzed the RMS data, which can be found in Appendix B. Some examples of time-averaged velocity fields can be found in Fig. 5.9, where we show results for conventional gas-fluidization and two gas-vibro fluidization cases. As mentioned earlier, for each combination of f_z and Γ we performed three experiments, where we used the averaged RMS value to investigate trends. It must be mentioned that it was difficult to obtain symmetric circulation patterns under vertical vibrations, since a very slight tilting could already disturb the time-averaged result, introducing a-symmetry.

As in the simulations, we investigate the trends (i) at constant Γ, (ii) at constant f_z and (iii) at constant A_z. We analyzed three areas, with heights of 16, 19 and 24 cm, where the difference is the amount of freeboard taken into account. In the RMS values for the different analyzed areas, it was found that the excessive downward pointing vectors above the level of $h = 19$ cm (see Fig. 5.9) had a strong effect on the observed trends. We therefore analyzed only the area from $h = 3$ to $h = 19$ cm (analyzed area of height 16 cm), since the velocities in the freeboard are large but

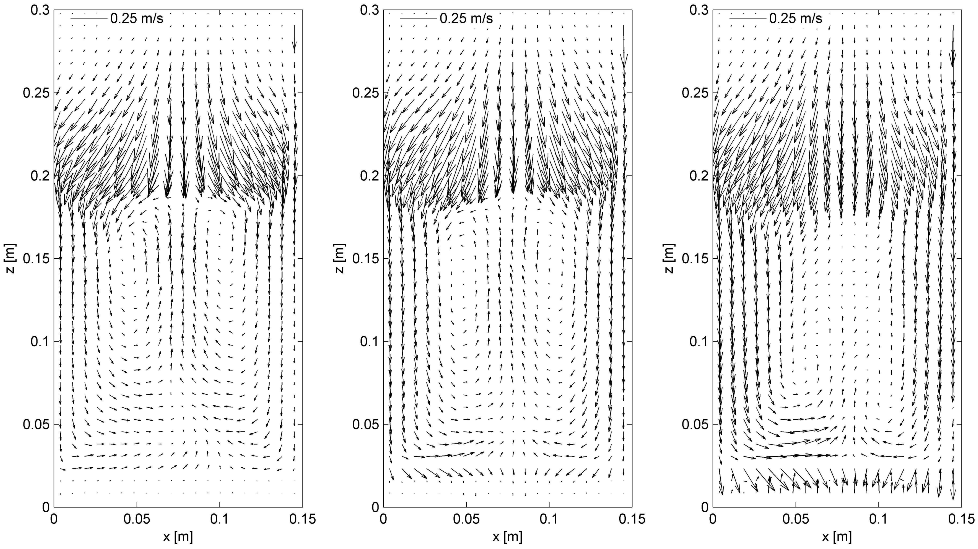

Figure 5.9: *Time-averaged velocity fields for three different experiments. From left to right: (i) conventional gas-fluidization, (ii) gas-vibro fluidization, with* $\Gamma = 1.0$ *(*$f_z = 10$ *Hz) and (iii) gas-vibro fluidization, with* $\Gamma = 2.0$ *(*$f_z = 10$ *Hz). As can be seen, the circulation rate increases with* Γ*, reflected in the increasingly large velocity vectors. However, for the case of* $\Gamma = 2.0$ *the upward velocity vectors in the center are very small, which was observed also for some other experiments. The reason for these very small velocities is not clear. However, since we did not observe such phenomenon in the simulations, it may either be caused by the measurement method or a true feature of the experimental system itself. The effect of this phenomenon is that the RMS value of such experiments is somewhat underestimated. However, since the affected region is relatively small, there are no significant changes in the RMS that changed the trends that we observed.*

less important since they represent only a small number of particles.

For the analysis at constant Γ (table 5.5 in Appendix B), we do not observe consistent trends for increasing f_z. For $\Gamma = 0.5$, we see the strongest circulation at $f_z = 5$ Hz, while for larger values it seems approximately constant. For $\Gamma = 1.0$, $\Gamma = 2.0$ and $\Gamma = 5.0$ it appears that the circulation rate decreases with increasing f_z. However, all cases exhibit a stronger circulation than conventional gas-fluidization, which we also observed in the simulations.

We next investigate the effect of increasing Γ at constant f_z, effectively increasing the vibration amplitude. The results are summarized in Fig. 5.10 and confirm the findings in the simulations, namely that at constant f_z, the circulation rate increases with increasing Γ. Finally, in Fig. 5.11 we show the results for a constant vibration amplitude ($A_z \sim 2.2$ and 5.0 mm). No clear trends can be observed for this case.

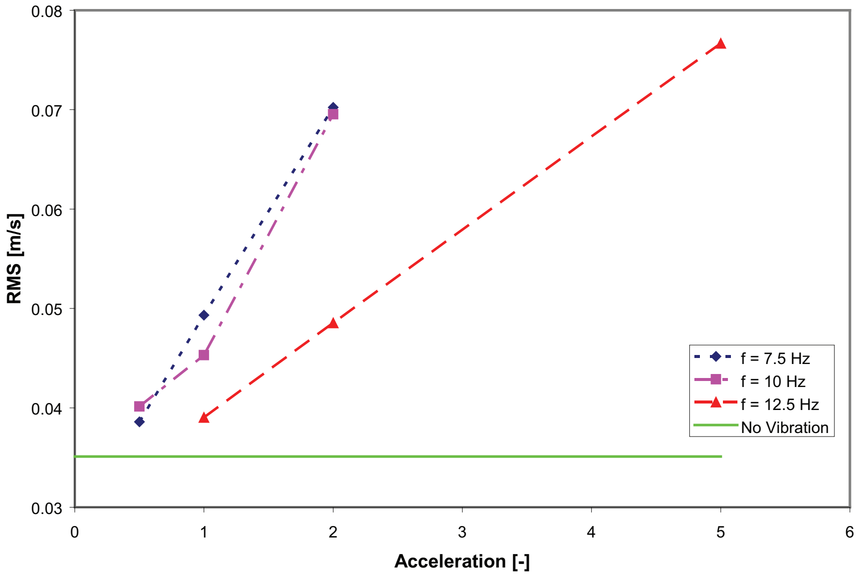

Figure 5.10: *RMS values [m/s] of the velocity fields of the experiments. We used the values obtained using an analyzed area of height 16 cm, which excludes most of the freeboard. The figure shows that for constant f_z, the circulation rate increases with the acceleration Γ.*

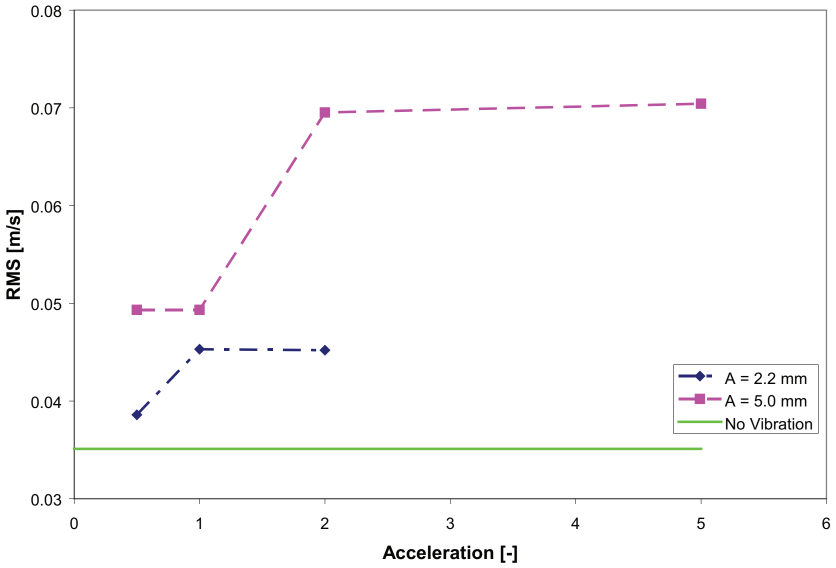

Figure 5.11: *As in Fig. 5.10, but now for different values of the A_z.*

5.7 Conclusions

In this chapter we have investigated the effect of vertical vibrations on the solids circulation in a pseudo-2D fluidized bed of 1.0 mm glass particles, fluidized at 1.5 u_{mf}. We compared visual observations from the discrete particle model with experiments and found similar behavior. Also, it was clear that the bubble behavior could be very different from conventional gas-fluidization, depending on the vibration parameters. Generally, we observed that the vibrations reduced bubble formation, leading to fewer, but larger bubbles. This was especially true for vibrations with larger amplitude (A_z), where a behavior reminiscent of that of a spout-fluidized bed could be observed. It is known that the bubble behavior can have a profound effect on the solids circulation, which we therefore investigated further.

We quantified the solids circulation in the simulations and experiments by means of the spatial root mean square (RMS) values. In both simulations and experiments we found that the dimensionless acceleration Γ was of key importance for the circulation rate: it increased with increasing Γ at constant f_z and this seemed also to be the case at constant A_z, although it was less pronounced. This finding agrees with Mawatari *et al.* [25] who found that the downflow of particles at constant f_z increased with Γ. We further found that at a constant level of Γ, there was no clear trend when the value of f_z was changed. This was somewhat surprising since from visual observation, it followed that the bubble behavior was affected. The RMS data further showed that both in the simulations as well as the experiments, the gas-vibro cases displayed a larger circulation rate as compared to conventional gas-fluidization. Based on the above observations, one can speculate on the effect on the circulation rate of increasing f_z beyond the values in this study. It is expected that above a certain threshold value of f_z, the circulation rate will not be further affected, mainly because the time scale of the gas velocity fluctuations will be too fast to significantly influence the dynamics of the particles.

It was found in the simulations that the particle-wall friction can have a profound effect on the observed circulation rate which makes a quantitative comparison between simulation and experiment difficult. Also, the effect of the reducing the box depth in the simulations was found to be of influence on the results. We further found that the circulation rate in the simulations was larger than in the corresponding experiments. From a limited parameter study in the simulations, we observed that this may be caused by a larger value of the wall friction in the experiments than assumed in the simulations.

In future experimental work, the focus should be on the accurate determination of the packing fraction so that fluxes can be compared. Additionally, experimental measurement of the bubble behavior under vibration may be further investigated by using a pressure probe, in order to determine the dominant bubble frequencies. In this light it would also be of interest to investigate the effect of increasing the particle bed height to study the effect of vibrations higher up in the granular bed, or the effect of having a wider set-up so that multiple circulation cells may develop.

Appendix A: RMS data of simulations

In this appendix, the RMS data of the performed simulations can be found, both expressed in fluxes (table 5.3) as well as velocities (table 5.4). The data shows that the RMS values for the time-averaged velocity fields are always larger than those for the corresponding flux fields, which is due to the effect of the packing fraction (ε_s). For both the fluxes as well as the velocities, no clear trends in RMS value could be observed when increasing f_z at constant Γ.

$f_z \downarrow \Gamma \rightarrow$	0.5	1.0	2.0	5.0
None	$7.36.10^{-2}$	$7.36.10^{-2}$	$7.36.10^{-2}$	$7.36.10^{-2}$
5.0	$9.07.10^{-2}$			
6.0		$8.59.10^{-2}$		
7.5	$7.63.10^{-2}$	$8.77.10^{-2}$	$1.03.10^{-1}$	
10.0	$8.16.10^{-2}$	$8.63.10^{-2}$	$1.06.10^{-1}$	
12.5		$8.42.10^{-2}$	$9.73.10^{-2}$	$1.20.10^{-1}$
15.0			$8.93.10^{-2}$	$1.20.10^{-1}$
17.5				$1.18.10^{-1}$
20.0				$1.24.10^{-1}$

Table 5.3: *RMS values [m/s] of all vector lengths in the time-averaged flux fields of the simulations. The investigated area had a height of 19 cm.*

$f_z \downarrow \Gamma \rightarrow$	0.5	1.0	2.0	5.0
None	$1.60.10^{-1}$	$1.60.10^{-1}$	$1.60.10^{-1}$	$1.60.10^{-1}$
5.0	$1.87.10^{-1}$			
6.0		$1.80.10^{-1}$		
7.5	$1.60.10^{-1}$	$1.81.10^{-1}$	$2.16.10^{-1}$	
10.0	$1.69.10^{-1}$	$1.77.10^{-1}$	$2.20.10^{-1}$	
12.5		$1.78.10^{-1}$	$2.09.10^{-1}$	$2.42.10^{-1}$
15.0			$1.90.10^{-1}$	$2.47.10^{-1}$
17.5				$2.49.10^{-1}$
20.0				$2.73.10^{-1}$

Table 5.4: *RMS values [m/s] of all vector lengths in the time-averaged velocity fields of the simulations. The investigated area had a height of 19 cm.*

Appendix B: RMS data of experiments

In tables 5.5 and 5.6, the RMS data of the time-averaged velocity fields of the experiments can be found, where the experiments were performed in triplo. We only display the data for the height of 16 cm and 19 cm. It was found that the effect of the freeboard was substantial as can be seen when studying the trends at constant Γ for increasing f_z in both tables 5.5 and 5.6. The reason for this is that the vectors in the freeboard were usually very large, associated with the vigorous movement of single particles.

$f_z \downarrow \Gamma \rightarrow$	0.5	1.0	2.0	5.0
None	$3.15.10^{-2}$	$3.15.10^{-2}$	$3.15.10^{-2}$	$3.15.10^{-2}$
5.0	$4.93.10^{-2}$			
7.5	$3.86.10^{-2}$	$4.93.10^{-2}$	$7.02.10^{-2}$	
10.0	$4.01.10^{-2}$	$4.53.10^{-2}$	$6.95.10^{-2}$	
12.5		$3.90.10^{-2}$	$4.85.10^{-2}$	$7.67.10^{-2}$
15.0			$4.52.10^{-2}$	$7.04.10^{-2}$
17.5				$6.69.10^{-2}$
20.0				$5.14.10^{-2}$

Table 5.5: *RMS values [m/s] of all vector lengths in the time-averaged velocity fields of the experiments. The investigated area had a height of 16 cm.*

$f_z \downarrow \Gamma \rightarrow$	0.5	1.0	2.0	5.0
None	$5.38.10^{-2}$	$5.38.10^{-2}$	$5.38.10^{-2}$	$5.38.10^{-2}$
5.0	$7.08.10^{-2}$			
7.5	$6.28.10^{-2}$	$7.06.10^{-2}$	$8.04.10^{-2}$	
10.0	$6.15.10^{-2}$	$7.24.10^{-2}$	$8.50.10^{-2}$	
12.5		$5.32.10^{-2}$	$6.56.10^{-2}$	$9.20.10^{-2}$
15.0			$6.38.10^{-2}$	$8.62.10^{-2}$
17.5				$7.87.10^{-2}$
20.0				$7.04.10^{-2}$

Table 5.6: *RMS values [m/s] of all vector lengths in the time-averaged velocity fields of the experiments. The investigated area had a height of 19 cm, which includes a larger part of the freeboard than the data in table 5.5.*

Appendix C: Time averaging

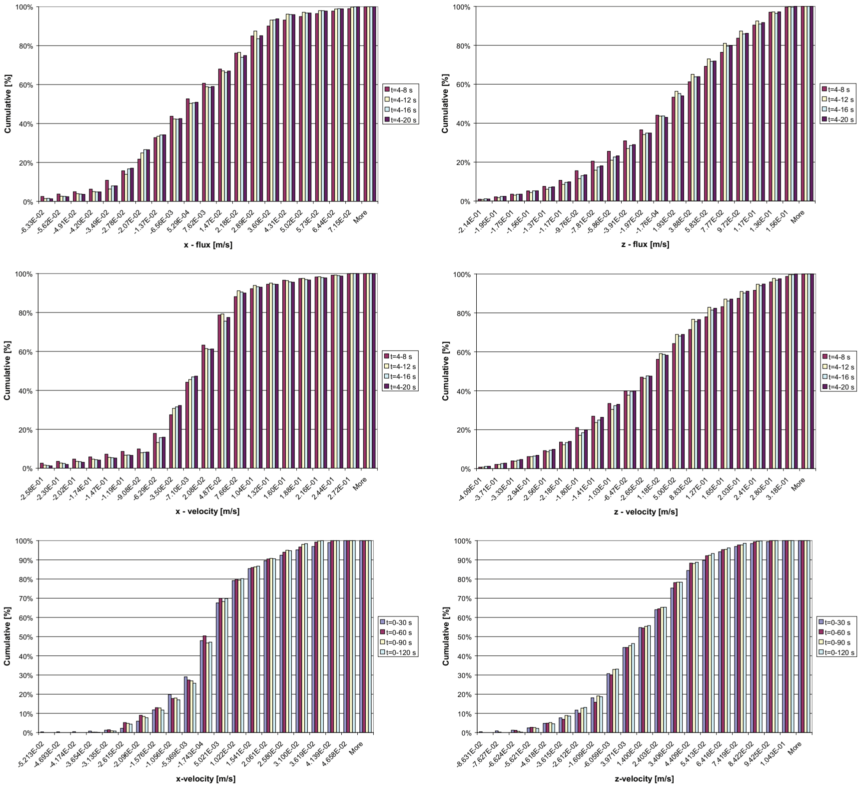

Figure 5.12: *(Top) Cumulative histogram for the x- and z-flux for the simulation results of a bed vibrated at 15 Hz ($\Gamma = 2.0$), simultaneously gas fluidized at 1.5 u$_{mf}$ (0.98 m/s). The investigated area had a height of 19 cm. (Middle) Cumulative histogram for the x- and z-velocity for the simulation results of a bed vibrated at 15 Hz ($\Gamma = 2.0$), simultaneously gas fluidized at 1.5 u$_{mf}$ (0.98 m/s). Both figures shows that the vector field is approximately constant starting from the average of t = 4-16 s. (Bottom) Cumulative histogram for the x- and z-velocity for the experimental results of conventional gas-fluidization at 1.5 u$_{mf}$ (0.98 m/s). The investigated area had a height of 16 cm. The figures show that the vector field is approximately constant when averaged over a time interval of more than 90 s.*

Bibliography

[1] E. Bratu, G.I. Jinescu, 'Effect of vertical vibrations on the pressure drop in a fluidised layer', Brit. Chem. Eng. **16**, p. 691 (1971).

[2] R. Gupta, A.S. Mujumdar, 'Aerodynamics of a Vibrated Fluid Bed', Can. J. Chem. Eng. **58**, p. 332 (1980).

[3] K. Erdész, A.S. Mujumdar, 'Hydrodynamic aspects of conventional and vibrofluidized beds - a comparative evaluation', Powd. Tech. **46**, p. 167 (1986).

[4] S. Mori, A. Yamamoto, S. Iwata, T. Haruta, I. Yamada, 'Vibro-fluidization of group-c particles and its industrial applications', AIChE Symp. Series **53**, p. 88 (1990).

[5] E. Marring, A.C. Hoffmann, L.P.B.M. Janssen, 'The effect of vibration on the fluidization behaviour of some cohesive powders', Powd. Tech. **79**, p. 1 (1994).

[6] E. Marco, A. Santos, M. Menéndez, J. Santamaría, 'Fluidization of agglomerating particles: influence of the gas temperature and composition on the fluidization of a Li/MgO catalyst', Powd. Tech. **92**, p. 47 (1997).

[7] K. Noda, Y. Mawatari, S. Uchida, 'Flow patterns of fine particles in a vibrated fluidized bed under atmospheric or reduced pressure', Powd. Tech. **99**, p. 11 (1998).

[8] D.V. Pence, D.E. Beasley, 'Chaos suppression in gas-solid fluidization', Chaos **8**, p. 514 (1998).

[9] T.-J. Wang, Y. Jin, A. Tsutsumi, Z. Wang, Z. Cui, 'Energy transfer mechanism in a vibrating fluidized bed', Chem. Eng. J. **78**, p. 115 (2000).

[10] J.R. Wank, S.M. George, A.W. Weimer, 'Vibro-fluidization of fine boron nitride powder at low pressure', Powd. Tech. **121**, p. 195 (2001).

[11] Y. Mawatari, T. Koide, Y. Tatemoto, T. Takeshita, K. Noda, 'Comparison of three vibrational modes (twist, vertical and horizontal) for fluidization of fine particles', Adv. Powd. Tech. **12**, p. 157 (2001).

[12] W. Yi, W. Ting-Jie, Y. Yi, J. Yong, 'Resonance characteristics of a vibrated fluidized bed with a high bed hold-up', Powd. Tech. **127**, p. 196 (2002).

[13] Y. Mawatari, T. Akune, Y. Tatemoto, K. Noda, 'Bubbling and bed expansion behavior under vibration in a gas-solid fluidized bed', Chem. Eng. Technol. **25**, p. 1095 (2002).

[14] V.A. Silva-Moris, S.C.S. Rocha, 'Development of a vibrofluidized bed and fluid-dynamic study with dry and wet adipic acid', Braz. J. Chem. Eng. **20**, p. 423 (2003).

[15] Y. Mawatari, Y. Tatemoto, K. Noda, 'Prediction of minimum fluidization velocity for vibrated fluidized bed', Powd. Tech. **131**, p. 66 (2003).

[16] Y. Mawatari, T. Koide, T. Ikegami, Y. Tatemoto, K. Noda, 'Characteristics of vibro-fluidization for fine powder under reduced pressure', Adv. Powd. Tech.

14, p. 559 (2003).

[17] Y. Mawatari, T. Ikegami, Y. Tatemoto, K. Noda, 'Prediction of agglomerate size for fine particles in a vibro-fluidized bed', J. Chem. Eng. Japan **36**, p. 277 (2003).

[18] M.-O. Coppens, J.R. van Ommen, 'Structuring chaotic fluidized beds', Chem. Eng. J. **96**, p. 117 (2003).

[19] Y. Tatemoto, Y. Mawatari, T. Yasukawa, K. Noda, 'Numerical simulation of particle motion in vibrated fluidized bed', Chem. Eng. Sci. **59**, p. 437 (2004).

[20] T. Zhou, H. Ogura, M. Yamamura, H. Kage, 'Bubble motion pattern and rise velocity in two-dimensional horizontal and vertical vibro-fluidized beds', Can. J. Chem. Eng. **82**, p. 236 (2004).

[21] H. Jin, Z. Tong, J. Zhang, B. Zhang, 'Homogeneous fluidization characteristics of vibrating fluidized beds', Can. J. Chem. Eng. **82**, p. 1048 (2004).

[22] C.H. Nam, R. Pfeffer, R.N. Dave, S. Sundaresan, 'Aerated vibrofluidization of silica nanoparticles', AIChE Journal **50**, p. 1776 (2004).

[23] Y. Tatemoto, Y. Mawatari, K. Noda, 'Numerical simulation of cohesive particle motion in vibrated fluidized bed', Chem. Eng. Sci. **60**, p. 5010 (2005).

[24] Y. Mawatari, M. Tsunekawa, Y. Tatemoto, K. Noda, 'Favorable vibrated fluidization conditions for cohesive fine particles', Powd. Tech. **154**, p. 54 (2005).

[25] Y. Mawatari, K. Tagawa, Y. Tatemoto, K. Noda, 'Bubbling characteristics under vertical vibration in a two-dimensional fluidized bed', J. Chem. Eng. Japan **38**, p. 18 (2005).

[26] X.S. Wang, M.J. Rhodes, 'Pulsed fluidization - a DEM study of a fascinating phenomenon', Powd. Tech. **159**, p. 142 (2005).

[27] X.S. Wang, M.J. Rhodes, 'Using pulsed flow to overcome defluidization', Chem. Eng. Sci. **60**, p. 5177 (2005).

[28] Internet link: www.niro.com, 'The vibro-fluidizer'.

[29] S.J. Moon, I.G. Kevrekidis, S. Sundaresan, 'Particle simulation of vibrated gas-fluidized beds of cohesive fine powders', Ind. Eng. Chem. Res. **45**, p. 6966 (2006).

[30] J.M. Link, C. Zeilstra, N.G. Deen, J.A.M. Kuipers, 'Validation of a Discrete Particle Model in a 2D Spout-Fluid bed using non-intrusive optical measuring techniques', Can. J. Chem. Eng. **82**, p. 30 (2004).

[31] J.M. Link, 'Development and Validation of a Discrete Particle Model of a Spout-Fluid Bed Granulator', Ph.D. Thesis University of Twente, 2006.

6

Impact Phenomena for Static Granular Assemblies

ABSTRACT

In this chapter, the impact of sphere on a static bed of fine particles is investigated. In experiments, performed by Lohse and co-workers, after initial contact, the falling sphere generates a channel as it passes through the granular bed. The channel collapses due to 'hydrostatic' pressure and a granular jet emerges. In the pseudo-2D simulations with 500 μm particles, similar observations as in the experiments are found, although the jet was less pronounced than in the experiments, where 40 μm sand was used. A theoretical scaling law was tested, but it was found that the simulation data did not agree with the assumptions underlying this law. The discrepancy is most likely caused by the differences between our model system and the experimental one.

The numerical work described in this chapter is to be considered part of this thesis. Experiments and void collapse analysis are work of Bergmann *et al.* [17] and were only included for clarity reasons.

6.1 Introduction

According to Shoemaker, the 'impact of solid bodies is the most fundamental process that has taken place on the terrestrial planets' [1], as they shape the surfaces of all solar system bodies. A lot of information on this process has been extracted from remote observations of impact craters on planetary surfaces. However, the nature of the geophysical impact events is that they are non-reproducible. Moreover, their scale is enormous and direct observations are not possible. On the other hand, Thoroddsen and Shen did small scale experiments by letting a lead sphere fall on monodisperse spherical glass beads [2]. They found a jet emerging from the impact site. Similar jets are long known when a ball or a fluid droplet impacts on a liquid surface [3–7]. Recently at Twente University, similar experiments as in [2] have been performed, but now on extremely fine sand (average grain size of about 40 μm; grains are non-spherical) [8, 17]. In previous experiments, it proved to be hard to achieve quantitatively reproducible results, most likely due to the random nature of the force-chain networks in the granular material [9–12]. Therefore, in order to prepare a well-defined initial state, fine sand is decompactified and homogenized by blowing air through it via a perforated bottom plate. The height of the sand bed above the bottom plate is typically 25-40 cm. The air is slowly turned off before the experiments and the grains are left to settle in an extremely loose packing (solids fraction $\varepsilon_s = 0.41$) with the force chains either broken or substantially weakened, which may be called a 'fluid-like' state. Impact events on this well-prepared fine sand will be gravity dominated. A steel ball (radius $R_0 = 1.25$ cm) is dropped from various heights (up to 1.5 m) onto the sand, and the dynamics of the sand are observed with a digital high-speed camera (up to 2000 frames per second).

The series of *visible* events is as follows (see Fig. 6.1): First, the ball vanishes in the sand and a crownlike splash is created. Inhomogeneities develop in the crown, due to the inelastic particle interactions (Fig. 6.1, frames 3-5). Then, after a while, a *jet* shoots out of the sand at the position of impact. In all of the experiments the jet height exceeds the release height of the ball; see Fig. 6.2(a). While the upper part of the jet is still going upward, in the lower parts the inelastic particle-particle collisions lead to density inhomogeneities in the jet (Fig. 6.1, frames 7-8). These inhomogeneities resemble those of the surface tension driven Rayleigh instability of a water jet, even though there is no surface tension in granular matter. Finally, after about half a second, a *granular eruption* is seen at the position of impact, resembling a volcano (Fig. 6.1, frame 8-9). The collapsing jet first leaves a *central peak* in the crater [13–15], but the granular eruption violently erases this peak.

How does the jet form? To answer this question, it is essential to find out what is going on below the surface of the sand. To this end, we have performed discrete particle simulations of the impact of a large intruder in a bed of glass spheres. This chapter is ordered as follows: we will first describe the theoretical description of the void formation. Then, we will describe the simulation model and parameters. After this, we will discuss the simulation results and finally draw conclusions.

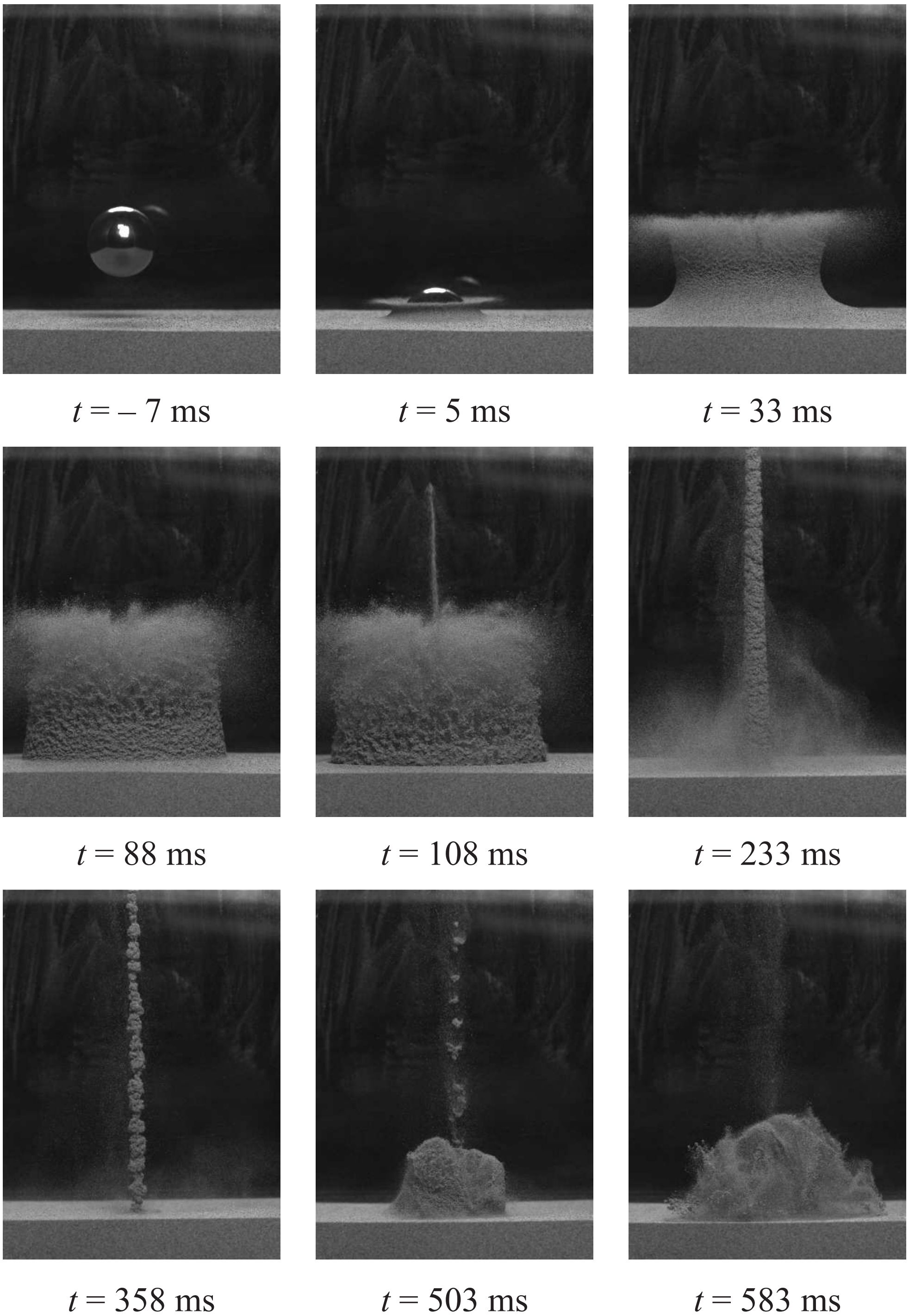

$t = -7$ ms

$t = 5$ ms

$t = 33$ ms

$t = 88$ ms

$t = 108$ ms

$t = 233$ ms

$t = 358$ ms

$t = 503$ ms

$t = 583$ ms

Figure 6.1: *Jet formation after the impact ($v_0 = 2.43$ m/s) of a steel ball of $R_0 = 1.25$ cm on loose very fine sand. The jet in this experiment exceeds the release height of the ball. Frames 2-4: splash; frames 5-6: a jet emerges; frame 7: clustering within the jet; frames 8-9: granular eruption at the surface.*

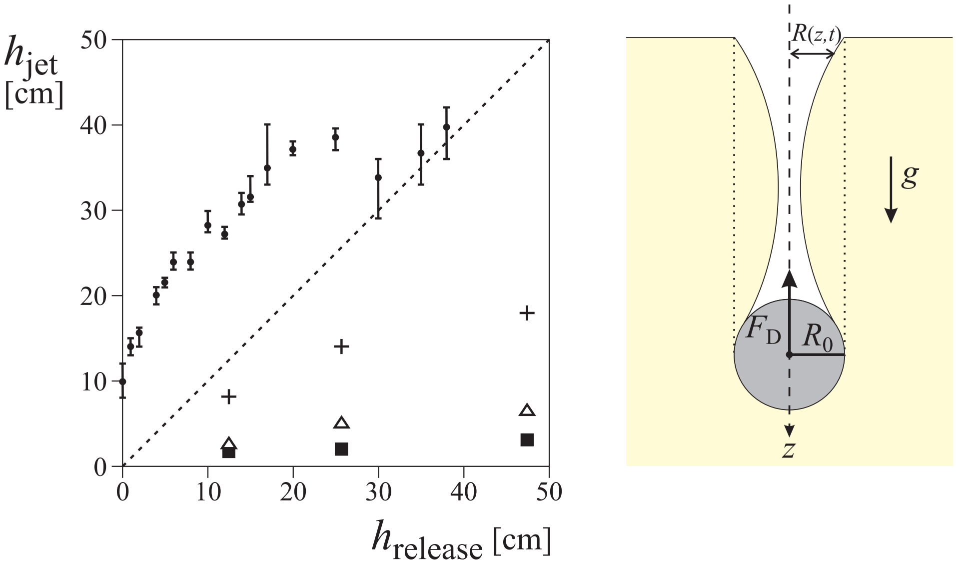

Figure 6.2: *(a) Jet height as a function of release height of the ball in the experiments (solid bullets with error bars) and in those of ref. [2] (for spheres in a granulate of different diameter:* $d_s = 0.08$ *mm (pluses),* $d_s = 0.118$ *mm (triangles),* $d_s = 0.176$ *mm (solid squares)). The jets of ref. [2] never reach the release height, because the granulate is less fine and much less decompactified. In the experiments jets are produced even at zero impact height [23] and there is no scaling relation as in ref. [2]. (b) Sketch of the void collapse. When the accelerated sand grains from the sidewalls of the cylindrical cavity collide on the axis of the cavity, two jets are formed: One downward into the entrained air bubble formed above the sphere, and one upward straight into the air.*

6.2 Theory

First, the delay curve $z(t)$ of the ball in the sand can be obtained from a simple force balance model involving drag, gravity, and added mass. It describes the experimental results obtained for a falling ball equipped with a thin stiff tail, which allows for easy depth measurements [23]. The delay curve $z(t)$ of the ball is inverted to obtain $t_{pass}(z)$, the time when the ball passes the layer of sand at depth z beneath the bed surface. This sets the initial conditions for the two-dimensional collapse of the void at this depth, namely $R(z, t_{pass}) = R_0$ and $\dot{R}(z, t_{pass}) = 0$. Here, $R(z, t)$ is the time and depth dependent radius of the void, see Fig. 6.2b.

Next, the collapse of the void formed by the ball has to be described. It is driven by the (hydrostatic) sand pressure $p(z)$ at depth z. For small z the pressure simply is $p(z) = \rho_s g z$; for larger z it saturates, as postulated by Rayleigh and Janssen [18]. Here, ρ_s is the sand density, assumed to be constant. If one neglects the dissipative processes both between the different layers of sand and between the sand grains in

---

This theory has been developed by D. van der Meer, R. Bergmann, D. Lohse and A. Prosperetti.

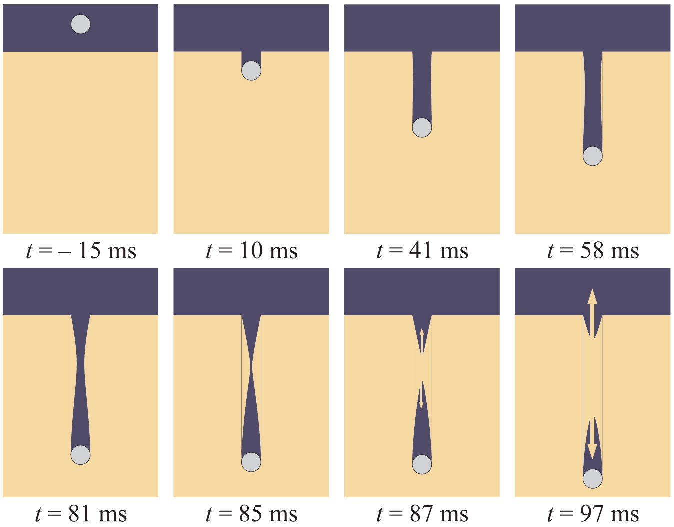

Figure 6.3: *Cross-section of the 3D-void collapse following from the Rayleigh-type model, for the same impact velocity and ball radius as in Fig. 6.1. The void is pressed together by the 'hydrostatic' pressure from the side, leading to a singularity and an upward and downward jet.*

one layer, the dynamics for fixed depth z is determined by the Euler equation,

$$\rho_s \left(\frac{\partial v(r,t)}{\partial t} + v(r,t) \frac{\partial v(r,t)}{\partial r} \right) = - \frac{\partial p(r,t)}{\partial r} \quad , \tag{6.1}$$

where $v(r,t)$ is the velocity field in the sand. With continuity $\partial_r[rv(r,t)] = 0$, and with the boundary conditions $v(R(t),t) = \dot{R}(t)$ at the void's wall and $v(R_\infty,t) = 0$ far away from the void, one obtains a Rayleigh-type [19, 20] ordinary differential equation for each $R(z,t)$, namely,

$$\left(R\ddot{R} + \dot{R}^2 \right) \log \frac{R}{R_\infty} + \frac{1}{2}\dot{R}^2 = \frac{1}{\rho_s} p(z) = gz \quad . \tag{6.2}$$

The dynamics following this Rayleigh-type model is shown in Fig. 6.3, resembling the void collapse in the discrete particle model (Fig. 6.4), in the 2D experiments [8], in experimental work on the void collapse in transparent fluids [3–7, 16], in boundary integral simulations of the complete hydrodynamical equations [21], and therefore presumably also in the 3D experiments in sand shown in Fig. 6.1. Having shown that the void collapse is driven by hydrostatic pressure, one can now deduce scaling arguments [22] for the limiting case of large impact velocity v_0, which is the relevant one in the geophysical context. The time up to void collapse in depth z is the sum of the time z/v_0 it takes the ball to get there and the collapse time itself, which scales as $\sim R_0/\sqrt{gz}$. The depth z_c where the walls of the void first touch (i.e., the position of the singularity) can be obtained from minimizing

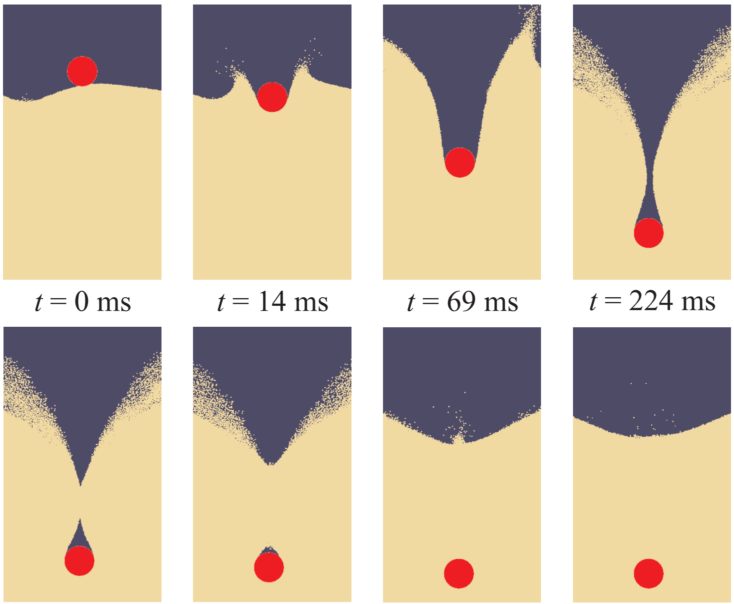

$t = 0$ ms $t = 14$ ms $t = 69$ ms $t = 224$ ms

$t = 245$ ms $t = 273$ ms $t = 385$ ms $t = 495$ ms

Figure 6.4: *A cut through the pseudo-2D discrete particle simulation (for visualization purposes we only show the impact region of bed). Frames 1-3: the impact of the disk on the particles; Frames 4-6: the collapse of the void; Frame 7: the upward jet (which is less pronounced than in the 3D experiments).*

this sum with respect to z, resulting in $z_c/R_0 \sim \mathrm{Fr}^{1/3}$, where $\mathrm{Fr} = v_0^2/(gR_0)$ is the Froude number. From this, one obtains that the time of the collapse t_c scales as $t_c \sim (R_0/v_0)\mathrm{Fr}^{1/3} \sim \sqrt{R_0/g}\mathrm{Fr}^{-1/6}$. For large v_0, these scaling laws are consistent with the continuum model. In this chapter, we will investigate if the discrete particle simulations can be used to validate this theoretical evaluation of the impact phenomenon.

6.3 Simulations

The size of the experimental system was such that the number of particles was far too large to handle with the discrete particle model, which is described in detail in Chapter 2. Therefore, we had to downscale both the dimensions of the simulation box and increase the particle size. As a result, we modeled a pseudo-2D system with 1.3 million particles of $r_p = 250\ \mu$m radius and density 1000 kg/m^3, where a narrow ($\sigma = 25\ \mu$m) Gaussian size distribution was used. The sphere being dropped onto the granular bed (hence called 'intruder') had a radius R_0 of 7.5 mm and a density of 1400 kg/m^3. We chose these densities different from the experiments where fine sand (2500 kg/m^3) and a steel intruder (7700 kg/m^3) where used, in order to reduce

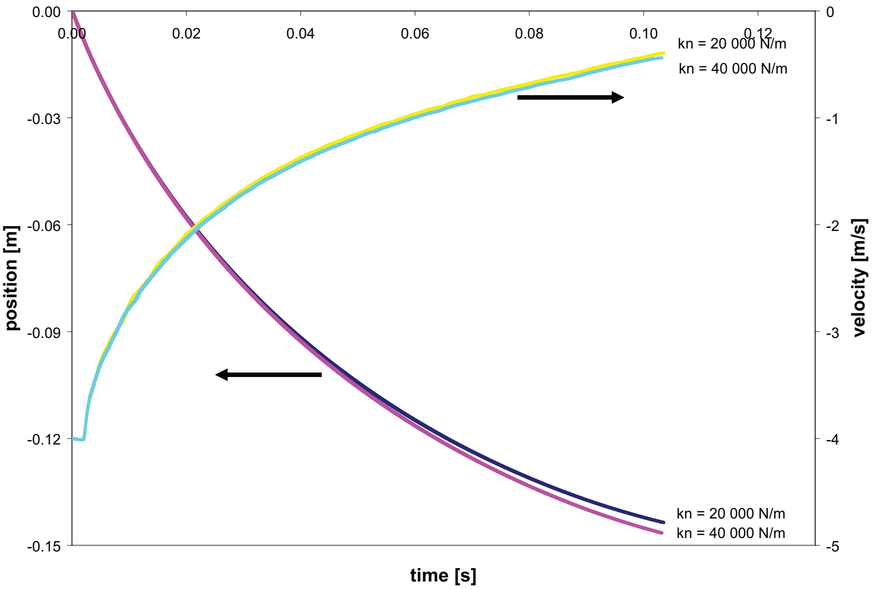

Figure 6.5: *Test of the intruder trajectory and velocity as a function of normal spring stiffness, where the velocity curves start in the lower left corner and the trajectory curves in the upper left corner. The initial intruder position is 0.15 m. The difference in intruder trajectory increased gradually to a maximum value of 3 mm at the end of the simulation. The difference in velocity was approximately constant at 0.03 m/s. The final location of the singularity differed only 2 mm.*

computational time that would be required since the normal spring stiffness would need to be increased. As collision parameters, we used a normal (e_n) and tangential (e_t) restitution coefficient of 0.97 and 0.33, respectively, which are typical values for 'sand-like' materials. The inter-particle friction coefficient (μ_{pp}) was set to 0.1. The effect of the particle-wall friction coefficient was investigated by setting either to a value of 0.1 or by deactivating it. The normal spring stiffness (k_n) was set to 20,000 N/m. As usual for soft-sphere simulations, we tested how sensitive the results are on the value of the spring stiffness by comparing the trajectory of the intruder with a case where a larger stiffness (40,000 N/m) was used. It was found that the trajectories slowly started to deviate, but the effect was minimal (Fig. 6.5). Additionally, the location of the singularity, i.e., the depth where the walls of the channel first touch, was nearly the same (within 2 %).

The dimensions of the box were $0.24 \times 0.004 \times 0.36$ m^3. Since we have a pseudo-2D system, we solved the gas-phase equations in only 2 dimensions, so that the domain was divided into 160×240 CFD cells (grid size 1.5 mm). The granular bed was prepared by fluidizing the smaller particles and subsequently decreasing the gas velocity to zero. The resulting bed, however, did not attain the experimentally

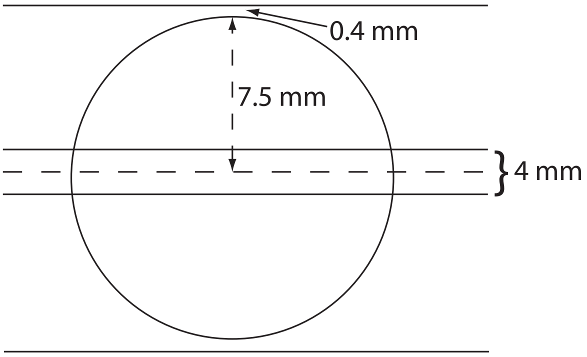

Figure 6.6: *Top view of an intruder, being dropped onto a granular bed. A set of extra walls (frictionless) was implemented to keep the center of the sphere above the granular bed, making the intruder more or less 'disc-like'. Due to the curvature of the sphere, the radius near the front and back wall was a little smaller (7.1 mm instead of 7.5 mm). It is not expected that this will have a pronounced effect on the channel collapse, however this has not been tested.*

obtained extremely loose packing of $\varepsilon_s = 0.41$. Instead, a granular bed height was 0.146 m was obtained, corresponding to $\varepsilon_s \sim 0.60$. At present it remains unclear why such a loose packing can be achieved in the experiments. In the experiments, the particles are rounded with aspect ratios between approximately 0.5 and 2 and the grain size varies between 10 and 100 μm, while in the simulations we have only a small spread in size (between 450 and 550 μm) and the particles are spherical. It may be that (i) non-sphericity, (ii) polydispersity, (iii) an attractive force (such as electrostatics or van der Waals force) or (iv) a combination of these can account for the low packing fraction obtained in the experiments. The reader may have noticed that the diameter of the intruder is much larger than the width of box. As a consequence, the intruder may be considered a disc, as shown in Fig. 6.6. It should be stressed that in these simulations, there was no interaction between the intruder and the gas-phase, i.e., the only 'drag' that the intruder experiences is from collisions with the smaller particles. From the gas-phase point of view, the volume occupied by the intruder is empty (i.e., $\varepsilon_s = 0$).

6.4 Results and discussion

In Fig. 6.4, the series of events can be observed when a 1.5 cm diameter ball is dropped onto the beads with an impact velocity of 2 m/s, revealing the jet formation process shown in Fig. 6.1: The impacting ball creates a void which is then pressed together through the 'hydrostatic' pressure from the side. At the position where the collapse is completed first, the void walls hit each other. It is this singularity which leads to the formation of *two* jets: one upwards and one downwards into an air bubble which was entrained in the sand by the void collapse. These

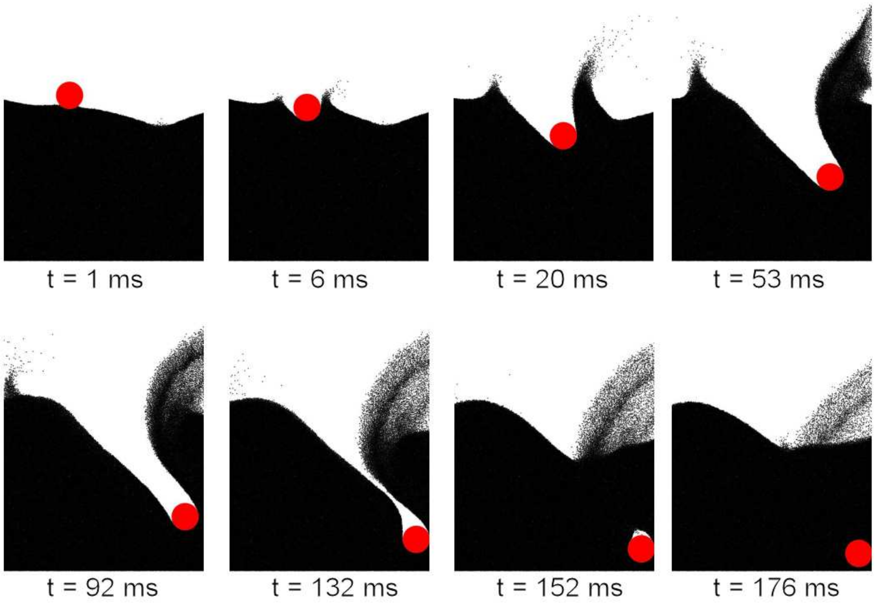

Figure 6.7: *A cut through the pseudo-2D discrete particle simulation for an oblique impact for visualization purposes we only show the impact region of bed). Frames 1-4: the oblique impact of the disk on the particles; Frames 5-7: the collapse of the void; Frame 8: the upward jet (which is less pronounced than in the pseudo-2D simulations for vertical impacts).*

events also occur in oblique impacts, as shown in Fig. 6.7. Note that the jet in the discrete particle simulations is much less pronounced than in the experiments, for which there may be two explanations. First, the singularity due to the focusing along the axis of symmetry is weaker in 2D and pseudo-2D since the collapse is only 2D in nature. Indeed, experiments revealed a jet which was much smaller compared to the jet in Fig. 6.1. Second, because - in comparison with the intruder - the beads in the simulations are much larger (size ratio intruder / beads ~ 30) than the sand grains in the experiment (size ratio ~ 600); i.e., the sand bed is less fluid-like. Third, the effect of gas forces is stronger in the fine sand used in the experiments as compared to the beads in the simulation. Having shown that the principle dynamics of the void collapse and jet formation are present in our discrete particle model, we now want to investigate the proposed scaling arguments in a more quantitative manner by analysis of the collapse data obtained from the simulations.

Since it was difficult to determine the exact location of the singularity with software, we measured this data from images of the impact. In these images - which were recorded every 1 ms - the depth beneath the bed surface of the singulary (z_c) could be determined with an accuracy of ~ 1.3 mm. The data so obtained can be found in tables 6.1 and 6.2.

Case	v_0	g	z_c	$R_0/\sqrt{gz_c}$	$t_{c,close}$
1	-2.5	-9.81	$4.70\ 10^{-2}$	$1.10\ 10^{-2}$	$7.34\ 10^{-2}$
2	-3.0	-9.81	$5.42\ 10^{-2}$	$1.03\ 10^{-2}$	$7.17\ 10^{-2}$
3	-4.0	-9.81	$6.13\ 10^{-2}$	$9.67\ 10^{-3}$	$7.58\ 10^{-2}$
4	-4.5	-9.81	$6.91\ 10^{-2}$	$9.11\ 10^{-3}$	$6.95\ 10^{-2}$
5	-5.0	-9.81	$6.97\ 10^{-2}$	$9.07\ 10^{-3}$	$7.39\ 10^{-2}$
6	-6.0	-9.81	$7.56\ 10^{-2}$	$8.71\ 10^{-3}$	$7.45\ 10^{-2}$
7	-2.0	-4.91	$5.09\ 10^{-2}$	$1.50\ 10^{-2}$	$1.01\ 10^{-1}$
8	-2.0	-9.81	$4.12\ 10^{-2}$	$1.18\ 10^{-2}$	$7.21\ 10^{-2}$
9	-2.0	-14.72	$3.86\ 10^{-2}$	$9.95\ 10^{-3}$	$5.75\ 10^{-2}$
10	-2.0	-19.62	$3.47\ 10^{-2}$	$9.09\ 10^{-3}$	$5.06\ 10^{-2}$

Table 6.1: *Simulation data with the particle-wall friction activated ($\mu_{pw} = 0.1$), using an intruder density of 3500 kg/m^3. In the table, v_0 is the initial intruder velocity at time of impact [m/s], g the gravitational acceleration [m/s^2], z_c the depth (measured from the bed surface) of the singularity [m], $R_0/\sqrt{gz_c}$ the scaling for the channel collapse (see eq. 6.3) and $t_{c,close}$ is the time required to collapse the channel at the depth of the singularity. The intruder diameter had a fixed value of 1.5 cm and we varied the initial impact velocity as well as the gravity constant.*

Case	v_0	g	z_c	$R_0/\sqrt{gz_c}$	$t_{c,close}$
1	-2.0	-9.81	$4.67\ 10^{-2}$	$1.11\ 10^{-2}$	$4.95\ 10^{-2}$
2	-2.5	-9.81	$5.48\ 10^{-2}$	$1.02\ 10^{-2}$	$5.03\ 10^{-2}$
3	-3.0	-9.81	$6.32\ 10^{-2}$	$9.52\ 10^{-3}$	$4.96\ 10^{-2}$
4	-3.5	-9.81	$6.97\ 10^{-2}$	$9.07\ 10^{-3}$	$5.02\ 10^{-2}$
5	-4.0	-9.81	$7.95\ 10^{-2}$	$8.49\ 10^{-3}$	$4.86\ 10^{-2}$
6	-5.0	-9.81	$9.18\ 10^{-2}$	$7.90\ 10^{-3}$	$4.90\ 10^{-2}$
7	-2.0	-14.72	$3.86\ 10^{-2}$	$9.95\ 10^{-3}$	$4.22\ 10^{-2}$
8	-2.0	-19.62	$3.54\ 10^{-2}$	$9.01\ 10^{-3}$	$3.70\ 10^{-2}$

Table 6.2: *As in table 6.1, but now for cases where the particle-wall friction was deactivated. The intruder diameter was 1.5 cm (density 1400 kg/m^3) and we varied the initial impact velocity as well as the gravity constant.*

The expression that describes the required time to collapse the channel (t_{close}, measured from when the intruder initially hits the bed surface) is:

$$t_{close}(z) = \frac{z}{v_0} + C\frac{R_0}{\sqrt{gz}} = \frac{z}{v_0} + t_{c,close} \tag{6.3}$$

where the first term on the right-hand side describes the time taken by the intruder to travel to a certain depth z and the second term describes the time required for the channel to close ($t_{c,close}$) at depth z. Furthermore, C is a constant, R_0 the intruder radius and g the gravity constant. Minimization of this sum leads to the earlier proposed scaling law $z_c/R_0 \sim \mathrm{Fr}^{1/3}$.

Two assumptions are used in this scaling law. One is that the intruder velocity is approximately constant until it reaches the singularity, and the other is that the collapse time of the channel ($t_{c,close}$) depends on the depth z beneath the bed surface according to hydrostatic pressure. For the first assumption, we found that the intruder velocity strongly decreased as it passed through the granular bed (also illustrated in Fig. 6.5). The second assumption implies that $t_{c,close}$ is a linear function of $R_0/\sqrt{gz}$, on which we will elaborate below.

We measured the closing time of the channel ($t_{c,close}$) using the following procedure. We first determined the depth of the singularity (z_c) and - from the intruder trajectory data - we looked up the time at which the intruder center was at this depth z_c. From this point the channel starts to collapse. Finally, we determined the time when the channel walls first touch, indicating the end of the collapse. The time difference gives $t_{c,close}$.

The collapse data in the tables are visualized in Fig. 6.8 and Fig. 6.9. These figures show that the collapse time $t_{c,close}$ does not significantly depend on $R_0/\sqrt{gz}$ when we change the depth of singularity (i.e., by using different impact velocities v_0). This would indicate that the assumption of 'hydrostatic' pressure is not correct for these conditions. Interestingly enough, we *do* find that $t_{c,close}$ is linear with $R_0/\sqrt{gz}$ when we change gravity.

The scaling law was validated on the basis of the visual similarities between results from the Rayleigh-type model and the experiments. However, it becomes clear the theoretical scaling cannot be confirmed from the discrete particle simulations described above, although the visual observations are the same as in the theory (i.e., compare figures 6.3 and 6.4). However, one should be careful to draw firm conclusions on the basis of our simulations, since the conditions are very different from those in the experiment. First of all, the particles in our simulations are much larger than the sand grains in the experiments. Second, the singularity due to the focusing along the axis of symmetry is weaker in pseudo-2D simulations (and experiments) and the jet will take the form of a sheet. Third, we could not obtain the extremely loose packing obtained in the experiments. One of the effects may be that the assumption of a constant intruder velocity is much more valid in the experiments than in the simulations, where we found that the velocity of the intruder was strongly reduced during impact. Fourth, it may be that in the simulations - in analogy to the Rayleigh-Janssen law - the hydrostatic pressure was

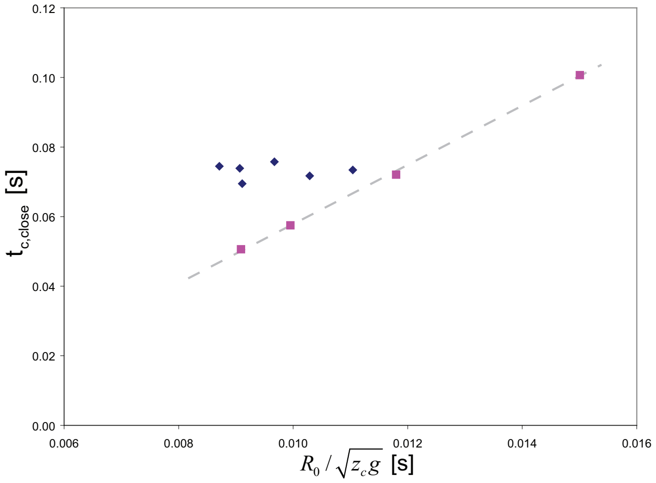

Figure 6.8: *The collapse time of the channel $t_{c,close}$ as a function of $R_0/\sqrt{gz_c}$, for the data presented in table 6.1 (particle-wall friction active). The diamonds are the simulations with constant gravity (9.81 m/s^2), but with varying values for v_0 and, consequently, z_c. v_0 increases from right to left. The plot shows that the values for $t_{c,close}$ are approximately constant for all z_c. The squares are the simulations with constant impact velocity (2 m/s), but varying values for the gravity. It was found that the collapse time does not significantly depend on the depth of the singularity. However, a linear dependence was when changing gravity (the dashed line is a guide to the eye).*

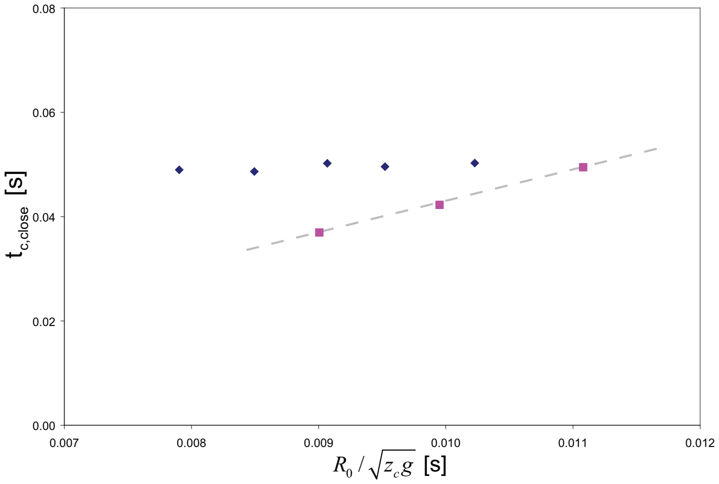

Figure 6.9: *The collapse time of the channel $t_{c,close}$ as a function of $R_0/\sqrt{gz_c}$, for the data presented in table 6.2 (particle-wall friction deactivated). Although the absolute values for the collapse time are different compared to Fig. 6.8, again the same trends are observed (the dashed line is a guide to the eye).*

saturated for depths where the singularity took place (z_c), and that therefore similar collapse times $t_{c,close}$ were found. This could be coupled to the fact that in the pseudo-2D system there are many more particle-wall contacts as compared to 3D systems, so that particles may be more ‘supported’ by the sidewalls. The observation that changing the gravity constant *does* have an effect on the collapse time of the channel suggests that the assumption of hydrostatic pressure may well be valid in a truly 3D system.

We finally discuss the role of the ambient air and the ambient pressure for the evolution of the jet: (i) For (3D) experiments with very high impact velocities it was observed that after the splash the crown goes inwards rather than outwards, due to the pressure reduction behind the fast projectile (Bernoulli’s law). The crown, in fact, can fully close and the jet then hits the closed crown, leading to an explosion-like collision with significant spreading of the particles. (ii) In impact experiments on very fine and loose sand but with strongly reduced ambient pressure the jet, in fact, is less pronounced than with ambient pressure [24]. For larger particles (500 μm) we redid above discrete particle simulations, but now reduced the air pressure to zero (vacuum) after fluidization. This was found to give very similar results as compared to the jet formation in the atmospheric case. More research on the role of air in loose fine granular material clearly is required.

Bibliography

[1] E.M. Shoemaker, in *Impact and Explosion Cratering*, edited by D.J. Roddy, R.O. Pepin and R.B. Meril (Pergamon Press, New York, 1977), p. 1-10.

[2] S.T. Thoroddsen, A.Q. Shen, ‘Granular Jets’, Phys. Fluids **13**, p. 4 (2001).

[3] A.M. Worthington, *A Study of Splashes* (Longman and Green, London, 1908).

[4] H. Oguz, A. Prosperetti, ‘Bubble entrainment by the impact of drops on liquid surfaces’, J. Fluid Mech. **219**, p. 143 (1990).

[5] A. Prosperetti, H. Oguz, ‘The impact of drops on liquid surfaces and the underwater noise of rain’, Annu. Rev. Fluid Mech. **25**, p. 577 (1993).

[6] J.E. Hogrefe, N.L. Peffley, C.L. Goodridge, W.T. Shi, H.G.E. Hentschel, D.P. Lathrop, ‘Power-law singularities in gravity-capillary waves’, Physica D (Amsterdam) **123**, p. 183 (1998).

[7] D. Lohse, ‘Bubble puzzles’, Phys. Today **56**, p. 36 (2003).

[8] R. Mikkelsen, M. Versluis, E. Koene, G.-W. Bruggert, D. van der Meer, K. van der Weele, D. Lohse, ‘Granular eruptions: Void collapse and Jet Formation’, Phys. Fluids **14**, S14 (2002).

[9] C.H. Liu, S.R. Nagel, D.A. Schecter, S.N. Coppersmith, S. Majumdar, O. Narayan, T.A. Witten, ‘Force fluctuations in bead packs’, Science **269**, p. 513 (2002).

[10] H.M. Jaeger, S.R. Nagel, R.P. Behringer, 'Granular solids, liquids, and gases', Rev. Mod. Phys. **68**, p. 1259 (1996).

[11] L. Kadanoff, 'Built upon sand: Theoretical ideas inspired by granular flows', Rev. Mod. Phys. **71**, p. 435 (1999).

[12] C.S. O'Hern, S.A. Langer, A.J. Liu, S.R. Nagel, 'Force distributions near jamming and glass transitions', Phys. Rev. Lett. **86**, p. 111 (2001).

[13] Similar peaks are observed in many craters of the terrestrial planets [14, 15].

[14] P.H. Schultz, 'Atmospheric effects on ejecta emplacement and crater formation on Venus from Magellan', J. Geophys. Res. Planets **97**, 16183 (1992).

[15] A.M. Walsh, K.E. Holloway, P. Habdas, J.R. de Bruyn, 'Morphology and scaling of impact craters in granular media', Phys. Rev. Lett. **91**, 104301 (2003).

[16] J.W. Glasheen, T.A. McMahon, 'A hydrodynamic model of locomotion in the basilisk lizard', Nature (London) **380**, p. 340 (1996).

[17] D. Lohse, R. Bergmann, R. Mikkelsen, C. Zeilstra, D. van der Meer, M. Versluis, K. van der Weele, M. van der Hoef, J.A.M. Kuipers, 'Impact on soft sand: Void collapse and jet formation', Phys. Rev. Lett **93**, 198003 (2004).

[18] J. Duran, *Sands, Powders, and Grains* (Springer, New York, 1999), 1st ed.

[19] L. Rayleigh, 'On the pressure development in a liquid during the collapse of a spherical cavity', Philos. Mag. **34**, p. 94 (1917).

[20] H.N. Oguz, A. Prosperetti, 'Dynamics of bubble-growth and detachment from a needle', J. Fluid Mech. **257**, p. 111 (1993).

[21] S. Gaudet, 'Numerical simulation of circular disks entering the free surface of a liquid', Phys. Fluids **10**, p. 2489 (1998).

[22] H.N. Oguz, A. Prosperetti, A.R. Kolaini, 'Air entrapment by a falling water mass', J. Fluid Mech. **294**, p. 181 (1995).

[23] D. Lohse, R. Rauhé, R.P.H.M. Bergmann, and D. van der Meer, 'Creating a dry variety of quicksand', Nature **432**, p. 689 (2004).

[24] J.R. Royer, E.I. Corwin, A. Flior, M-L. Cordero, M. Rivers, P. Eng, H.M. Jaeger, 'Formation of Granular Jets Observed by High-Speed X-ray Radiography', Nature Physics **1**, p. 164 (2005).

7

Impact Phenomena Using a Hybrid DPM-IBM method

ABSTRACT

In this chapter, a first attempt has been made to incorporate the immersed boundary method (IBM) - which can be used to describe the gas-solid interaction of particle much larger than the computational grid - into DPM. The motivation for doing so is that it allows to study the effect of interstitial air in granular systems with particles that strongly differ in size. Although the model is still far from perfect (in particular it suffers from grid-size and time step dependence), it has been used - as a first application - to measure the viscosity of the granular medium by using a method similar to the 'falling sphere' method used in experiments for determining the viscosity. In our case, the intruder is pulled through the granular bed with constant velocity. The drag force was measured as function of the intruder velocity and - assuming that the Stokes-Einstein drag law is valid for the gas-solid suspension - values for the granular viscosity in the range 0.6-0.9 Pa.s were found for this particular system. Despite the relatively coarse computational grids employed in the simulations, the computed viscosities are close to the range reported in literature.

7.1 Introduction

When particles are sufficiently small, the interstitial air can have a pronounced effect on the typical phenomena that they display. One example is given in Chapter 4 (bronze/glass segregation) of this thesis, however, there are other examples which involve a single large sphere ('intruder'). For example, in a study of granular jets - such as those discussed in Chapter 6 - Royer *et al.* found that the jet formation could be suppressed when the air pressure was reduced [1]. Similarly, Möbius *et al.* found that the air pressure had a profound effect on the Brazil Nut effect, even making that the intruder (the 'Brazil Nut') could sink instead of going to the top [4]. It is desirable to obtain more detailed information on such experiments in order to gather further support for the theoretical arguments used to explain the experimental observations. From a modeling point of view however, the treatment of such large spheres in the presence of many much smaller ones is non-trivial. For example, in the discrete particle model, the coupling between gas and particles requires that the grid cells are larger than the particle size and it is for this reason that the intruder in the granular jet simulations of Chapter 6 was not coupled to the gas phase.

Proper interaction between the intruder and the gas phase requires a fully resolved treatment of the gas-solid coupling. In other words: the no-slip velocity boundary condition at the intruder surface needs to be modeled. This can be done using the immersed boundary method (IBM) [2,3]. In this chapter, we discuss and test the implementation of this method in the discrete particle model. As a preliminary test case, we investigate the forces experienced by an intruder being pulled through a fluidized granular bed operated near minimum fluidization velocity. Depending on the relationship between the forces and intruder velocity, a granular viscosity of the gas-solid suspension may be obtained. The chapter is organized as follows. First, the new model is tested with respect to the forces acting on a single sphere and on an sphere moving through a fluidized granular bed. In the second part, preliminary tests regarding the granular viscosity are performed: first, an overview on experimental measurement techniques and findings is given. After this, the simulation parameters for the actual drag simulations are presented and the results of subsequent simulations are discussed. Finally, we will draw conclusions about the suitability of the new model and discuss possible enhancements.

7.2 Simulation method

In this section, we focus on the numerical method used in our simulations and give a schematic overview of its' implementation in the flow solver, including some tests to ascertain the validity of the method for our application. For a more comprehensive computational scheme of the discrete particle model, the reader is referred to Chapter 2.

We want to simulate a system where an intruder is moving through a bed of small particles, with a typical diameter ratio of 1:20. The difficulty with such a system is the interaction with the gas phase; the intruder will be much larger than the size of a flow cell (i.e., the control volume for which the Navier-Stokes equations are solved), whereas the background particles will be much smaller. This calls for a hybrid approach, where the interactions of the large and small particles with the gas phase are handled differently. In this approach, the discrete particle model (DPM) is used for the description of all the 'background' (small) particles, insofar that it handles the collisions between the particles and performs the two-way coupling between the particles and the interstitial gas. DPM's typically handle particles with a diameter that is smaller than the size of a flow cell. Larger particles make that the control volume is devoid of gas, i.e., the void fraction is zero, and numerical problems are encountered. One way to overcome this problem is to smear out particle volumes over multiple flow cells, instead of using the volume-weighing method described in Chapter 2. Link *et al.* [15] used such a smearing method for the description of a spout-fluidized bed. In our application, the drawback of applying such a method to the intruder is that gas can still pas through areas that are - in a physical sense - completely occupied by the intruder, which is not realistic. Moreover, this unrealistic gas flow may very well influence the trajectories of the background particles, leading to different collisional behavior with the intruder. To overcome this problem, an additional model, namely the immersed boundary method (IBM), is used for the description of the gas-solid interaction of the intruder. In this method, the surface of the intruder is covered with so-called 'force points'. The local gas velocity at these force points is forced to be the local particle velocity (no-slip condition) and the amount of momentum (per unit volume) needed to enforce this condition is put into a source term for the momentum balance of the gas phase (see Chapter 2 for more details). In Appendix A, the implementation was verified by computing the terminal velocity of a falling sphere. It was found that, although the terminal velocity was slightly grid-dependent, the results are in good agreement with the experimental data of Schiller & Naumann [5], except for Reynolds numbers smaller than 1.

The implementation of the immersed boundary method in the flow solver is schematically depicted in Fig. 7.1. The forcing terms from the IBM are calculated explicitly and therefore, care must be taken in the selection of the time step used to integrate the Navier-Stokes equations. In the simulations for the terminal velocity of a single large intruder, with no background particles present we found that the local *gas* velocity at the force points was in good agreement with the local *particle* velocity, which is also reflected in the agreement between the terminal velocity and the experimental data of Schiller & Naumann. We next evaluate two cases to get insight in the behavior of the no-slip boundary condition in the presence of background particles. In the first case, an intruder was pulled through an empty column (in the presence of background fluidization from the gas inlet), where we used a time step of 5.10^{-5} s. In the second case, the intruder was pulled through a gas-fluidized bed, i.e., a bed with background particles present, operated just above minimum fluidization velocity, using the same time step. See Appendix B.

For the first case, we found that more than 90 % of the force points had a local gas velocity that was within 10 % of the desired value of -0.25 m/s. For the second

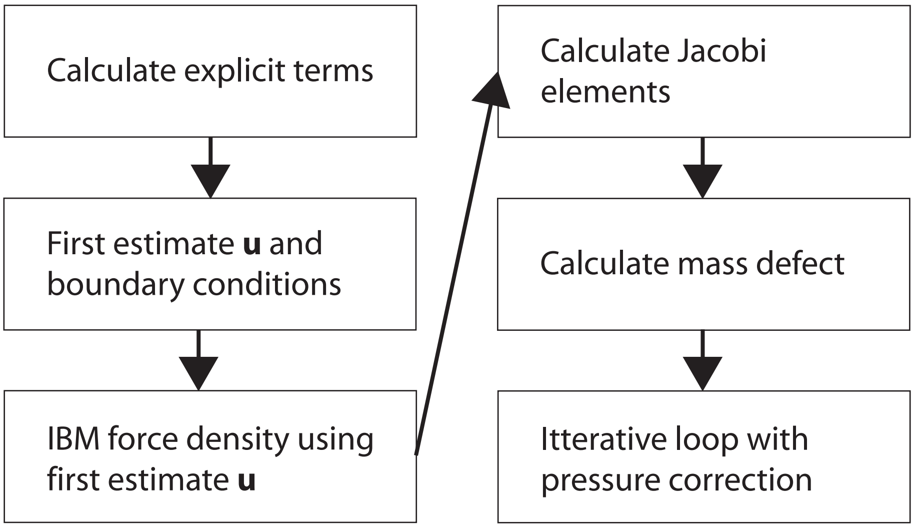

Figure 7.1: *Schematic overview of the flow solving procedure of the discrete particle model. Also included is the calculation for the immersed boundary method. As can be seen, the first estimates for the new gas velocities are used to determine the force densities required to obtain the no-slip boundary condition for the immersed boundary terms.*

case, we found that the local gas velocity deviated more than 100 % for 50 % of the force points. For computational efficiency, the smallest time step that should be chosen for solving the gas phase depends on the one used for integrating the equation of motion of the particles. In our particular case, this minimum time step was 2.10^{-6} s. When we used this value to re-evaluate the case, we found that 75 % of the force points had a deviation of less than 20 % from the desired local gas velocity of -0.25 m/s. The improvements are also obvious from Fig. 7.2, where the gas field looks more realistic.

It may be clear that the explicit treatment of the IBM forcing terms requires special attention when background particles are present. Most likely, the reason for the deviations is the presence of the source term **S** in the Navier-Stokes equations, which represents the effective momentum exchange of the discrete particles with the gas phase. Treating the IBM forcing semi-implicit did not alleviate the problem.

The accuracy of the no-slip boundary condition may be improved by (i) grid refinement, (ii) making the calculation of the IBM forcing terms implicit and (iii) by decreasing the time step: if it is small enough, the effect of DPM forcing will be relatively small, allowing for better enforcement of the boundary condition and coupling to the external flow field.

Unfortunately, from a computational point of view, we cannot limitlessly increase the grid resolution and we therefore did not pursue this in the rest of the research. Most likely, local grid refinement can alleviate these problems.

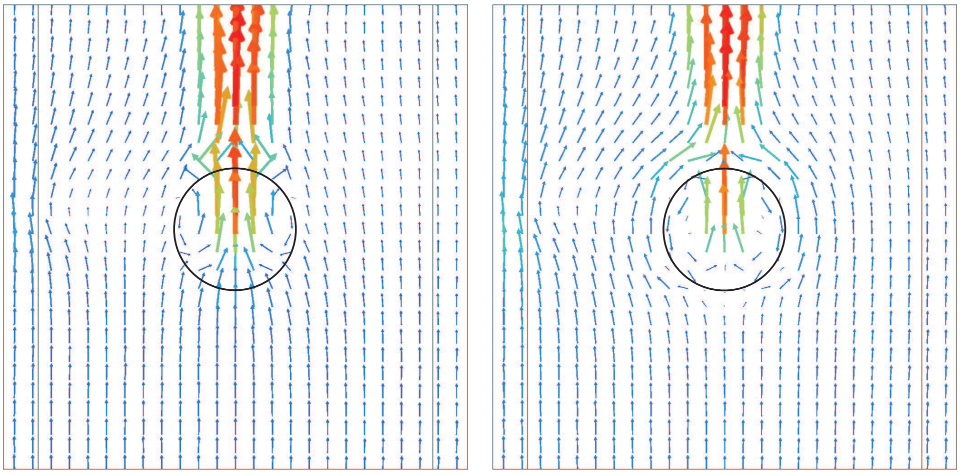

Figure 7.2: *Vector representation of the instantaneous gas velocities obtained by pulling a sphere through a fluidized granular bed (background particles not shown), with a constant velocity of -0.25 m/s. The grid size is 1.5 mm and the bed contains 1.4 million background particles. A channel-like structure of lower packing fraction is present behind the intruder and virtual internal circulation can be observed inside it. On the left-hand side we show the results from a simulation with time step of* 5.10^{-5} *s. It can be seen that the gas is flowing toward the sphere surface instead of flowing around it. On the right-hand side the result for a time step of* 2.10^{-6} *s. For this case, the gas field looks more realistic, which is also reflected in the percentage of force points that satisfy the no-slip boundary condition, as shown in Appendix B.*

7.3 Literature overview for the granular viscosity

We now present a short literature overview on experimental methods used to determine the granular viscosity. We pay special attention to typical values of the viscosity for particles with a diameter of 500 μm, which we use in our simulations.

Most researchers have employed intrusive measurement techniques to study the granular viscosities, inspired by the analogy with conventional fluids. Kai *et al.* [14] have catalogued these methods as follows.

- ‘Paddle’-type of methods where a paddle is immersed in the fluidized bed. A measure for the viscosity can be obtained from the torque that is required to keep the paddle rotating with a certain fixed angular velocity. This method has been employed by Kramers [6] and Shuster *et al.* [7].

- Couette-type viscometers. When such a viscometer is used in liquids, the gap between the two vertical coaxial cylinders is filled with the liquid of interest. The inner cylinder is suspended by a torsion wire and the outer cylinder is rotated at a constant rate. Momentum transfer via the liquid to the inner cylinder results in a torque which can be measured by the twist of the torsion

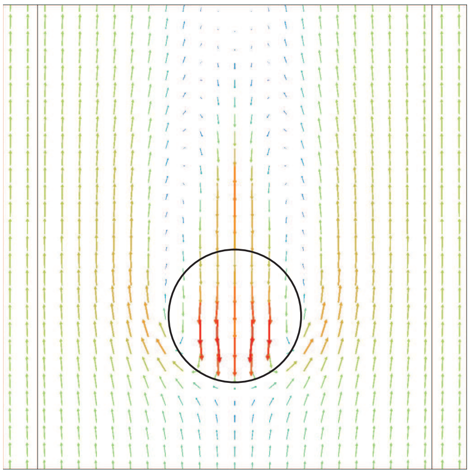

Figure 7.3: *As in Fig. 7.2, but for a sphere being pulled through an empty column (with a background gas flow). A time step of* 5.10^{-5} *s was used. The figure shows gas flowing around the sphere and a wake has been developed behind it. Such a wake is absent in Fig. 7.2, due to the presence of the particles.*

wire. This method was employed by Schügerl *et al.* [8, 9].

- Falling sphere. The terminal velocity of a falling sphere is used to estimate the granular viscosity, used by Daniels [10], King *et al.* [13] and Kai *et al.* [14].
- Torsion pendulum. A method used by Hagyard *et al.* [11], employs a torsion pendulum. This construct consists of a cylindrical body which is partially immersed in the fluidized bed and suspended by a vertical torsion wire. The immersed body is given a momentary impulse to start it oscillating torsionally about its vertical axis; the rate of decay of amplitude of oscillation was measured and converted directly into viscosity units through the use of a correlation function that was determined previously.

We will now discuss the trends and observations found in literature, and report the viscosity values found for glass particles with 500 μm diameter. Schügerl *et al.* [9], using a Couette-type viscometer, found that the granular viscosity for 500 μm glass particles varied between 1.2 and 5 Pa.s, depending on the applied gas velocity. Hagyard *et al.* [11], using a torsion pendulum, observed that at high gas velocities, the granular viscosity is practically independent of the particle diameter and gas velocity. Both found that the viscosity increases for low gas velocities, which was confirmed by others [6, 7, 10]. Grace [12] estimated the granular viscosity using an empirical approach based on the shape of spherical-cap bubbles rising in conventional liquids. He suggests that the granular viscosity might be non-isotropic, since the velocities in the vertical direction are larger than the horizontal ones. He found a viscosity of 0.95 Pa.s for 530 μm ballotini. King *et al.* [13]

investigated the granular viscosity as a function of operating pressure and found that it decreased significantly for particles smaller than 100 μm when the pressure was increased. However, pressure increase had little effect for larger particles. For 475 μm glass particles, he found a granular viscosity of 2.2 Pa.s. Grace [12] and Kramers [6] warn against the use of intrusive measurement techniques in fluidized bed, since voidage effects can influence the measurements. Kramers goes even further by saying that '*even under carefully specified conditions, no definite physical properties can be ascribed to a bed of fluidized solids because it is essentially non-homogeneous and non-uniform. In this respect it has nothing in common with the liquid state.*' [6].

From the above, it becomes clear that determining a granular viscosity for gas-fluidized beds is non-trivial and there are many variables that affect the obtained values. In the next sections we investigate the possibility of obtaining such information from a discrete particle model, where in principle many parameters can be controlled, which is nigh impossible to do in experiments.

To this end we will employ a method which is similar to the (experimental) falling sphere method for determining the emulsion 'drag' force. The new, hybrid DPM-IBM method makes it possible to solve the gas-phase dynamics when studying particle species with large size differences. Since the number of particles in our simulations is limited to approximately 1.4 million, our fluidized bed is of limited size. It is therefore not feasible to determine the terminal velocity and instead, we will directly measure the forces experienced by a sphere that is pulled through the granular bed with a constant (small) velocity.

7.4 Drag force simulations

In this section we will treat the details of the simulations, performed for determining the emulsion 'drag' force (having a contribution from the gas drag and particle collisions) acting upon an intruder being pulled through a gas-fluidized bed.

The simulation box, which has a size of $5 \times 5 \times 12$ cm, is filled with 1.4 million background particles with 250 μm radius and density $\rho_p = 2500$ kg/m^3 (average bed height 6 cm). A narrow Gaussian size distribution ($\sigma = 10$ μm) in the radius was used. The intruder possessed a radius of 5 mm and the same density as the background particles. The normal and tangential spring stiffness were set to 2000 and 571 N/m, respectively. In this preliminary study, we did not further investigate the sensitivity of the results with regards to these parameters. Instead of the volume-weighing technique, we used the technique of Link *et al.* [15] to distribute the background particle properties, such as particle volume and drag force, to the Eulerian grid. This makes the properties grid independent and allows us to use smaller grids. We performed our impact simulations for three grid sizes, namely 2.0, 1.5 and 1.0 mm cubed, in order to assess the grid dependence of the forces acting upon the intruder. The simulation allows us to measure the contact force F_{cont} and the gas force F_{gas} separately.

We want the fluidized bed to be as homogeneous as possible, effectively suppressing bubble formation, so that the forces acting upon the intruder will remain more or less constant. To this end, we fluidize near minimum fluidization and use perfectly elastic particles ($e_n = e_t = 1.0$), which is known to enhance homogeneous flow structures [16]. The shear viscosity μ_g, average pressure P, and density ρ_g of the gas were set to match the properties of air at ambient conditions: $\mu_g = 1.8 \times 10^{-5}$ Pa.s, $P = 1$ bar, and $\rho_g = 1.2$ kg/m^3. The bed was fluidized for 0.8 s with the intruder immmersed in the bed, using a gas velocity of 0.19 m/s, which is just above minimum fluidization velocity.

The intruder particle (being 20 times larger than the background particles) was pulled through the granular bed with a constant velocity (v_p) which was set to values 0.100 m/s, 0.125 m/s, 0.150 m/s and 0.175 m/s. We can make an estimate of the maximum Reynolds number in the fluidized bed:

$$\mathrm{Re} = \frac{\rho_{gran} v_p d_p}{\mu_{gran}} = \frac{1500 \times 0.175 \times 0.01}{1.0} = 2.6 \tag{7.1}$$

Here, we choose the suspension density ρ_{gran} of the granular bed as $0.6 \times \rho_p = 0.6 \times 2500 = 1500$ kg/m^3, where 0.6 is the approximate packing fraction of the fluidized bed. Further, we assume that the granular viscosity (μ_{gran}) is equal to 1.0 Pa.s, which is the order of magnitude reported in literature. If the relation between force and intruder velocity is linear, this would indicate that we can use the Stokes-Einstein drag law to estimate the granular viscosity:

$$\mathrm{F} = 3\pi \mu_{gran} d_p v_p \tag{7.2}$$

7.5 Results

In this section, we describe the findings for the simulations where the intruder was pulled through the granular bed. A series of snapshots is presented in Fig. 7.4. We tested four different intruder velocities (v_{int}) and for each of these, three grid sizes were tested, namely 1.0, 1.5 and 2.0 mm cubed. We are interested in the gas force (F_{gas}) and contact force (F_{cont}) acting upon the intruder, where we only consider the forces in the vertical direction. Note that we show a moving time-average of F_{cont}, in order to average out the fluctuations in this force. The findings for $v_{int} = 0.100$ and 0.175 m/s are shown in Fig. 7.5. It is apparent that a grid effect is present: (i) F_{gas} *decreases* with decreasing grid size, while F_{cont} *increases* with decreasing grid size, and (ii) while F_{gas} seems to be nearly constant with depth, the F_{cont} increases with depth. Observation (i) is most likely due to changes in the gas flow field connected to the increased resolution for smaller grid sizes, which causes the particle trajectories and thus collisional interaction to proceed differently. An explanation for (ii) is that due to the relatively large v_{int} (i.e., 0.175 m/s) the particles underneath the intruder are not easily displaced to the sides. It is not an added mass effect, however, since the intruder does not accelerate. Instead, it is expected that it is a stagnation effect which increases as the intruder approaches the bottom: an intruder moving with high velocity will have a densified zone of particles in front

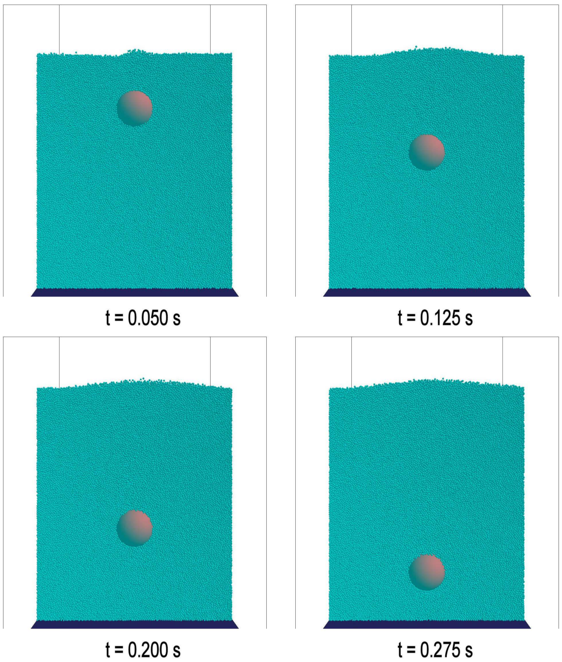

Figure 7.4: *A cut through the fluidized bed, showing an intruder moving through the fluidized bed with velocity 0.150 m/s.*

of it. This explanation is confirmed by $v_{int} = 0.125$ and 0.100 m/s, since there F_{cont} is more or less depth independent (see also Fig. 7.9, Appendix C), most likely since the particles beneath the intruder have more time to move aside.

We next compare the effect of v_{int} on F_{gas} and F_{cont}. For all investigated grid sizes, it was found that F_{gas} was more or less independent of v_{int} and depth. By contrast, F_{cont} was strongly dependent on v_{int}, as expected. See Fig. 7.9 in Appendix C.

We determined the size of F_{cont} exerted on the intruder as a function of v_{int}. Unfortunately, for larger values of v_{int} (0.150 and 0.175 m/s) this force was found to become increasingly depth dependent for reasons mentioned earlier. For $v_{int} = 0.100$ and 0.125 m/s, F_{cont} is approximately constant with depth and, although depth dependent, also an estimate for F_{cont} was made for intruder velocity 0.150 m/s. Doing so for each grid size yielded the results as visualized in Fig. 7.6. We performed a similar analysis where we used the sum of F_{cont} and F_{gas} acting upon the intruder, instead of only F_{cont} (not shown here). The viscosities so obtained are summarized in table 7.1. Granular viscosities in the range of 0.6-0.9 Pa.s are found, which is close to the findings from literature. The associated Reynolds number is approximately 3.

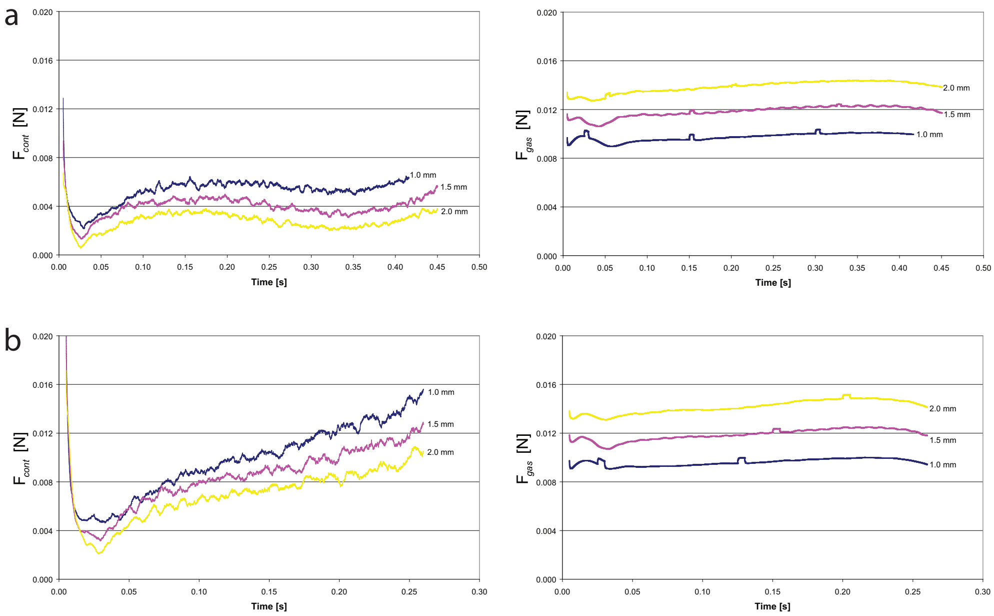

Figure 7.5: *F_{cont} (left-hand side) and F_{gas} (right-hand side) acting upon an intruder, as a function of the grid size. Figure a) shows the results for $v_{int} = 0.100$ m/s and figure b) the results for $v_{int} = 0.175$ m/s.*

7.6 Conclusion

We have explored the feasibility of combining a discrete particle model (DPM) with an immersed boundary method (IBM) approach for the description of a large sphere in the presence of assemblies of much smaller ones. The implementation of the IBM was verified by investigating the terminal velocity of a falling sphere in an empty column and it was found that the results agreed well with the findings of Schiller & Naumann, with a slight grid dependence. In a gas-fluidized bed, however, the gas force acting upon the large sphere was unusually large due to the presence of the background particles.

Despite the problems with the implementation, we have performed a first application of the model by measuring the granular viscosity of a granular bed, where the effect of the grid size was investigated by using three different grid sizes. In the simulations, an intruder was pulled with constant velocity v_{int} through a granular bed at minimum fluidization and the forces F_{cont} and F_{gas} resulting from the collisions with the background particles and from the interaction with the gas phase, respectively, were measured. Assuming a Stokes-Einstein drag law for F_{cont} as a function of the velocity v_{int}, a granular viscosity was obtained, which was found to be in the range of 0.6-0.9 Pa.s. This is close to the values reported in literature. Apart from necessary improvements in the implementation of the hybrid DPM-

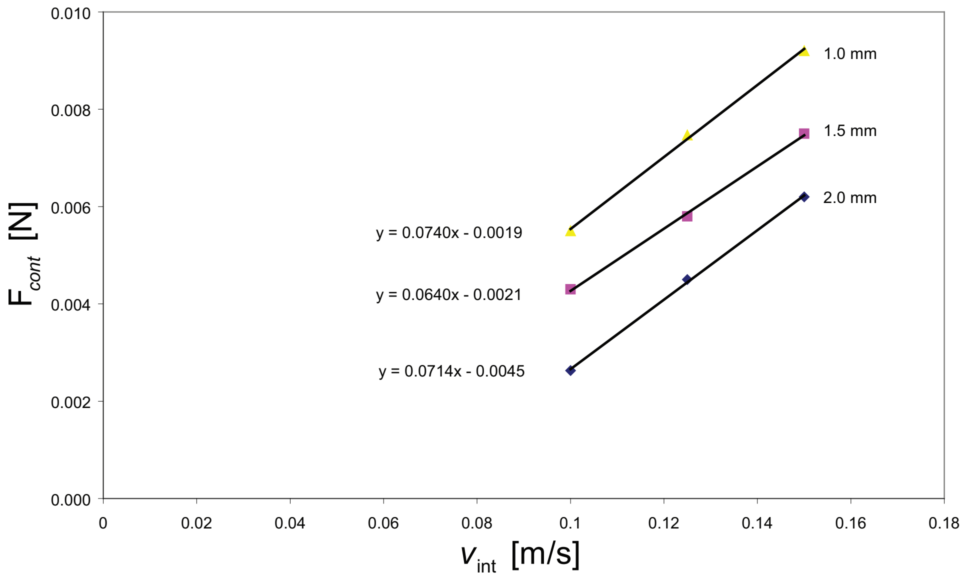

Figure 7.6: *F_{cont} vs. v_{int} for the three different grid sizes. According to the Stokes-Einstein law (Eq. 7.2), the slope corresponds to $3\pi\mu_{gran}d_p$ and thus, an estimate of μ_{gran} can be obtained.*

	1.0 mm		**1.5 mm**		**2.0 mm**	
$\mathbf{F}_{cont}$	0.76	(0.79)	0.68	(0.64)	0.79	(0.84)
$\mathbf{F}_{cont} + \mathbf{F}_{gas}$	0.59	(0.72)	0.64	(0.85)	0.64	(0.64)

Table 7.1: *μ_{gran} as obtained from a plot of F_{cont} vs. v_{int}, see Fig. 7.6. The data of $v_{int} = 0.100$, 0.125 and 0.150 m/s were used. For the values in parenthesis, only 0.100 and 0.125 m/s were used.*

IBM model, one could further investigate the effect of the box dimensions and the intruder diameter, the effect of collision properties and the effect of the homogeneity of the granular bed. To avoid grid effects in the IBM forcing, as observed in Fig. 7.8 in Appendix A, one could choose to use a distribution function different from linear, which is currently used.

Eventually, it would be very interesting to study the performance of the model for the description of the Reverse Brazil Nut effect as observed by Möbius *et al.*, who found that the interstitial air played a crucial role in whether the Brazil Nut would moved to the top or would sink.

Appendix A: Terminal velocity

We tested the performance of the IBM by measuring the terminal velocity ($\mathrm{v}_{\mathrm{term}}$) of a falling sphere. We did so for three situations. Firstly, we tested the result for a single sphere falling through an empty column, where we use linear interpolation (volume-weighing) to determine the local gas velocity at the force points. Secondly, we test a single falling sphere, but now using cubic spline-interpolation (3rd order accurate) [17] to determine the local gas velocity. Thirdly, we studied the effect of the number of force points used to describe the sphere surface. The results can be found in tables 7.2 to 7.4.

The terminal velocity of falling spheres in an empty column at different Re numbers was compared to the results obtained when using the empirical drag relation of Schiller & Naumann [5]. The force balance of the particle takes the form:

$$\mathrm{F}_{\mathrm{gas}} + \mathrm{F}_{\mathrm{buoy}} + \mathrm{F}_{\mathrm{grav}} = 0 \tag{7.3}$$

where

$$\mathrm{F}_{\mathrm{buoy}} + \mathrm{F}_{\mathrm{grav}} = \frac{1}{6}\pi d_p^3 g \left(\rho_g - \rho_p\right) \tag{7.4}$$

and

$$\mathrm{F}_{\mathrm{gas}} = c_w \left(\frac{1}{4}\pi d_p^2\right)\left(\frac{1}{2}\rho_g v_{\mathrm{inf}}^2\right) \quad \text{with} \quad c_w = \frac{24}{\mathrm{Re}}\left(1 + 0.15\mathrm{Re}^{0.687}\right) \tag{7.5}$$

We found that $\mathrm{v}_{\mathrm{term}}$ obtained in the simulations was in good agreement with the one obtained from the force balance, usually within 5 %. However, for low Re numbers ($\mathrm{Re} < 1$), it was found that $\mathrm{v}_{\mathrm{term}}$ could deviate strongly, namely up to 25 %. This effect may be caused by the limited size of our simulation box, which makes that the side walls play a dominant role (which is especially important at relatively large values of the viscosity). In all cases, we found that the results were grid dependent (see Fig. 7.7). The effect of the time step was found to be minimal (see table 7.3). From the simulation results it was found that the grid dependence was not caused by the type of gas velocity interpolation (linear or spline). It is rather expected that the distribution of the IBM forcing (see Eq. 2.41 in Chapter 2) is the cause, since its distance changes linearly with the grid. We did not further test this, however. We also investigated the effect of using an increased number of force points for the description of the intruder surface (table 7.4), but found that it did not change the results. Finally, we observed small fluctuations in the terminal gas drag force, see Fig. 7.8. The fluctuations are connected to the grid size and we expect that an other distribution method for the IBM forcing will alleviate this.

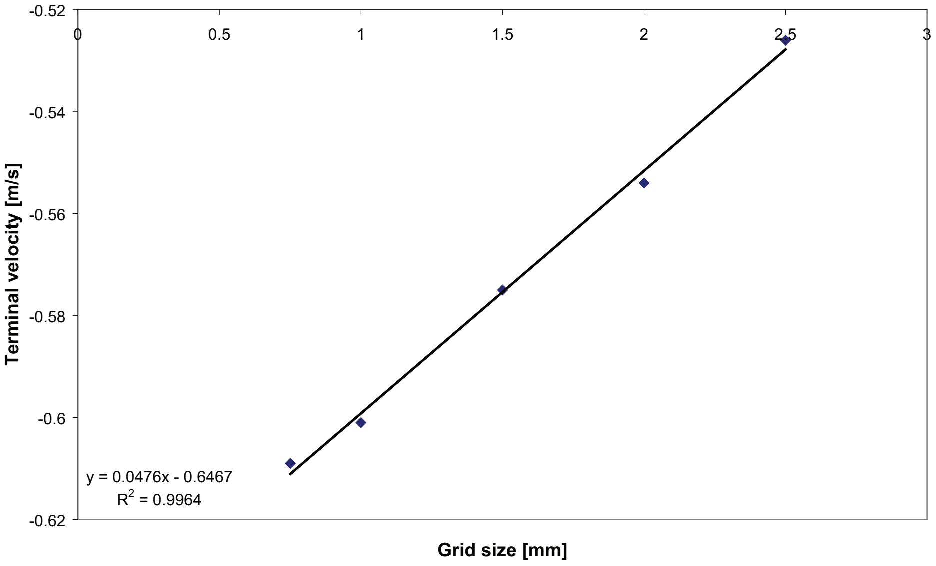

Figure 7.7: *Linear grid dependence of the terminal velocity. The terminal velocity results for the case of* $\mathrm{Re}_{\mathrm{inf}} = 24.9$ *are plotted, see table 7.3.*

Case	$\mathrm{Re}_{\mathrm{inf}}$	$\mathrm{v}_{\mathrm{inf}}$	$\mathrm{v}_{\mathrm{term}}$	dev [%]	$\Delta x = \Delta y = \Delta z$	DT	ρ_g	ρ_p	NX	NY	NZ	nodes
1	0.58	-0.488	-0.378	22.5	$1.5.10^{-3}$	$2.5.10^{-5}$	1.2	100	40	40	240	728
2	0.58	-0.488	-0.391	19.9	$1.0.10^{-3}$	$1.0.10^{-5}$	1.2	100	60	60	180	1442
3	0.58	-0.488	-0.397	18.6	$7.5.10^{-4}$	$6.0.10^{-6}$	1.2	100	80	80	240	2916
4	12.4	-0.519	-0.484	6.7	$1.5.10^{-3}$	$1.0.10^{-4}$	23.9	200	40	40	240	728
5	12.4	-0.519	-0.507	2.3	$1.0.10^{-3}$	$1.0.10^{-4}$	23.9	200	60	60	200	1442
6	24.9	-0.594	-0.561	5.6	$1.5.10^{-3}$	$2.0.10^{-4}$	41.9	300	40	40	240	728
7	24.9	-0.594	-0.592	0.3	$1.0.10^{-3}$	$2.0.10^{-4}$	41.9	300	60	60	300	1442
8	41.0	-0.622	-0.594	4.5	$1.5.10^{-3}$	$2.0.10^{-4}$	65.9	400	40	40	240	728
9	41.0	-0.622	-0.632	-1.6	$1.0.10^{-3}$	$2.0.10^{-4}$	65.9	400	60	60	300	1442
10	60.2	-0.628	-0.605	3.7	$1.5.10^{-3}$	$2.0.10^{-4}$	95.8	500	40	40	240	728

Table 7.2: *Different conditions for determining the terminal velocity, where we used linear interpolation to obtain the gas velocity at the force points.* $\mathrm{Re}_{\mathrm{inf}}$ *and* $\mathrm{v}_{\mathrm{inf}}$ *are the terminal Reynolds number [-] and particle velocity [m/s] on basis of the force balance.* $\mathrm{v}_{\mathrm{term}}$ *is the terminal velocity obtained from the simulation.* $\Delta x, \Delta y, \Delta z$ *are the dimensions of the flow cells [m] and DT is the time step of the simulation [s].* ρ_g *and* ρ_p *are the density of the gas and particle, respectively [kg/m*^{3}*]. NX, NY and NZ are the number of cells in the different directions and 'nodes' is the number of Lagrangian force points located on the sphere surface. In all cases, the dynamic gas viscosity* μ_g *was 0.01 Pa.s and the molecular mass of air (28.8.10*$^{-3}$ *kg/mol) was used. Different gas pressures were used to obtain the used gas densities. The intruder had a diameter of 10 mm.*

Case	$\mathrm{Re}_{\mathrm{inf}}$	$\mathrm{v}_{\mathrm{inf}}$	$\mathrm{v}_{\mathrm{term}}$	dev [%]	$\Delta x = \Delta y = \Delta z$	DT	ρ_g	ρ_p	NX	NY	NZ	nodes
1	12.4	-0.519	-0.462	11.0	$2.5.10^{-3}$	$1.0.10^{-4}$	23.9	200	24	24	180	254
2	12.4	-0.519	-0.482	7.1	$2.0.10^{-3}$	$1.0.10^{-4}$	23.9	200	30	30	225	386
3	12.4	-0.519	-0.498	4.0	$1.5.10^{-3}$	$1.0.10^{-4}$	23.9	200	40	40	300	728
4	12.4	-0.519	-0.516	0.6	$1.0.10^{-3}$	$1.0.10^{-4}$	23.9	200	60	60	450	1442
5	24.9	-0.594	-0.526	11.4	$2.5.10^{-3}$	$2.0.10^{-4}$	41.9	300	24	24	144	244
6	24.9	-0.594	-0.554	6.7	$2.0.10^{-3}$	$2.0.10^{-4}$	41.9	300	30	30	180	386
7	24.9	-0.594	-0.575	3.2	$1.5.10^{-3}$	$2.0.10^{-4}$	41.9	300	40	40	240	728
8	24.9	-0.594	-0.601	-1.2	$1.0.10^{-3}$	$2.0.10^{-4}$	41.9	300	60	60	360	1442
9	24.9	-0.594	-0.609	-2.5	$7.5.10^{-4}$	$2.0.10^{-4}$	41.9	300	80	80	360	1906
10	41.0	-0.622	-0.608	2.3	$1.5.10^{-3}$	$2.0.10^{-4}$	65.9	400	40	40	240	728
11	41.0	-0.622	-0.607	2.4	$1.5.10^{-3}$	$1.0.10^{-4}$	65.9	400	40	40	240	728
12	41.0	-0.622	-0.606	2.6	$1.5.10^{-3}$	$5.0.10^{-5}$	65.9	400	40	40	240	728
13	41.0	-0.622	-0.605	2.7	$1.5.10^{-3}$	$2.5.10^{-5}$	65.9	400	40	40	240	728
14	41.0	-0.622	-0.640	-2.9	$1.0.10^{-3}$	$2.0.10^{-4}$	65.9	400	60	60	300	1442
15	60.2	-0.628	-0.619	1.4	$1.5.10^{-3}$	$2.0.10^{-4}$	95.8	500	40	40	240	728

Table 7.3: *As in table 7.2, but using spline interpolation to obtain the gas velocity at the force points. As can be seen, the results were only marginally better than those obtained from using linear velocity interpolation.*

Case	$\mathrm{Re}_{\mathrm{inf}}$	$\mathrm{v}_{\mathrm{inf}}$	$\mathrm{v}_{\mathrm{term}}$	dev [%]	$\Delta x = \Delta y = \Delta z$	DT	ρ_g	ρ_p	NX	NY	NZ	nodes
1	24.9	-0.594	-0.525	11.6	$2.5.10^{-3}$	$2.0.10^{-4}$	41.9	300	24	24	144	15002
2	24.9	-0.594	-0.553	6.9	$2.0.10^{-3}$	$2.0.10^{-4}$	41.9	300	30	30	180	15002
3	24.9	-0.594	-0.576	3.0	$1.5.10^{-3}$	$2.0.10^{-4}$	41.9	300	40	40	240	15002
4	24.9	-0.594	-0.600	-1.0	$1.0.10^{-3}$	$2.0.10^{-4}$	41.9	300	60	60	360	15002
5	24.9	-0.594	-0.525	11.6	$2.5.10^{-3}$	$2.0.10^{-4}$	41.9	300	24	24	144	1946
6	24.9	-0.594	-0.553	6.9	$2.0.10^{-3}$	$2.0.10^{-4}$	41.9	300	30	30	180	1946
7	24.9	-0.594	-0.576	3.0	$1.5.10^{-3}$	$2.0.10^{-4}$	41.9	300	40	40	240	1946
8	24.9	-0.594	-0.600	-1.0	$1.0.10^{-3}$	$2.0.10^{-4}$	41.9	300	60	60	360	1946

Table 7.4: *The effect of an increased number of force points on the sphere surface. The results are the same as the cases where we used a smaller number of force points. Spline interpolation was used to determine the local gas velocity.*

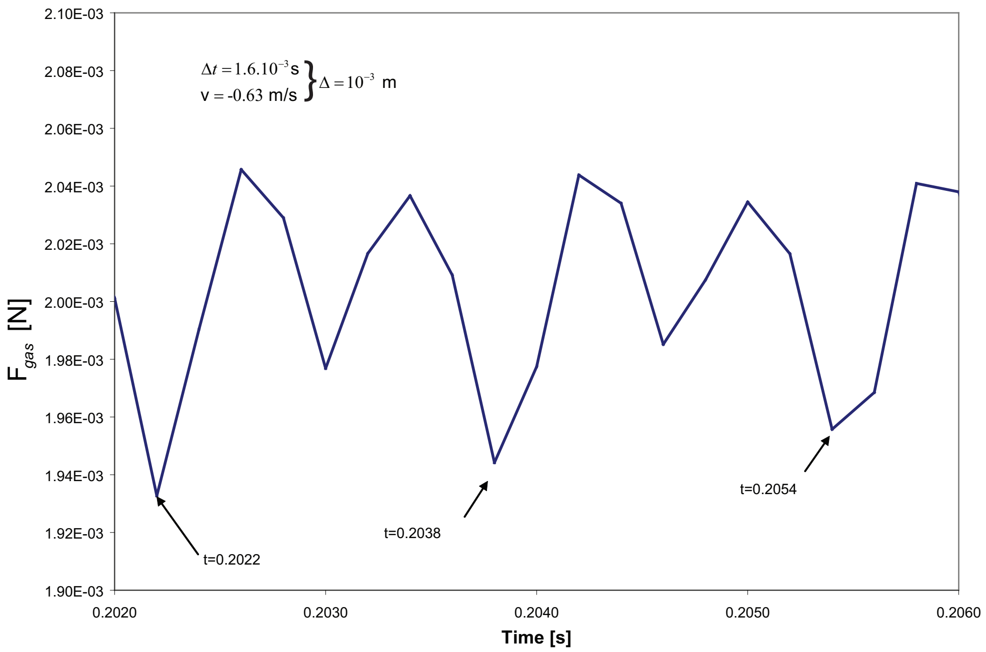

Figure 7.8: *Transient behavior of the vertical gas drag force acting upon the particle as in Case 9, table 7.2. As can be seen, small oscillations around the stationary gas force are present. When multiplying the time span of the oscillations (1.6.10^{-3} s) with the particle velocity (-0.63 m/s), we found the distance to be 10^{-3} m which is the grid size. This shows that the fluctuations are caused by the mapping method of the forcing terms, namely linear interpolation.*

Appendix B: Accuracy at the force points

The accuracy of the local gas velocity at the force points was investigated, since the explicit implementation of the IBM forcing does not guarantee that the no-slip boundary condition is satisfied. To this end, we calculated this velocity (which is obtained via linear interpolation of the surrounding eight velocity nodes) *after* the flow field had converged. The surface of the intruder was covered with 728 force points and we evaluate the local gas velocity for each of these points for the duration of 43 computational cycles. We then determined the relative deviation from the desired velocity (namely the local particle velocity) for all the force points and constructed a histogram to evaluate the results. Three different cases were investigated: (i) pulling an intruder through an empty column, using a time step of 5.10^{-5} s, (ii) pulling the intruder through a gas-fluidized bed containing background particles using a time step of 5.10^{-5} s and (iii) the same as (ii) but now with a time step of 2.10^{-6} s. The results of the cases can be found in table 7.5.

dev [%]	cnt [-]	cum [%]
0 - 1	3649	16.2
1 - 2	2809	28.6
2 - 3	2245	35.6
3 - 4	2748	50.9
4 - 5	2438	61.7
5 - 6	1933	70.3
6 - 7	1690	77.8
7 - 8	1166	82.9
8 - 9	1124	87.9
9 - 10	762	91.3
more	1968	100

dev [%]	cnt [-]	cum [%]
0 - 20	6189	19.8
20 - 40	3148	29.8
40 - 60	2926	39.1
60 - 80	2028	45.7
80 - 100	1547	50.6
100 - 120	1687	56.0
120 - 140	1810	61.8
140 - 160	2161	68.7
160 - 180	871	71.5
180 - 200	1562	76.4
more	7375	100

dev [%]	cnt [-]	cum [%]
0 - 10	14110	45.1
10 - 20	9624	75.8
20 - 30	3934	88.4
30 - 40	1700	93.8
40 - 50	956	96.9
50 - 60	897	99.7
60 - 70	83	100
70 - 80	0	100
80 - 90	0	100
90 - 100	0	100
more	0	100

Table 7.5: *Three cumulative histograms indicating the deviation from the no-slip boundary condition at the force point locations for the duration of 43 time steps. From left to right: (i) a sphere being pulled through an empty column with background fluidization (time step is* 5.10^{-5} *s), (ii) a sphere being pulled through a fluidized bed in the presence of background particles (time step is* 5.10^{-5} *s) and (iii) as in (ii) but with a time step is* 2.10^{-6} *s. The deviation of the gas velocity at the surface of the intruder from the desired value is plotted in the first column, the number of counts in the second and the cumulative percentage in the third. As can be seen, the accuracy of the calculation is reasonable for (i). For (ii) the data already shows that the accuracy is insufficient, where half of the force points have a deviation of 100 % or more. For (iii) the accuracy has much improved, compared to the one in (ii): 75 % of the force points is within 20 % of the accurate value.*

As can be seen, the results for the intruder in an empty column (case (i)) are acceptable. However, the results for the intruder immersed in a fluidized bed (case (ii)) show that there is a significant deviation between the desired and the actual flow field. The agreement becomes significantly better, however, when the time step is decreased to 2.10^{-6} s (case (iii)). The effect is attributed to the explicit treatment of the IBM forcing terms.

Appendix C: Gas and contact forces

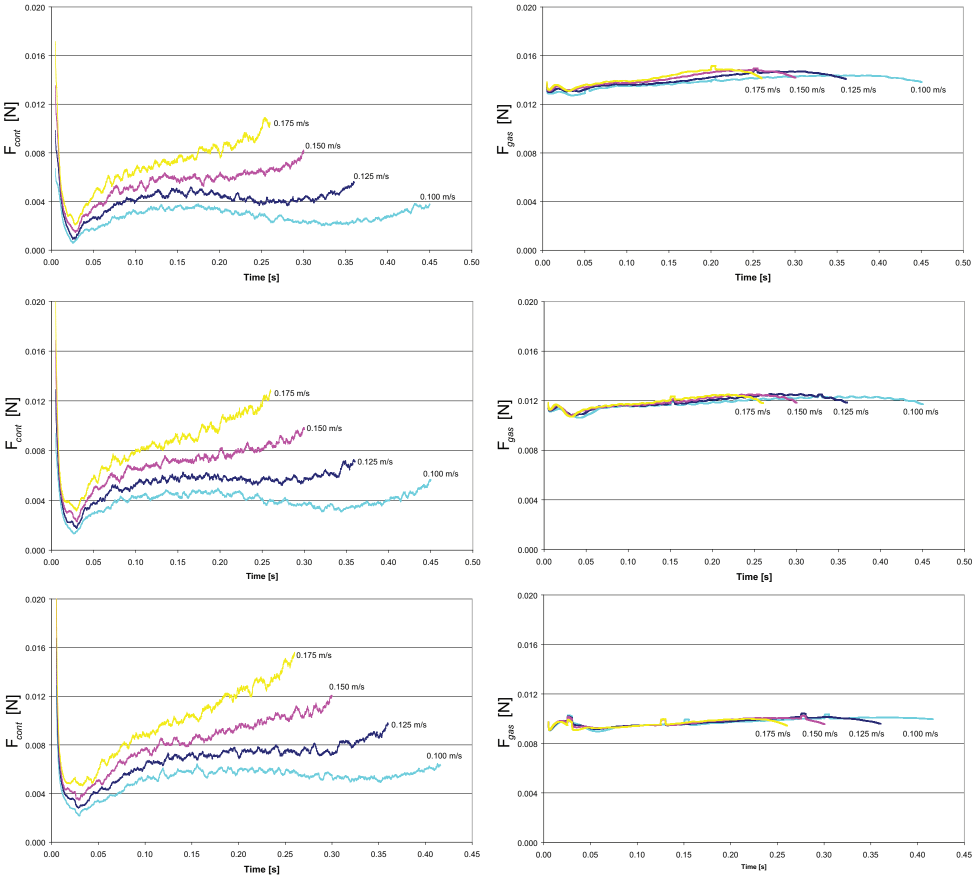

Figure 7.9: *The figure summarizes the findings for the 2.0 mm (top), 1.5 mm (middle) and 1.0 mm (bottom) grids. On the left-hand side,* F_{gas} *and on the right-hand side* F_{cont} *acting upon an intruder, for the four tested velocities. As expected,* F_{cont} *increases with velocity.* F_{gas} *seems velocity independent, which is not realistic.*

Bibliography

[1] J.R. Royer, E.I. Corwin, A. Flior, M-L. Cordero, M. Rivers, P. Eng, H.M. Jaeger, 'Formation of Granular Jets Observed by High-Speed X-ray Radiography', Nature Physics **1**, p. 164 (2005).

[2] C.S. Peskin, 'The immersed boundary method', Acta Numerica **11**, p. 480 (2002).

[3] M. Uhlmann, 'An immersed boundary method with direct forcing for the simulation of particulate flows', J. Comp. Phys. **209**, p. 448 (2005).

[4] M.E. Möbius, B.E. Lauderdale, S.R. Nagel, H.M. Jaeger, 'Size separation of granular particles', Nature **414**, p. 270 (2001).

[5] L. Schiller, A. Naumann, Z. Ver. dtsch. Ing. **77**, p. 318 (1933).

[6] H. Kramers, 'On the "Viscosity" of a bed of fluidized solids', Chem. Eng. Sci. **1**, p. 35 (1951).

[7] W.W. Shuster, F.C. Haas, 'Point viscosity measurements in a fluidized bed', J. Chem. Eng. Data **5**, p. 525 (1960).

[8] K. Schügerl, M. Merz, F. Fetting, 'Unregelmässiges Verhalten von Fliessbettsystemen bei rheologischen Messungen', Chem. Eng. Sci. **15**, p. 75 (1961).

[9] K. Schügerl, M. Merz, F. Fetting, 'Rheologische Eigenschaften von gasdurchströmten Fliessbettsystemen', Chem. Eng. Sci. **15**, p. 1 (1961).

[10] T.C. Daniels, 'Measurement of the Drag on Immersed Bodies in Fluidised beds', Rheologica Acta **4**, p. 192 (1965).

[11] T. Hagyard, A.M. Sacerdote, 'Viscosity of suspensions of gas-fluidized spheres', Ind. Eng. Chem. Fundam. **5**, p. 500 (1966).

[12] J.R. Grace, 'The Viscosity of Fluidized Beds', Can. J. Chem. Eng. **48**, p. 30 (1970).

[13] D.F. King, F.R.G. Mitchell, D. Harrison, 'Dense Phase Viscosity of Fluidised Beds at Elevated Pressures', Powd. Tech. **28**, p. 55 (1981).

[14] T. Kai, M. Murakami, K. Yamasaki, T. Takahashi, 'Relationship between apparent bed viscosity and fluidization quality in a fluidized bed with fine particles', J. Chem. Eng. Japan **24**, p. 494 (1991).

[15] J.M. Link, L.A. Cuypers, N.G. Deen, J.A.M. Kuipers, 'Flow regimes in a spout-fluid bed: A combined experimental and simulation study', Chem. Eng. Sci. **60**, p. 3425 (2005).

[16] J. Li, J.A.M. Kuipers, 'Effect of competition between particle-particle and gas-particle interactions on flow patterns in dense gas-fluidized beds', Chem. Eng. Sci. special issue: Frontiers in Chemical Engineering - Multi-scale bridge between reductionism and holism, in press (2007).

[17] See Numerical Recipes in C, at www.nr.com.

List of Publications

1. J.M. Link, C. Zeilstra, N.G. Deen, J.A.M. Kuipers, ‘Validation of a Discrete Particle Model in a 2D Spout-Fluid bed using non-intrusive optical measuring techniques’, Can. J. Chem. Eng. **82**, p. 30 (2004).
2. D. Lohse, R. Bergmann, R. Mikkelsen, C. Zeilstra, D. van der Meer, M. Versluis, K. van der Weele, M. van der Hoef, J.A.M. Kuipers, ‘Impact on soft sand: Void collapse and jet formation’, Phys. Rev. Lett **93**, 198003 (2004).
3. G. Finnie, N.P. Kruyt, M. Ye, C. Zeilstra and J.A.M. Kuipers, ‘Longitudinal and transverse mixing in rotary kilns: a discrete element method approach’, Chem. Eng. Sci. **60**, p. 4083 (2005).
4. C. Zeilstra, M.A. van der Hoef, J.A.M. Kuipers, ‘Simulation of Vibration-Induced Segregation of Equal-Sized Bronze and Glass Spheres’, WCPT5: Proceedings 5th World Congress on Particle Technology, 24-27 April 2006, Orlando, Florida, USA
5. C. Zeilstra, M.A. van der Hoef, J.A.M. Kuipers, ‘Simulation study of air-induced segregation of equal-sized bronze and glass particles’, Phys. Rev. E **74**, 010302 R (2006).
6. C. Zeilstra, M.A. van der Hoef, J.A.M. Kuipers, ‘Simulation of density segregation in vibrated beds’, in preparation.
7. C. Zeilstra, J.G. Collignon, M.A. van der Hoef, N.G. Deen, J.A.M. Kuipers, ‘Experimental and numerical study of wall-induced granular convection’, in preparation.
8. C. Zeilstra, M.A. van der Hoef, M. Van Sint Annaland, J.A.M. Kuipers, ‘Experimental and numerical study of solids circulation in gas-vibro fluidized beds’, in preparation.

Levensloop

Christiaan Zeilstra werd op 19 oktober 1977 geboren te Sneek. Hij groeide op in Scharnegoutum alwaar hij de lagere school heeft doorlopen. Hij bezocht hierna het Bogerman College te Sneek, waar hij is 1996 het VWO diploma behaalde.

In augustus 1996 begon hij aan de opleiding Chemische Technologie van de Universiteit Twente. In het kader van deze opleiding werd in het najaar van 2000 stage gelopen bij DOW Chemical in Terneuzen. In april 2002 studeerde hij af bij de werkeenheid Fundamentele Aspecten van de Proceskunde (FAP) op de verificatie en validatie van een computermodel voor pseudo-2D spout-fluïde bedden.

Na afloop van zijn studie trad hij in juni 2002 in dienst bij de werkeenheid FAP om als onderzoeker in opleiding een promotieonderzoek te verrichten op het gebied van stroming en segregatie in geschud granulair materiaal. De resultaten van het onderzoek staan beschreven in dit proefschrift.

Dankwoord

Het dankwoord is vaak het best gelezen onderdeel van een proefschrift. Dit is niet zozeer omdat de tekst voor de gemiddelde lezer toegankelijker zou zijn, maar vooral omdat men toch graag wil weten wie betrokken was bij de totstandkoming van het proefschrift. Het zal namelijk iedereen duidelijk zijn dat een proefschrift niet het werk is van één persoon, hoewel er maar één naam op de voorkant staat. Ik wil dan ook vanaf deze plek stilstaan bij de mensen die hierin direct en indirect een belangrijke rol hebben gespeeld.

Allereerst wil ik mijn promotor Hans Kuipers bedanken voor de mogelijkheid die hij mij heeft geboden om binnen zijn onderzoeksgroep Fundamentele Aspecten van de Proceskunde een promotieonderzoek uit te voeren. Ik heb altijd veel profijt gehad van jouw indrukwekkende kennis op het gebied van gas-vast systemen, zowel op modelmatig als op experimenteel vlak. Ik vind het mooi om te zien hoe veelzijdig het discrete deeltjes model - dat oorspronkelijk ontwikkeld was voor gas-gefluïdiseerde bedden - toegepast kan worden en ik denk dan ook dat het terecht als de 'work horse' van de gas-vast onderzoekslijn kan worden beschouwd. Het gestelde vertrouwen en de warme belangstelling heb ik altijd als zeer motiverend ervaren. Al met al kan ik zeggen dat ik tijdens het project veel heb geleerd en ik kijk er ook met veel plezier op terug.

Voor de directe begeleiding wil ik Martin van der Hoef ten zeerste bedanken; niet alleen voor de kritisch inhoudelijke inbreng, maar ook voor de taalkundige aanwijzingen. Ik kan zeggen dat mijn kennis van Engelse synoniemen een grote vlucht heeft genomen sinds de start van het project, wat vooral bij opsommingen goed van pas kwam ("First", "Then", "Next", "Following this", "Finally"). Om op het literair vlak te blijven: ik ben nog steeds zeer nieuwsgierig naar het plot van jouw 'Da Vinci Code' en hoop ooit het manuscript onder ogen te krijgen. Tevens wil ik graag Martin van Sint Annaland bedanken voor zijn inbreng op het modelleergebied (zowel DPM als IBM) en de mooie visualisatiesoftware. Niels Deen wordt bedankt voor zijn bijdrage op het gebied van de meettechniek Particle Image Velocimetry (PIV).

Verder wil ik Detlef Lohse, Devaraj van der Meer, Ko van der Weele en Raymond Bergmann van de onderzoeksgroep Physics of Fluids bedanken voor de samenwerking op het gebied van de granulaire jet. Hun impact experimenten demonstreerden op spectaculaire wijze de analogie tussen granulair materiaal en vloeistoffen. Tevens had de experimentele component van dit proefschrift niet gerealiseerd kunnen worden zonder het gebruik van hun 'shaker', waarbij ik Gert-Wim Bruggert en Peter Eshuis wil bedanken voor de tips en technische ondersteuning.

Ik ben de stichting FOM erkentelijk voor de financiering van het onderzoek en het NCF voor de rekentijd op de computerclusters van Sara te Amsterdam.

Voor het valideren van numerieke modellen is een goede experimentele opstelling een eerste vereiste. Dat de opstelling geschud ging worden, maakte dat de materiaalkeuze en constructie complexer was dan bij reguliere gefluïdiseerde bedden. Zonder de goed gekwalificeerde technici en de goed uitgeruste werkplaats die ons vakgroep nog rijk is, was dit zeker niet gelukt. Ik wil dan ook Wim Leppink en Robert Brouwer bedanken voor het vervaardigen van de granulaire convectie en gas-vibro fluïdisatie opstellingen, de bijbehorende randapparatuur en de support ervan. Tevens worden Gerrit Schorfhaar en Robert Meijer bedankt voor de diverse (ad-hoc) hand - en spandiensten. Voor het uitvoeren van de 'rekensommetjes' is een goed werkende numerieke opstelling noodzakelijk. Dadan Darmana, Robert Meijer, Wouter Dijkhuizen, Sebastian Kriebitzsch en Willem Godlieb worden bedankt voor hun inspanningen met betrekking tot het ontwikkelen, bouwen en onderhouden van de Oscar en Citra computerclusters. De administratieve afhandeling van het project was altijd in goede handen bij Nicole Haitjema.

Tijdens de promotietijd heb ik ook een afstudeerster mogen begeleiden. Jeanne Collignon heeft zich bezig gehouden met simulaties en experimentele validatie op het gebied van granulaire convectie. De experimentele validatie bleek echter gecompliceerder dan voorzien. Ik zal geen bloemlezing geven over de typen geteste wandmaterialen en het monnikenwerk dat gepleegd moest worden om de ruwe wanden te vervaardigen. Het resultaat mag er echter zonder meer zijn en zou zonder haar inspanningen niet mogelijk zijn geweest, waarvoor hartelijk dank!

De DPM code heeft al een lange historie en 'generaties' promovendi hebben eraan gewerkt. Ten eerste wil ik Bob Hoomans bedanken voor het leggen van de fundamenten van de code. Verdere uitbreidingen zijn gepleegd door Mathijs Goldschmidt, Albert Bokkers, Jeroen Link en Mao Ye. Recentelijk zijn door Willem Goblieb zelfs de eerste stappen richting parallel rekenen gezet. Ik ben dan ook zeer benieuwd waar de begrenzing van het model zal komen te liggen in het licht van de voortschrijdende optimalisatie van de code en ontwikkelingen op het gebied van computer hardware. Verder wordt Henk Jan van Gerner, ook werkzaam op het gebied van geschudde bedden, bedankt voor de discussies.

De sfeer op de 'werkvloer' (ook wel kantoortuin genaamd) heb ik altijd als erg plezierig ervaren. Zowel binnen als buiten werktijd werd er regelmatig over de meest uiteenlopende onderwerpen gediscussieerd, waarbij 'buiten' vaak onder het genot van een drankje was op de Vlugtheuvel of in de borrelkelder van studievereniging Alembic. In dit kader wil ik de FAP-borrelcommissarissen (Albert Bokkers, Renske Beetstra, Jan Albert Laverman, Sander Noorman en Sebastian Kriebitzsch) en de Vlugterlab-lecture coördinatoren (Joris Smit en Tymen Tiemersma) noemen die middels hun inspanningen het 'lezingencircuit' altijd tot een succes hebben gemaakt. Ik wil verder alle (oud-) collega's van FAP, OOIP, Procede en Sasol bedanken voor de gezellige tijd.

Ik heb me de afgelopen jaren ook altijd prima vermaakt binnen (beach) volleybal vereniging Harambee en wil iedereen bedanken voor de goede tijd. Ook de contact-AIO's van het Burgerscentrum (en in het bijzonder delegatie Enschede) worden bedankt. De autoritten naar Utrecht/Amersfoort leenden zich altijd uitstekend voor gesprekken over Enschede en de rest van de wereld.

Er waren echter ook 'actievere' activiteiten zoals het vakgroep volleybal, voetbal, bowlen, wadlopen en het jaarlijkse zeilevenement in Friesland. In dit kader wil ik Liesbeth Kuipers ook van harte bedanken voor de organisatie van de jaarlijkse skivakantie en het Waarbeek-feest (voorheen pan-feest). Ik heb jouw betrokkenheid bij de vakgroep altijd zeer gewaardeerd.

Ik wil tevens van deze gelegenheid gebruik maken om mijn paranimfen, Jorrit de Jong en Wouter Dijkhuizen, te bedanken. Jorrit is een oud studie- en huisgenoot en Wouter een oud-collega. Leuk dat jullie van de partij zijn! Verder wil ook mijn (oud-) huisgenoten Marcel Meinema en Hans Noorlag bedanken voor de goede tijd aan de Rembrandtlaan.

Tot slot wil ik mijn ouders, mijn broertje Jan-Jaap en z'n vriendin Inez noemen. Hoewel jullie misschien niet altijd begrepen waar ik mee bezig was, hebben jullie altijd belangstelling en support getoond.

Nogmaals iedereen van harte bedankt!

Christiaan